Remote sensing derived spatial patterns of glacier mass balance in Tibet

Von der Fakultät für Georessourcen und Materialtechnik
der Rheinisch -Westfälischen Technischen Hochschule Aachen

zur Erlangung des akademischen Grades eines
Doktors der Naturwissenschaften
genehmigte Dissertation
vorgelegt von **M.A.**

Marinka Spieß

aus Berlin

Berichter: Univ.-Prof. Dr.rer.nat. Frank Lehmkuhl
Univ.-Prof. Dr.rer.nat. Christoph Schneider
Univ.-Prof. Dr.rer.nat. Dieter Scherer

Tag der mündlichen Prüfung: 06. Juni 2016
Diese Dissertation ist auf den Internetseiten der Hochschulbibliothek online verfügbar

Abstract

The climate has changed on the Tibetan Plateau. The air temperature has shown distinct increase since the 1960s, exceeding the increase in other land areas of the same latitudinal position in the Northern Hemisphere. The retreat of Tibetan glaciers in connection with climate change is of interest since the glacierized areas constitute important freshwater resources – which, among others, provide the basis for all livelihoods on the plateau. Furthermore, the glaciation and snow cover of Tibet are crucial to feedback mechanism in the global climate system.

Glacier retreat has been documented in many areas of the Tibetan Plateau. Regional differences in glacier change across the Tibetan Plateau are evident. Measured glaciological, meteorological and hydrological data are largely absent due to difficult excess of the remote areas. Only few and spatially dispersed mass balance studies have been conducted to date. Remote sensing presents thus preferable methods in order to monitor Tibetan glacier change.

In this thesis the Moderate-resolution Imaging Spectroradiometer (MODIS) snow product and MODIS Level 1 radiance Swath Data is used to derive snow line altitudes. The snow line altitude at the end of the ablation period provides a proxy for the equilibrium-line altitude (ELA) of a glacier. The variability of the annual ELA itself is a valuable proxy for the variability of glacier mass balance. The mass balances of different glaciers in a specific region often show very high correlations in their temporal variance even though the transient snowline elevation can vary across individual glaciers. In this thesis the former three facts are utilized to derive daily regional snow line altitudes and interannual ELAs on different glacierized regions distributed across the Tibetan Plateau. The regions of interest are the Western Nyainqêntanglha range, three areas in the mountains of the Transhimalayas, the Gurla Mandhata massif in the western Himalayas, the Muztagh Ata in the Pamirs, the Ulugh Muztagh ice cap in the Kunlun Shan and the Purogangri ice cap in the central eastern part of the plateau. The variability of the ELA is used to reveal differences in glacier response to the various climatic forcings.

Validation and comparison of results are conducted utilizing Landsat images and a modelling approach. The derived transient snow lines are used to fit the physical based COupled Snowpack and Ice surface energy and MAss balance model (COSIMA) in order to derive energy and mass balance components on a monthly basis. The high resolution atmospheric model data from the High Asia Refined dataset (HAR) is used to correlate ELA variability and to force the COSIMA model.

Results show a distinct spatial pattern of average ELA proxy with lowest altitude in the Pamirs dominated by westerlies. Average ELA on the TP is remarkably higher. A tendency towards a generally ascending ELA and more negative MB in the last decade is apparent at the Western Nyainqêntanglha range. A distinct negative MB is modelled for Ulugh Muztagh in the Kunlun Shan between 2008 and 2010. The remote sensing fitted usage of HAR forced COSIMA appears feasible for the analysis on a monthly or annual basis. Sublimation is favoured by rising temperatures, even during periods with temperatures well below freezing point, especially under arid conditions. Results further confirm the essentially different climatic patterns due to large scale circulation and local factors. Whereas, for example, increased westerly air flow in November enhances sublimation at glaciers in the east and central Plateau, it is the driver of increased snowfall in the Pamirs leading to a contrasting regional pattern of ELA variability. Strong southerly flow in July is connected to higher temperatures and is correlated with an increased ELA in most of the study regions. Monsoonal influence is traceable in regions in the Himalaya and Transhimalaya between June and September. El

Niño in spring (summer) is connected to a lower (higher) ELA in the Pamir (western Himalaya). In February or March a positive phase of NAO is connected to higher wind speed and a lower ELA at many studied regions.

The thesis contributes to a further and detailed understanding of the spatially differencing characteristics of climate forcing of the glaciers on the Tibetan Plateau. It serves to increase the knowledge on the current status of glaciers and cryosphere-atmosphere interaction to estimate their evolution in the future on the Tibetan Plateau. Such results are essential for further improving research on glacier related water availability in Tibet.

Zusammenfassung

Das Klima hat sich verändert auf dem Tibetischen Plateau. Die Lufttemperatur zeigt seit den 1960ern einen Erwärmungstrend, welcher den Anstieg über Landflächen in gleichen Breitengraden auf der Nordhemisphäre deutlich übersteigt. Der Rückgang von Tibetischen Gletschern im Zusammenhang mit dem Klimawandel ist bedeutend, da die vergletscherten Gebiete einen wertvollen Süßwasserspeicher darstellen, welcher Grundlage allen Lebens und Wirtschaftens auf dem Plateau ist. Die Vergletscherung und die Schneebedeckung sind außerdem entscheidend für globale Feedbackmechanismen des Klimas.

Der Gletscherrückgang wurde in vielen Gebieten des Tibetischen Plateaus belegt, wobei aber regionale Unterschiede bestehen. Durch den schwierigen Zugang zu den entlegenen Regionen sind glaziologische, meteorologische und hydrologische Messdaten größtenteils nicht vorhanden. Dadurch liegen auch nur sehr wenige Gletschermassenbilanzstudien vor. Die Fernerkundung bietet unter diesen Voraussetzungen Ansätze um die Veränderung der Gletscher nachvollziehen zu können.

In dieser Arbeit werden das snow product und die Level 1 Radiation Swath Daten des Moderate-resolution Imaging Spectroradiometer (MODIS) genutzt um Schneelinien abzuleiten. Die Schneelinienhöhe am Ende der Ablationsperiode spiegelt die Gleichgewichtslinie (ELA) eines Gletschers wieder. Die Variabilität der jährlichen ELA ist ein wertvoller Proxy für die Variabilität der Massenbilanz. Die Massenbilanzen verschiedener Gletscher in einem Gebiet zeigen oft eine sehr hohe Korrelation in ihrer jährlichen Variabilität, auch wenn die absolute Höhe der Schneelinie auf den einzelnen Gletschern abweichen kann. In dieser Arbeit liegen die drei zuletzt genannten Fakten zugrunde um für unterschiedliche Regionen auf dem Tibetische Plateau tägliche regionale Schneelinienhöhen und interanuelle ELAs abzuleiten. Diese Regionen sind im Einzelnen: die westliche Nyainqêntanglha Kette, drei Regionen in den Bergen des Transhimalayas, das Gurla Mandhata Massiv im westlichen Himalaya, Muztagh Ata im Pamir, Ulugh Muztagh im Kunlun Shan und die Purogangri Eiskappe im zentralen Osten des Plateaus. Die Variabilität der ELAs wird genutzt um Unterschiede in den Gletscherreaktionen auf verschiedenen klimatischen Antrieb zu beleuchten.

Die Validierung und der Vergleich der Ergebnisse wurden anhand von Landsat Bildern und einer Modellierung durchgeführt. Die abgeleiteten transienten Schneelinien wurden genutzt um das physikalisch basiertes Energie- und Massenbilanzmodel der Schneebedeckung und Eisoberfläche (COSIMA) zu fitten und Energie- und Massenbilanzkomponenten auf monatlicher Basis abzuleiten. Die hochauflösenden atmosphärischen Modelldaten des High Asia Refined Datensatzes (HAR) wurden genutzt um klimatische Variablen mit der ELA Variabilität zu korrelieren und um das COSIMA Model anzutreiben.

Die Ergebnisse zeigen ein räumliches Muster durchschnittlicher ELAs. Die niedrigste ELA liegt im Westwind dominierten Pamir, während die durchschnittliche ELA auf dem Plateau wesentlich höher liegt. Im westlichen Nyainqêntanglha zeigt sich eine Tendenz zu generell ansteigender ELA und zu negativer Massenbilanz im letzten Jahrzehnt. Am Ulugh Muztagh im Kunlun Shan wurden negative Massenbilanzen von 2008 bis 2010 modelliert. Das durch die Fernerkundungsdaten angepasste und mit HAR Daten angetriebene COSIMA ist nützlich für eine Analyse auf monatlicher oder jährlicher Basis. Sublimation wird unter ariden Bedingungen durch steigende Temperaturen begünstigt auch wenn die Temperaturen deutlich unter dem Gefrierpunkt liegen. Die Ergebnisse bestätigen weiter, dass die klimatischen Bedingungen und Einflussfaktoren in den untersuchten Regionen durch das

Zusammenspiel von großräumigen Zirkulationen und lokale Faktoren sehr unterschiedlich sind. Verstärkte Westwinde im November verstärken zum Beispiel die Sublimation auf Gletschern im östlichen und östlich-zentralen Plateau. Andererseits sind sie der Antrieb für stärkeren Schneefall im Pamir, was jeweils zu gegensätzlichen Mustern der ELA Variabilität führt. Starke südliche Anströmung im Juli ist in den meisten untersuchten Gebieten mit höheren Temperaturen und einer höheren ELA korreliert. Monsunaler Einfluss ist auffindbar in den Regionen des Transhimalayas und Himalayas zwischen Juni und September. Ein El Niño Event im Frühling (Sommer) ist mit niedrigerer (höherer) ELA im Pamir (westlichen Himalaya) verbunden. Eine positive NAO-Phase im Februar oder März hängt in vielen untersuchten Regionen mit höherer Windgeschwindigkeit und niedrigerer ELA zusammen.

Diese Arbeit trägt zu einem detaillierterem Verständnis der räumlich differenzierten Ausprägungen von Gletschern in Tibet bei. Sie dient der Verbesserung des Verständnisses über Gletscher – Atmosphäre Interaktionen und leistet einen Beitrag um die zukünftige Entwicklung der Gletscher besser abschätzen zu können. Entsprechende Ergebnisse sind notwendig für die weitere Forschung zu gletscherbezogener Wasserverfügbarkeit in Tibet.

Acknowledgements

First I like to express my gratitude to Prof. Christoph Schneider for being a supportive supervisor. He always found the time to listen whenever it was needed and also trusted me to work independently. He always provided a clear thought and ideas about the bigger picture whenever I was not able to see the wood for the trees. I warmly thank Prof. Frank Lehmkuhl for kindly stepping in to supervise my thesis as well as Wolfgang Römer who had my back especially at the end of my thesis. I thank Dieter Scherer for providing initial ideas and always offered support for realisation.

I salute to all my colleagues in Aachen: Eva, Steffi, Katja, Isabel, Miriam, Rebecca, Mona, Lars, Marco, Timo, Gernot, Tobias, Oliver, David and Bastian. I thank Gunnar Ketzler, who I respect for his engaged work, and Elke Bruer-Plastrotmann for her indispensable support.

I thank my colleagues in WET and DynRG-TiP projects, who made me looking forward to every meeting: Julia, Benjamin, Nicolai, Frank, Niklas, Sophie, Jan, Fabien, Dieter, Manfred B., Manfred F. and Volker.

For surviving and enjoying surviving in Tibet I heartfelt thank Yang Wei, Eva, Julia, Fabien and Nicolai. I especially thank Marco, who got me started with IDL, and Fabien, who was open for any of my IDL related questions and clearly was my personal WAVE wizard. Additionally I like to thank many people in the High Asia community who I enjoyed getting to know a little and spending time with them during various meetings.

Most importantly I thank Arne, my beloved parents, my dearest grandmother, the whole little family, Alix, Saskia, René and my other exceptional beautiful, special and intelligent friends for support, distraction and reliability!

List of figures

List of tables

List of abbreviations

AAR ..... accumulation area ration
AATSR ..... Advanced Along-Track Scanning Radiometer
AMJ ..... April, May, June
AO ..... Arctic Oscillation teleconnection pattern
APDRC ..... Asia Pacific Data Research Centre
ASTER ..... Advanced Spaceborne Thermal Emission and Reflection Radiometer
ATO ..... air temperature offset
AVHRR ..... Advanced Very High Resolution Radiometer
AWS ..... automatic weather station
BMBF ..... Bundesministerium für Bildung und Forschung
CAME ..... Central Asia – Monsoon dynamics and Geo-ecosystems (BMBF programm)
CAS ..... Chinese Academy of sciences
CGI ..... Chinese glacier inventory
COSIMA ..... physical based COupled Snowpack and Ice surface energy and MAss balance ..... model
DAAC ..... NASA Distributed Active Archive Centre
DEM ..... Digital elevation model
DFG ..... Deutsche Forschungsgesellschaft
DJF ..... December, January, February
DMI ..... Indian Ocean Dipole Mode index
DynRG-TiP ..... Dynamic Response of Glaciers on the Tibetan Plateau to Climate Change ..... (DFG Project)
EAWR ..... East Atlantic/Western Russia teleconnection pattern
ELA ..... Equilibrium-line altitude
ENSO ..... El Niño Southern Oscillation
ENVI ..... Environment for Visualizing Images (software application)
ETM+ ..... Enhanced Thematic Mapper Plus (Landsat)
GCM ..... general circulation model
GDEM ..... Global Digital Elevation Model
GLAS ..... Geoscience Laser Altimeter System
GLIMS ..... Global Land Ice Measurements from Space
GLOF ..... glacier lake outburst flow
GRACE ..... Gravity Recovery And Climate Experiment
HAR ..... High Asia Refined analysis
HRS ..... High Resolution Stereoscopic
HRV ..... High resolution visible (SPOT)
HRVIR ..... High resolution visible and infrared (SPOT)
HWSI ..... horizontal wind shear index
ICESat ..... ice, cloud and land elevation satellite
ICIMOD ..... International Centre for Integrated Mountain Development
IDL ..... Interactive data language
InSAR ..... interferometric synthetic aperture radar

IPCC..... Intergovernmental Panel on Climate Change
IR..... shortwave infrared
ISM..... Indian summer monsoon index
ITP..... Institue for Tibetan Plateau Research (CAS)
JJA..... June, July, August
LIDAR ..... Light detection and ranging
LW_{in}..... incoming longwave radiation
LW_{net} ..... net longwave radiation
LW_{out} ..... outgoing longwave radiation
MA ..... Muztagh Ata
MAM..... March, April, May
MB ..... mass balance
MCTK ..... ENVI plug-in MODIS Conversion Toolkit
MEI..... Multivariate ENSO Index
MERIS..... Medium Resolution Imaging Spectrometer
METI..... Ministry of Economy, Trade, and Industry of Japan
mm w.e. ..... millimetre water equivalent
MOD02QKM ..... MODIS level 1 product, satellite Terra
MOD10A1 ..... MODIS level 2 product, satellite Terra
MODIS..... Moderate Resolution Imaging Spectroradiometer
MYD02QKM ..... MODIS level 1 product**,** satellite Aqua
MYD10A1..... MODIS level 2 product, satellite Aqua
NAO ..... North Atlantic Oscillation
NASA..... National Aeronautics and Space Administration
NCAR UCAR ..... National Centre of Atmospheric Research
NCEP NCAR ..... Reanalysis product from the National Centers for Environmental Prediction ..... and the National Center for Atmospheric Research
NDSI ..... Normalized Difference Snow Index
NOAA ..... National Oceanic and Atmospheric Administration
NSIDC..... National Snow and Ice Data Centre
NWN ..... north-west oriented slope of Western Nyainqêntanglha range
p..... p value
PDD..... positive degree day
PIC..... Purogangri ice cap
PNA..... Pacific/North America teleconnection pattern
POL ..... Polar/Eurasia teleconnection pattern
prcp..... precipitation
PSF ..... precipitation scaling factor
Q_G..... ground heat flux
Q_{lat} ..... turbulent latent heat flux
Q_{melt} ..... melt energy
Q_{sens} ..... turbulent sensible heat flux
r ..... correlation coefficient
RGI ..... Randolph glacier inventory
RMSE..... root mean square error

ROI ..... region of interest
SAR..... snow pixel area ratio
SEB ..... Surface energy balance
SEN..... south-east oriented slope of Western Nyainqêntanglha range
SLA ..... mean snow line altitude
SLC ..... Scan Line Corrector
SO ..... Southern Oscillation teleconnection pattern
SON..... September, October, November
SPOT ..... Satellites Pour l'Observation de la Terre or Earth-observing Satellites
SRTM..... Shuttle radar topography mission
Std dev. ..... standard deviation
SW_{in}..... incoming shortwave radiation
SW_{out} ..... outgoing shortwave radiation
TAR ..... Tibetan Autonomous Region
TiP ..... Tibetan Plateau: FormationClimateEcosystems
TM..... Thematic Mapper (Landsat)
TP ..... Tibetan Plateau
TPE ..... Institute of Tibetan Plateau Research
T_s ..... surface temperature
UM ..... Ulugh Muztagh massif
UMdetail..... detail region of Ulugh Muztagh
USGS ..... U.S. Geological Survey
UTM ..... universal transverse Mercator (coordinate system)
WET ..... Variability and Trends in Water Balance Components of Benchmark Drainage
..... Basins on the Tibetan Plateau (part of BMBF programm CAME)
WGS ..... world geodetic system
WP ..... West Pacific teleconnection pattern
α..... albedo

Content

1 Introduction

1.1 Motivation and intention

Not only ancient spiritual mystery and recent social-political conflicts are associated with the Tibetan Plateau but also a high scientific interest concerning a variety of research disciplines. Since entering Tibet was forbidden for westerners in former times the geographical exploration took place only since about 1900. Since then the interest for the literally outstanding Tibetan Plateau increased steadily. Nevertheless scientific knowledge is still limited due to lack of ground truth data in large areas of the TP.

The Tibetan Plateau (TP), also called Qinghai-Xizang, forms a clearly bordered unit. Its elevated area covers 2.5 million km² and has an average altitude of around 4700 m a.s.l. (Meyerhoff et al. 1991; Wang et al 2014). The plateau is bounded by even higher mountain ranges, namely by Kunlun Shan, Altun Shan and Qilian Shan to the north, the arc of the Nyainqêntanglha range in the south-east, the Gangdise mountains (the latter two form the Transhimalaya range) and Himalaya to the south and Karakorum and Pamir mountains to the west (see Fig. 2.1). The plateau hosts vast plains and many dome-like mountains higher than 6000 m a.s.l., which provide favourable conditions for the development of ice caps (Wei et al. 2014).

The big land mass of the TP reaches into the mid-troposphere. Thus scientists were interested in its role in the atmospheric circulation early on. The TP acts as huge natural barrier, blocks the mid-latitude westerly jet (e.g. Domrös and Peng 1988) and influences the Asian summer monsoon. Its role as main driver for the Indian monsoon connected to a thermally induced pressure system on the TP is unresolved since last findings suggest the mechanical/orographic importance of the Himalaya range rather than that of the plateau (e.g. Boos and Kuang 2010; Molnar et al. 2010).

The TP contains the largest number of glaciers after the polar regions (Yao et al. 2012). The TP has been named ‘Watertower of the world’, ‘the Third Pole’ and the ‘Antenna of the Earth’ indicating the importance for supra-regional fresh water supply and global climate stability (Qui et al. 2008; Immerzeel et al. 2010; Kang et al. 2010; Chen et al. 2012; Wei et al. 2013; Yao 2010; Xu 2014).

The cryosphere is considered to be one of the most sensitive indicators of climate change especially due to its positive feedback mechanisms enhancing climate warming (Lemke et al. 2007; Kang et al. 2010). Albedo feedback is enhanced in high altitudes due to stronger solar radiation. The decrease of glaciers comes along with the loss of stable snow cover which increases the warming rate due to lower albedo (Liu and Chen 2000; Flanner and Zener 2005; Kang et al. 2010).

In the climate change debate glacier retreat is connected to fresh water loss and sea level rise (Lemke et al. 2007). Glaciers play a special role regarding water storage. They buffer water in times of precipitation maxima and supply fresh water in times of dry and warm seasons. Glacier retreat might consequently result in flood risk and increased drought risk (Hagg et al. 2006). Furthermore the TP with its adjective mountain ranges clearly has an important function in supplying precipitation due to orographic advection (Immerzeel et al. 2010). On the arid TP itself glaciers represent the only reliable fresh water source for consumption and irrigation of local inhabitants and farmers. The overwhelming majority of the glaciers on the TP drain into endorethic basins and seem to be linked to lake level rise rather than to sea level rise (Zhang et al. 2011; Kropáček et al 2012). Considering high relative amounts of sublimation, glacier loss might have reduced effect on local meltwater (Kaser et al. 2010).The relative importance of glacier runoff for the water balance of individual basins varies (Zhu et al. 2010; Zhao et al. 2014a; Biskop et al. 2015). In the Upper Indus basin the glacier runoff is revealed to be the main reason for the increased total runoff. Projections also show a considerable contribution of glacier melt to the Brahmaputra runoff (Su et al. 2016).

The importance of topics in connection with Tibetan glaciers as for example snow cover change, permafrost degradation, lowering of water levels, desertification, methane release and large scale teleconnections is likely to grow with ongoing climate change (Wang et al. 2006; Cheng et al. 2007, Yang et al. 2010). Glacial hazards such as glacial lake outburst flows (GLOF) and ice avalanches seem to increase in number and relevance (Kääb et al. 2003; Kropáček et al. 2015). Along the highly seismic active mountain ranges bordering the TP landslides may become more prevalent at slopes formerly stabilized by permafrost (Gruber and Haeberli 2007).

Like in most parts of the world glaciers receded on the TP during recent decades (Stocker at al. 2013; Yao et al. 2012; Bolch et al. 2012). The rate of shrinkage disperses spatially and even balanced mass budgets were detected (Kääb et al. 2012; Gardner et al. 2013; Neckel et al. 2014; Kääb et al. 2015). Reasons for the variability in response to climate change are likely to be spatially diverse local climate and effects of climate change (Kang et al. 2010; Palazzi et al. 2013).

All of the above mentioned aspects reveal basically discovery spirit and the mere importance to study the Tibetan glacier as the main motivation for this thesis. In the absence of observational meteorological and glaciological data, especially at higher altitudes, and, due to the remoteness and inaccessibility of the many parts of the plateau the regional climate and cryo-atmospheric interactions are little studied so far. In the absence of in situ data information on longer timescales is mostly available through remote sensing approaches for the remote glaciers. The results provide insights into the long-term development of glaciers and can be connected to averaged climatic parameters (e.g. Bolch et al. 2012; Kääb et al. 2012; Yao et al. 2012; Gardelle et al. 2013). However, to understand locally specific cryo-atmospheric mechanisms, interannual glacial development and atmospheric forcing we need to derive information at high temporal and spatial resolution.

Remote sensing studies of dispersed key regions on the TP can provide observational datasets. These datasets can be used to calibrate and validate physically based glacier models which again improve understanding of the local glaciological mechanisms.

The following key questions describe the intention of this thesis.

- Can we adjust and refine methods to automatically derive transient snow lines from freely available remote sensing data for application on the Tibetan Plateau?
- Can we reliably derive an ELA proxy for the study regions? What are the limitations of the method?
- Can we identify a spatial pattern of interannual MB variability and climatic forcing across the Tibetan Plateau?
- How can the method help for a better understanding of glaciers outside of direct observations? What are the methodological limitations?
- Which connections can be revealed between interannual ELA variability and large scale atmospheric teleconnections?
- Which atmospheric components dominate the glacier variability and how do the influences vary in different region on the TP?
- Can remote sensing derived snow line altitude be used as additional calibration data for glacier modelling?

In 2008 a Sino-German Priority Programme (Tibetan Plateau: Formation – Climate – Ecosystems) was initiated by the German Research Foundation (DFG) to develop a multidisciplinary approach focussing on the major driving forces and their interactions on the TP. As part of this priority programme the DynRG-TiP project (Dynamic Response of Glaciers on the Tibetan Plateau to Climate Change) aimed at a better understanding of atmosphere-cryosphere interactions. Since 2011 the project was complemented by a Federal Ministry of Education and Research (BMBF) programme Central Asia – Monsoon dynamics and Geo-ecosystems (CAME). Within this the WET project was initiated (Variability and Trends in Water Balance Components of Benchmark Drainage Basins on the Tibetan Plateau) to deal with the interaction of atmospheric, hydrological and glaciological aspects within drainage basins across the TP. The two projects amounted in the complementary cooperation between the RWTH Aachen University, TU Berlin, TU Dresden, Uni Marburg, Uni Tübingen and Uni Jena until 2014. The group of RWTH Aachen focussed mainly on the development and validation of a surface energy balance and mass balance model and the development of a remote sensing method to derive glacier status. The Sino-German field campaigns on the TP were carried out together with the Institute of Tibetan Plateau research (ITP) of the Chinese Academy of sciences (CAS). The work presented in this thesis took place based on this cooperation.

1.2 Thesis outline

In chapter 2 a first overview of the regional settings of the thesis is given. The different areas of the TP are distinguished and a first classification about climatology is provided.

Chapter 3 outlines the current state of research regarding climatology and the glaciology of the TP. Furthermore, an introduction on methods and approaches is given. It is divided into a section about methodological principles concerning equilibrium-line altitudes of glaciers and a section about remote sensing methods observing ice and snow.

Chapter 4 introduces a remote sensing method to derive snow line altitudes and states connections between the glacier development and large scale climatology at the Purogangri icecap. It constitutes the content of a research paper published in Geografiska Annaler: Series A, Physical Geography:

Spieß M., Maussion, F., Möller, M., Scherer, D. and Schneider, C. (2015): MODIS derived equilibrium-line altitude estimates for Purogangri Ice Cap, Tibetan Plateau, and their relation to climatic predictors (2001-2012). Geografiska Annaler, Series A, Physical Geography, 20, 1-17. doi: 10.1111/geoa.12102

In chapter 5 the method to derive snow line altitudes based on satellite data is enhanced and carried out using data with a higher spatial resolution. This method is utilized in eight study sites across the TP and examined for connections to the spatial and temporal patterns of large scale climate. The content is published in Annals of Glaciology:

Spieß M., Schneider, C. and Maussion, F. (2016a): MODIS derived interannual variability of the equilibrium-line altitude across the Tibetan Plateau. Annals of Glaciology, 57(71). doi:10.3189/2016AoG71A014

For chapter 6 a refined method is introduced and applied to a glacierized region in the northern plateau. Results of the remote sensing based method to derive transient snowlines are used to calibrate a physically based glacier model. Results between both approaches are compared on a daily basis. The results are content of a research paper published in the Journal of Mountain Science:

Spieß M., Huintjes, E. and Schneider, C. (2016b): Comparison of modelled- and remote sensing-derived snow line altitudes at Ulugh Muztagh, northern Tibetan Plateau. Journal of mountain science, 13(4), 593-613. doi:10.1007/s11629-015-3818-x

The synthesis in chapter 7 describes the design of the remote sensing methods developed and applied in this thesis, conducts an overall summary and draws a final conclusion including an outlook to further research options.

For all three original papers the author of this thesis was responsible for data preparation, the enhanced development and implementation of methods and models, the analysis and interpretation of the results and all writing.

2 Synoptic geographical view of the Tibetan Plateau

Within this thesis different regions on the TP have been concentrated on. In the following chapter a short overview of relevant features of the TP as well as the discussed regions of interest is given. This includes characteristics of the individual regions of interest with respect to the overall TP. For a comprehensive overview of the current state of research concerning climate, glaciers and climate change, please be referred to chapter 3.1. Detailed information about the individual study sites are introduced in the corresponding chapters.

2.1 Administration

The TP is a geological formation building the highland of western China. The TP represents almost half of the traditional Tibetan area (Fig. 2.1). Tibet consists of the central plateau region of Utsang including the regions of Ngari and Jangtang, and the lower regions of Kham and Amdo in the east (Ryavec 2015). After the Chinese occupation in 1950 these regions were comprised within the Chinese administration. Utsang and part of Kham form the Chinese province of Tibetan Autonomous Region (TAR) since 1965, whereas remaining area of Kham and Amdo are devided and included into four western Chinese provinces: Qinghai, Gansu, Sichuan and Yunnan (Fischer 2005).

According to the Chinese census 2010 the population includes 6.2 Mio Tibetans. The total population of TAR is given to be 3 Mio (China 2010 census data released 2011). The economy on the TP traditionally relies on subsidence agriculture and nomadic pastoralism (Klein et al. 2004; Choekyi 2014). Tibetan nomadic pastorialism is older than 6000 years (Miehe et al. 2009).

2.2 Formation of the TP

The climate and distinction of the TP is originated by the geological formation of the TP. The collision of the Indian plate and the Eurasian plate took place around 50-70 Mya after the interjacent ocean Tethys was subducted beneath the Asian plate (Yin and Harrison 2000; Molnar et al. 2010). Induced by the collision the Pamir-Tibet-Himalaya orogenic system was uplifted (Murphy et al. 1997; Leech et al. 2005; Mulch and Chamberlain 2006). The basic structure of the terranes still predetermines the

modern east-west trending crustal blocks and interjacent suture zones on the TP (Ratschbacher et al. 2011). There is still ongoing research about exact mechanisms, deformations and crustal motion connected to the uplift. A northward migration of the uplift is concluded in many studies due to crustal thickening. While the southern parts reached high elevation the northern area remained low and a deep lithosphere crust flow out of the Tibetan region towards the east is proposed (Mulch and Chamberlain 2006; Royden et al. 2008). Uplift of the eastern parts seems to have occurred latest with further uplift in the late Neocene (Royden et al. 2008). Other studies show that crustal shortening began more or less synchronously in the southern (Himalayas) and the northern border of the TP (Kunlun Shan and Qilian Shan) which relatively moved towards each other and constructed the TP (Yin and Harrison 2000; Molnar et al. 2010; Yuan et al. 2013). A further view is an inside-out growth of the TP (Wang et al. 2014). Measurements of crustal motion have revealed clockwise rotations (Kornfeld et al. 2014).

Fig. 2.1: Western provinces of China (dotted lines) and Tibetan cultural areas (light grey colours) (Fischer 2005).

2.3 Study regions

Since this thesis aims at covering the spatial diversity of the TP in climate and glaciology the study sites are distributed across the TP (Fig. 2.2).

The TP as a geological feature is clearly bordered within the surrounding mountain ranges. Defined by its geological formation the Qaidam basin, a temperate desert, the Altun Shan and the Qilian Shan in the far north-east belong to the Himalayan-Tibetan Orogen (Yin and Harrison 2000) (Fig. 2.2). In this thesis no study sites lie within these regions in the north-east.

In the 'high plateau zonation' after Chang (1981) the vegetational zones comprise montane forest, high-cold meadow, high-cold steppe, semi-desert and high-cold desert. The pattern of vegetation is related to precipitation and temperature (cf. chapter 3.1). Biomass decreases from southeast to northwest (Xu and Liu 2007). Sparse cultivated crops are mainly located in lower altitudes with mild climatic conditions between forest and grassland (Xu and Liu 2007). Many forest areas of southern and south-eastern TP were replaced by cropland in recent years (Cui and Graf 2009).

The northern plateau is referred to as the region of the Kunlun Shan, which forms a long arc from the Pamir in the west to the Gansu Corridor in the east. Its elevation is in average higher in the west and

lower in the east in average. Most glaciers are located in the upper reaches of the Western Kunlun Shan (Yafeng et al. 2005). The study region *Ulugh Muztagh* is situated in its central part, in the intersection zone between Western Kunlun Shan, Eastern Kunlun Shan and Altun Shan to the north.

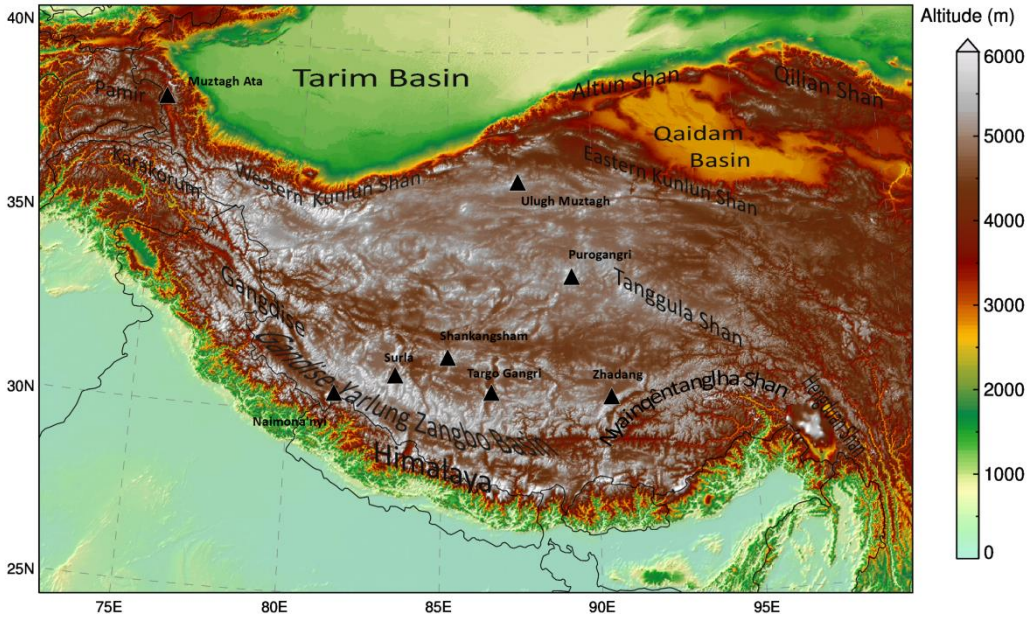

Fig. 2.2: Overview of the study regions of this thesis which are indicated as black triangles.

The southernmost part of the TP, the gradually descending northern slopes of the Himalaya and the Gandise-Yarlung Zangbo Basin hosts one study region (*Gurla Mandhata*) at its eastern and southern end (Fig. 2.2). In the southern part of the TP the Transhimalayas comprise the Nyainqêntanglha arc in the east and the Gangdise range in the west of the plateau (Fig. 2.2). A study site of this thesis is the *Western Nyainqêntanglha* neighbouring the Nam Co which is one of the largest and highest lakes on the TP. The Nyainqêntanglha mountain range displays a distinct water divide, with the south-eastern slopes belonging to the Brahmaputra drainage system. The region lies in the transition zone between the heavily monsoonal influenced regions with glaciers of maritime type in the southeast and the more arid central plateau region.

In the southern TP and in parts of the central Plateau the predominant vegetation is montane shrubby-steppe and alpine steppe (Zhao 1986). The alpine meadow consists mainly of *Kobresia pygmaea*. The *Kobresia pygmaea* pastures of the southern, south-eastern and central TP are the world's largest ecosystem (Miehe et al. 2008). The extremely firm turf protects large surfaces against erosion.

The central TP comprises the actual plateau with an average altitude of about 4700 m a.s.l. altitude. The basin is an endorheic drainage system with a high quantity of lakes. Within this thesis the central Transhimalayas are comprised in the denotation of central TP even though its southern slopes belong to the Brahmaputra drainage system. The three study sites located within the *Transhimalaya* are *Surla, Shankangsham* and *Targo Gangri*.

Along the east-west transect a change in dominating climate influences is supposed. The study region of *Purogangri ice cap* is located west of the Tanggula Shan in the eastern part of the central plateau (Fig. 2.2). The central TP can be classified as subalpine/semi-arid and alpine/arid in the north-western

part of the plateau (Domrös and Penn 1988). The area features many dome-like mountains higher than 6000 m a.s.l. These mountains provide favourable conditions for the development of ice caps and glaciers of extreme continental/subpolar type (Wei et al. 2014). The glaciers outside mountain ranges are scattered and distributed mainly near the highest peaks (Yafeng et al. 2005). Glaciers in the Gandise Shan are relatively small and mostly of cirque-hanging type (Yafeng et al. 2005).

The study region *Muztagh Ata* is situated outside the actual TP within the Eastern Pamir Mountains in the far north-west (Fig. 2.2). The Pamir Mountains are a highly glacierized region with a high amount of debris covered glaciers. It is strongly influenced by the mid-latitude Westerly Jet while the influence of monsoonal flow can be excluded (Bolch et al. 2012; Gardelle et al. 2013). Glacier termini reach low altitudes at about 4000 – 5000 m a.s.l. (Yafeng et al. 2005).

3 Current state of research

Through international research efforts the knowledge acquisition concerning the physical geography of the TP has increased substantially within the last decade. Among others the ITP and The International Centre for Integrated Mountain Development (ICIMOD) conducted programmes aiming at a better understanding of the climatic and environmental changes on the TP. Furthermore, the priority programme 'Tibetan Plateau: FormationClimateEcosystems' (TiP, http://www.tip.uni-tuebingen.de/index.php/de/) of the DFG and the research programme CAME (http://www.zentralasien.senckenberg.de/websiteCAMEenglish/index-engl.html) of the BMBF focussed on the TP within the last years. Most of the research is of foundational nature aiming for synergetic knowledge explaining the local as well as global role of the biggest high mountain plateau in the world. Applied research were mostly done in adjacent areas of the plateau where the changes in climate and glaciers affect the lives of millions inhabitants. Especially the southern slopes of the Himalaya have been studied concerning glacier lake outburst flow (GLOF) and future fresh water supply (e.g. Bolch et al. 2008; Shrestha et al. 2011; Kropáček et al. 2015; Neckel et al. 2015).

3.1 Climate and large scale atmospheric circulation patterns on the TP

The TP reaches up into the mid-troposphere. Consequently its extensive influence on the large scale atmospheric circulation was already stated since the 1950s (cp. Flohn 1958). The current climate of the TP is mainly controlled by the mid-latitude westerlies and the Indian monsoon system. Fig. 3.1 displays examples on how the circulation is commonly portrayed. Regional climate of the TP is mostly thought to be constructed by the seasonal variation of these major circulation patterns. Their concurrent role in the present climate of the TP is still an ongoing research topic (e.g. Mölg et al. 2012; Gao et al. 2014). The East Asian monsoon is an extratropical phenomenon, associated with frontal systems that migrate northward during spring. Precipitation from this frontal system reaches its westernmost position in June (Molnar et al. 2010). However, its influence on the TP is not resolved and might be minor (Maussion et al. 2014a; Curio et al. 2015).

Geopotential height and wind at 500 hPa level for winter and summer are shown in Fig. 3.2. In winter a strong mid-latitude westerly jet is established generated by the thermally induced pressure gradient between the inner and outer tropics. The southernmost jet position reaches the latitudinal level of the TP at about 30°N (Lauer and Bendix 2004). The zonal flow of the continental air masses is interrupted by the topography of the TP and the main stream is divided into a southern and northern

branch circuiting the TP (e.g. Schiemann et al. 2009; Fig. 3.1). Highest wind speed occurs south of the TP. In spring the formation gets disturbed by the shift of the Jet to the north. The intensity of the Jet decreases. The variance of its zonal position increases (Schiemann et al. 2009). Due to the strong solar heating of the elevated land masses in summer the high convective heating on the plateau induces the formation of the Tibetan Low pressure system which additionally blocks the zonal flow of the Westerlies. The position of the upper-tropospheric high pressure system was commonly thought to be on the central plateau tugging the monsoonal air masses onto the plateau (Yeh at el. 1957; Wu and Zhang 1998; Molnar et al. 2010). Recent studies suggest a position south of the TP acknowledging possible local enhanced precipitation due to the heating on the TP but questioning the primary role as a trigger for the Indian monsoon system (Boos and Kuang 2010; Ma et al. 2014; Maussion et al. 2014a).

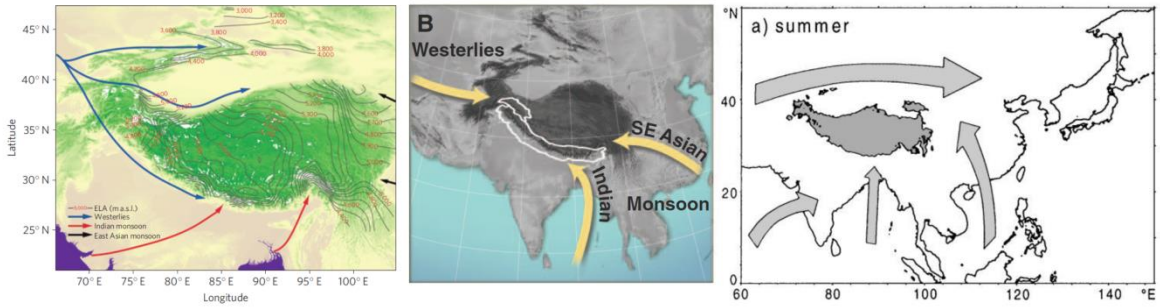

Fig. 3.1: Examples on summarising circulation influencing the Tibetan Plateau. Yao et al. 2012, Bolch et al. 2012, Lehmkuhl and Haselein 2000.

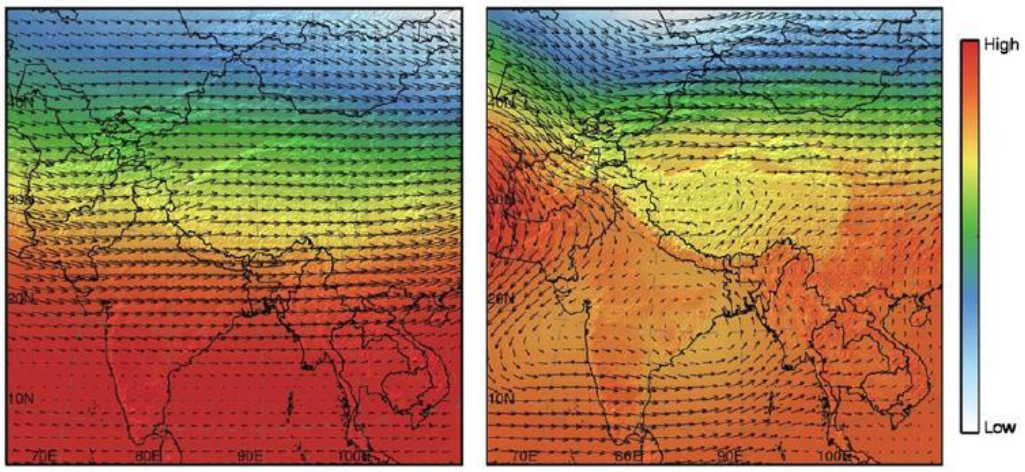

Fig. 3.2: Geopotential height and horizontal wind vectors at the 500-hPa level in winter (left) and summer (right). Note that the colour scale represents a different range for winter (low: 5.24 km; high: 5.89 km) and summer (low: 5.67 km; high: 5.90 km) (Maussion et al. 2014a).

A southeast-northwest gradient of precipitation and air temperature is apparent on the TP. High estimates of precipitation in the southeast TP arise from monsoonal atmospheric currents reaching the TP along the gorges onto the Plateau. Precipitation on the central plateau is mainly initiated through convection with minimum amounts on the lee sides of high mountain systems in the west of the TP (Flohn 1958; Böhner 2006). A clear pattern of arid conditions in intra-mountainous basins with less than 100 mm a^{-1} compared to amounts of above 1000 mm a^{-2} in elevated areas reveal a

generally decreased relevance of frontal precipitation in the central plateau areas (Böhner 2006; Gerlitz et al. 2015). Thus, the arid central TP is regularly characterized by less strong precipitation events in summer and a distinct diurnal cycle of precipitation in connection with a high relative amount of local convective precipitation (Liu et al. 2009; Maussion et al. 2014a). In consequence, thin patchy snow covers can occur all year round on the TP. On the other hand, destructive orographically induced snowstorms with tropical origin can form on the TP (Chen et al. 2012; Maussion et al. 2014a). A latitudinal temperature change exists as well but is usually disguised by the much stronger vertical zonation. The annual mean wind speed is highest in the northern and western parts of the plateau. Highest (lowest) wind speeds are found in spring (autumn) (You et al. 2014).

The results of Curio et al. (2015) suggest the westerlies as source of atmospheric water transport onto the TP also in summer. This is the case even along the large parts of the eastern Himalayas earlier suspected to be dominated by moisture of monsoonal source. There seems to be a water vapour input from the arid Tarim and Quaidam Basin to the northern TP which does not result in precipitation possibly due to subsidence. Another smaller input is revealed near the surface from the east and peaking in July. The amount of moisture which is recycled within the Plateau is estimated to be 60% (Curio et al. 2015).

Large-scale circulation patterns are apparently connected to the climate variability on the TP via teleconnections. On geological time scales the consistent uplift of the plateau was closely connected to the onset of the monsoon system, the drying of the Asian interior and the global Cenozoic cooling (Molnar et al. 2010; Li et al. 2014). The westerlies and the Asian summer monsoon influence the atmospheric variables on an inter- and intraannual scale on the modern TP. Different studies reveal teleconnections between those patterns and the North Atlantic / mid-latitude Europe (Liu and Yin 2001; Li et al. 2008; Bothe et al. 2011; Mölg et al. 2014; Yang et al. 2015), the tropical Pacific (Wu et al. 2009) and the western North Pacific (Takaya and Nakamura 2013) (Fig. 3.3).

Fig. 3.3: Locations of centres of action of the considered circulation indices; sea level pressure [circle] or sea surface temperature [box] anomalies; the signs indicate the anomalies during the respective positive phase.

The Indian Ocean Dipole as captured in the Dipole Mode Index (DMI) and the El Niño Southern Oscillation (ENSO) are found to directly influence Asian monsoon circulation with subsequent reduced or enhanced precipitation on the TP. Positive DMI in years without ENSO event is found to increase the snow cover of the TP (Yuan et al. 2012). After an El Niño event in winter an eastward propagating planetary wave in the troposphere forms a jet across the Himalayas leading to increased winter snowfall on the TP. The subsequently increased snow pack weakens the intensity of the Asian

summer monsoon (e.g. Shamann and Tziperman 2005; Bothe et al. 2011). Monsoonal flow strength does not necessarily represent the monsoonal convective strength. Wu et al. (2012) conclude that ENSO signals appear stronger in years with reduced snow cover on the TP. Furthermore Park et al. (2010) line out that an El Niño event persists via a warm anomaly of the Northern Indian Ocean. The moisture transport associated with the positive North Atlantic Oscillation (NAO) can compensate for the wind effect in this regard. The NAO seems to have an influence on precipitation on the eastern part of the plateau in spring to summer via a wave train teleconnection (Liu and Yin 2001; Li et al. 2008; Wu et al. 2009; Mölg et al. 2014). A positive NAO index and a northward displacement of the westerly jet in East Asia due to contrasting thermal anomalies in middle and high latitudes supports dry condition in the proximity of the plateau (Bothe et al. 2011). A teleconnection between atmospheric circulation anomalies in mid-latitude Europe and both air temperature as well as precipitation in the southeast TP is shown also by Yang et al. (2015). Surface temperatures over mainland China and the TP correlate strongly positive with the West Pacific (WP) index in winter and also positively in spring but with overall weaker correlation (Climate Prediction Center 2012). Positive Southern Oscillation (SO) phases generally result in below-average air temperatures and above-average precipitation over the southern and central TP and India (Bothe et al. 2010; Climate Prediction Center 2005).

3.2 Glaciers on the TP

The TP inhabits more than 100,000 km^2 of glaciers (Yao et al. 2012). The glaciers are mainly situated within the big mountain ranges bordering the TP (Fig. 3.4). In accordance with the spatial variance of climate and topography the glaciers on the TP are quite heterogeneous in form, status and sensibility to climate forcing.

Shi and Liu (2000) reveal a glacier classification based on continentality. They group the glaciers of the TP into three categories: maritime (temperate), subcontinental (subpolar) and extremely continental (polar) (Fig. 3.5). Maritime glaciers are located in the southeast of the plateau including the Henguan Mountains and eastern parts of Himalayas and Nyainqêntanglha range. These glaciers are clearly influenced by high amounts of precipitation connected to monsoonal flow (Maussion et al. 2014a). They consist of temperate ice with “warm” surface ice temperature, decreasing ice temperature with depth and pressure melting point at their base (Shi and Liu 2000; Cogley et al. 2011). Additionally, their ELA is usually at low altitudes what makes them very sensitive to climate variability.

Subcontinental glaciers can be found in the eastern Kunlun Shan, western Nyainqêntanglha range, and the northern slopes of the mid to western Himalayas and Karakorum (Shi and Liu 2000). In higher altitudes these glaciers still receive 500 – 1000 mm of annual precipitation sums. Polythermal glaciers are common in these transition zones between continental and maritime glaciers. They consist of adjacent zones of temperate and cold ice within the ice body. A temperate layer is usually found near the bed due to geothermal heat flux. Temperate ice within the cold glacier can form when infiltrating melt water refreezes and releases latent heat (Aschwanden 2008; Cogley et al. 2011).

Extremely continental glaciers are located in cold and dry climates and can be found in the central TP including large parts of the Transhimalayas, western Kunlun Shan and eastern Pamir (Shi and Liu 2000; Fujita and Ageta 2000; Scherler et al. 2011). Most of the available energy at the glacier surface is used for sublimation. Besides the near-surface layer and possibly the bottom layer, the glaciers

consist of cold ice through-out (Cogley et al. 2011). The glaciers are less sensitive to air temperature change and their flow velocity is low (Cogley at el. 2011; Hu et al. 2014).

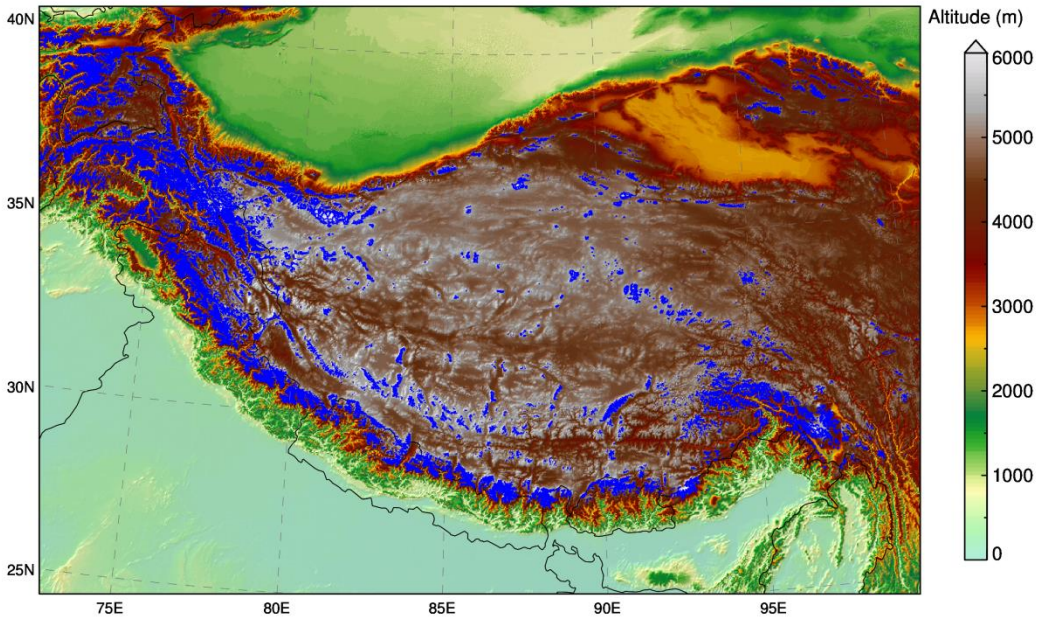

Fig. 3.4: Distribution of glaciers on the Tibetan Plateau and its adjacent areas. In blue, glaciers are shown according to the Randolph Glacier Inventory (RGI).

Since the timing and amount of precipitation is a main influencing factor for glacier MB on the TP (Fujita and Ageta 2000; Mölg et al. 2012; Kang et al. 2009) a classification of glaciers based on their accumulation regime is valuable. Summer-accumulation-type glaciers gain mass mainly from summer snowfall connected to monsoonal flow. Their annual MB variations are generally small (Cogley et al. 2011). Those glaciers occur in the south-east of the TP. They are highly sensitive to changes in air temperature because the maximum accumulation and ablation occur simultaneously. Thus higher summer temperatures will increase melt and rainfall directly and strongly affect the energy budget due to the positive albedo feedback mechanism (Fujita 2008a; Fujita 2008b; Fujita et al. 2007). The winter-accumulation-type glaciers are located in the western part of the TP with its adjacent mountain ranges. They receive their mass gain mainly from the winter westerlies, show a distinct accumulation and ablation season and are less sensitive to air temperature change Fujita (2008a). Maussion et al. (2014a) introduced a glacier classification based on precipitation seasonality revealed through a cluster analysis of model data (Fig. 3.5). Since temperatures on the TP are generally low and summer precipitation falls mainly as snow this classification can be translated into accumulation regimes as well. Summer-precipitation-type (JJA) glaciers cover larger parts of the southern TP including the central part of the Transhimalayas. The winter-precipitation-type (DJF) can be assigned to large parts of the Karakorum, Pamir and eastern-most parts of the Himalayas. In large areas within the Himalayas and the north-eastern part of the central TP the precipitation regimes seem to vary within short distance. Here mixed precipitation classes of MAM/DJF and MAM/JJA mainly occur. Exposition and the topographic surroundings with respect to the wind direction seem to play a significant role (Maussion et al. 2014a). Along the north-western fringe of the plateau the spring-precipitation-regime is dominant (Fig. 3.5).

Due to the lack of in-situ data and sparsely conducted remote sensing and model approaches to study glaciers on the TP several little-known factors about the glacier – atmosphere interaction in general limit our knowledge of recent developments and thus about future predictions (Cogley et al. 2011). The local factors include the role of debris cover, superimposed ice, aerosols, snow drift, overall velocity and surging of glaciers. Fujita et al. (1996) point out that the formation of superimposed ice at the ice-snow interface compensates for much the superficial melt during the ablation period. Debris cover tends to protect the glacier from insolation (Scherler et al. 2011; Bolch et al. 2012). However finer supraglacial deposit like dust and black carbon reduces the albedo and increases ablation (Flanner and Zenner 2005; Qu et al. 2014).

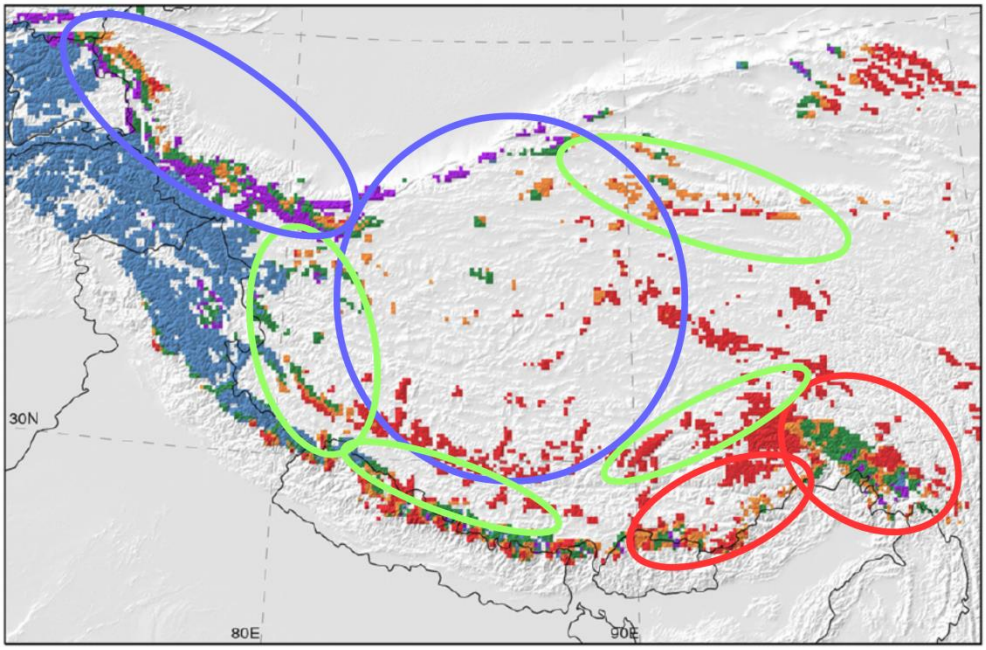

Fig. 3.5: Classification of glaciers on the Tibetan Plateau. Classification of glacier accumulation regimes according to precipitation seasonality shown as coloured areas, DJF (blue), DJF/MAM (green), MAM (violet), MAM/JJA (orange) and JJA (red) (Maussion et al. 2014a). Classification according to continentality is shown as coloured circles with maritime (red), subcontinental (green) and extremely continental (blue) after Shi and Lui 2000.

3.3 Climate Change on the TP and consequences for glaciers of the TP

Climate change on the TP since the 20th century can be revealed from meteorological observations as well as from satellite data. Many studies based on observational data agree on a trend towards higher air temperature since the 1950, accelerating since the 1980s and with highest increases in winter (Liu and Chen 2000; Ding et al. 2006; Yang et al. 2009; You et al. 2010; Xue et al. 2009; Wei and Fang 2013; Yang et al. 2014). Considerable air temperature increase is also apparent in the summer months in the south-eastern and north-eastern TP between 1996 and 2010 (Yang et al. 2015). Spatially, the largest warming trends can be identified in the central, north-western and north-eastern plateau regions (You et al. 2010; Wei and Fang 2013). The rate of warming in 1955–1996 increased from 3000 to 4000 m a.s.l. and stayed stable with altitude above that height (Liu and Chen 2000). Wei and Fang (2013) show that this pattern was predominant on the TP from 1961 to

2010. In the last years the warming trend of the altitudes below 4000 m a.s.l. accelerated and exceeded those of higher altitudes making the Quaidam basin the region with highest warming rates on the TP (Wei and Fang 2013; Wang et al. 2014). Due to a lack of reliable data above 5000 m a.s.l. the existence of an elevational dependency of glacier mass loss are in question (Kang et al. 2010).

Accompanying the warming is air moistening, which favours more deep-clouds, which again results in solar dimming (Yang et al. 2014). However, trends in precipitation on the TP are less clear. Overall, precipitation observations show small decreasing trends from 1961-2008, but generally increasing trends in the winter months (Li et al. 2010). Climates of endhoretic lakes hint toward warmer and wetter conditions (Liu et al. 2009; Yang et al. 2014). Increasing precipitation is shown in eastern Pamir and north-western part of the TP (Ding et al. 2006; Yao et al. 2012) while decreasing precipitation is found in the Hindukush-Karakorum-Himalaya region (Palazzi et al. 2013). During the summer months an increase in precipitation is found for the north-eastern TP whereas the monsoonal influenced areas in the south-east show decreased precipitation between 1996 and 2010 (Yang et al. 2015). The complex terrain decreases the reliability of available global meteorological datasets with coarse resolution, especially for precipitation (You et al. 2012).

In accordance with the warming trend mean wind speed shows a decreasing trend at most stations (Yang et al. 2014; You et al. 2014). Gao et al. (2014) exposed a northward shift of the mid-latitude westerly jet. Wind speed seems to be negatively correlated with temperature and cloud coverage. Over large parts of the central plateau higher wind speed is correlated to less precipitation in early summer (Mölg et al. 2014).

Recent studies found a weakening of the Indian monsoon and a strengthening of the westerlies (Wu 2005; Zhao et al. 2012). However, increasing of the monsoonal precipitation amount is likely to go along with the overall temperature increase (Gao et al. 2014).

In response to climate warming surface glacier melt might accelerate, glacier flow might increase and glacier mass loss might be intensified (Yasuda and Furuya 2012). Concerning different thermal glacier types it is apparent that the area and volume decrease is largest for the temperate glaciers and smallest for the cold glaciers (Yao et al. 2012). Due to the lack of in situ data glacier status and changes on the TP are comparatively not well known (Gardner et al. 2013). Overall studies reveal glacier mass loss on the TP (Kääb et al. 2012; Mölg et al. 2012; Yao et al. 2012; Gardelle et al. 2013; Gardner et al. 2013; Mölg et al. 2014; Neckel et al. 2014; Wei et al. 2014). Also continental glaciers are found to increase their movement and loose mass while ice caps rather tent to maintain their stable status (Yan et al. 2015). The so called ‘Karakorum anomaly’, as introduced by Hewitt et al. (2005), describes the fact that slight positive MB are measured recently on glaciers in the Pamirs, Karakorum and Western Kunlun Shan (Gardelle et al. 2013; Gardner et al. 2013; Neckel et al. 2014; Kääb et al. 2015).

3.4 Methodical background

The methods used in this thesis are mainly remote sensing based. Furthermore, the studies in this thesis partly rely on surface energy and glacier mass balance (MB) modelling. This chapter aims to clarify the underlying physical processes and the consideration of suitable remote sensing data for the approaches of the thesis.

3.4.1 Glacier mass balance, equilibrium-line altitude and their climatic influences

The MB describes the change of the mass of the glacier, or part of the glacier, over a stated period (Cogley et al. 2011). The annual glacier-wide MB is the sum of accumulation and ablation over the mass balance year. The mass balance year is also called glaciological year. It comprises the duration of one calendar year and is adjusted to the study region usually equalling the local hydrological year starting with the beginning of the accumulation season (Cogley et al. 2011). For the glaciers on the TP we utilize a glaciological year from 01 October to 30 September.

The transient snow line on a glacier is the visible line separating areas free of snow (ice or firn) from snow covered glacier surface at every point in time. The concept of the equilibrium line of a glacier is the set of points on the glacier surface where the MB is zero. This line separates the area of accumulation from the area of ablation on the glacier and often varies in altitude across a glacier. The spatially averaged altitude of the equilibrium line is the equilibrium-line altitude (ELA). At the annual ELA the annual MB is zero. Changes in the ELA may be a good measure of the impact of climate variations (Hooke 2005). Annual ELAs reflect solely the situation in the year of observation and may be highly variable over longer periods. In this thesis ELA is referred to as the annual ELA applying to the glaciological year if not stated otherwise. The ELA can be used as a proxy for the mass balance of a glacier since MB and ELA for individual glaciers are usually strongly correlated (Zhang et al. 1998; Braithwaite and Raper 2010; Cogley et al. 2011; Shea et al. 2013; Brun et al. 2015).

In the absence of field data there are a few methods on how to indirectly approximate the ELA of present-day glaciers. The convex–concave surface transition assuming the convex surface of the ablation area and the concave form within an accumulation area (Benn and Evans 2010), the accumulation-area ratio assuming a linear relationship between the sizes of the accumulation and ablation areas of glaciers (Porter 1975), different versions of the toe-to-summit ratio method assuming ELA represents a regional ratio between the highest and lowest points of a glacier (Höfer 1879; Louis 1955; Loibl et al. 2014) and the median altitude of the glacier (Braithwaite and Raper 2010; Sakai et al 2015). All of these methods rely on the assumption of an ELA of a steady state glacier. A steady state describes the state of a glacier with a glacier-wide MB of zero over many subsequent years (Cogley et al. 2011). Since modern glaciers on the TP are subject to ongoing climate and mass balance change (cf. chapter 3.3) the listed approaches are not suitable for this thesis' aims. Furthermore, many of the approaches look at ELAs of individual glaciers which are strongly influenced by local topography and micro climate. Conversely, a regional ELA integrates averaged data from multiple glaciers, providing a more general measurement which is less prone to local effects.

Linking the ELA with the visible snow line enables the remote sensing approach used in this thesis (Fig. 3.5). The highest transient snowline within the glaciological year coincides with the annual ELA if there is no superimposed ice present (Cogley et al. 2011; Pelto 2011; Fig. 3.6). Thus, the end-of-ablation or end-of-summer-snow line can be used as an ELA proxy (Shea et al. 2013; Brun et al. 2015).

Roughly the influences of climate parameters can be considered separately in surface energy and the MB components. The near-surface layer is an interface which links atmospheric processes and the glacier body and cannot store relevant amounts of energy (Huintjes 2014). The energy exchange within this layer is governed by the energy fluxes as presented in Fig. 3.7. As commonly defined in the discipline of glaciology, a positive sign indicates an energy gain to the glacier surface, a negative sign an energy loss (Hock 2005). As within the general energy balance of the earth, the incoming

solar shortwave radiation and the longwave radiation emitted by the earth and its atmosphere play a major role in the glacier surface energy balance (Oerlemans 2010). Additionally important are the turbulent fluxes within the atmospheric boundary layer.

The incoming shortwave radiation (SW_{in}) depends on the position of the sun, topography and resulting sun angle, the structure of the atmosphere and cloud cover. The outgoing shortwave (SW_{out}) radiation additionally depends on the albedo determining how much of the incoming shortwave radiation is reflected by the surface (Oerlemans 2010). The outgoing longwave radiation (LW_{out}) is emitted by the surface and primarily depends on the glacier surface temperature according to the law of Stefan and Boltzmann. Incoming longwave radiation (LW_{in}) increases with increasing air temperature, air humidity and cloud cover. Topography can also influence LW_{in} due to emission from surrounding slopes. Normally LW_{out} is larger than LW_{in} resulting in negative net longwave radiation (LW_{net}) (Oerlemans 2010).

The turbulent fluxes occur within the boundary layer when no stable conditions exist. They consist of sensible (Q_{sens}) and latent heat flux (Q_{lat}). While Q_{sens} is controlled by the temperature gradient, Q_{lat} is driven by the vapour pressure gradient between glacier surface and the boundary air layer (Oerlemans 2010). Q_{sens} describes the direct heat transport to or from the surface. Q_{lat} is the indirect heat transfer connected to sublimation and/or evaporation or resublimation and/or condensation on a glacier surface. The ground heat flux and the heat transfer due to rain on the glacier surface are small (Oerlemans 2010) and are not specifically discussed within this thesis. If the sum of all fluxes, the surface energy balance (SEB), is positive the energy heats the surface layer until it reaches its melting point. The energy surplus beyond that point is used for melting of snow and/or ice at the surface (Hock 2005; Huintjes 2014).

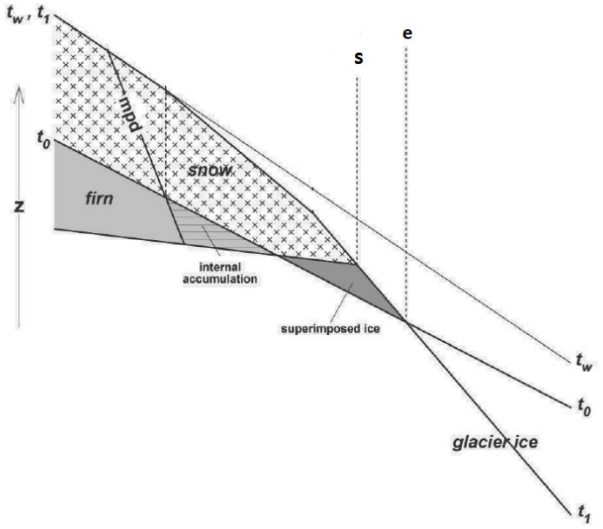

Fig. 3.6: Zones, snow line (s) and equilibrium line (e) on a cold or polythermal glacier. The summer surface t_0- t_0 at the begin of the mass balance year, the surface t_w- t_w at the end of the accumulation season and t_1- t_1 at the end of the ablation season. Mpd indicates the maximum depth to where the meltwater perculates before refreezing. Modified after Cogley et al. 2011.

The processes of melting and sublimation couple the surface energy balance to the MB. Within this thesis the MB refers to the climatic MB. The climatic MB is the combination of surface MB and internal MB (Cogley et al. 2011). Different components and influencing factors add or discharge mass

from the glacier (Fig. 3.8). The surface mass balance considers all changes that occur within the layer above the last summer surface. The influencing processes are mainly melt and sublimation, accumulation of snow as well as snow drift. The internal MB refers to all processes adding or removing mass from the glacier's interior. These are mainly percolation of melt water and refreezing beneath the summer surface in the firn. Both parts of the climatic MB are induced by climatic conditions (Cogley et al. 2011).

There are different methods to measure the MB of a glacier. Within this thesis MB proxies are estimated using snow line altitudes derived by a remote sensing approach. In chapter 6 a physically based coupled snowpack and ice surface energy and MB model (COSIMA; Huintjes 2014; Huintjes et al. 2015a) is used. COSIMA and other glacier models applied on the TP do not incorporate debris cover, superimposed ice, aerosols, snow drift, overall velocity and surging of glaciers. Due to the lack of knowledge and the complexity of the physical processes these factors cannot easily be parameterized in the modelling approaches (cf. chapter 3.2). Remote sensing and modelling belong to the indirect methods to measure the MB of a glacier. Other commonly used methods are the glaciological, the geodetic (cf. chapter 3.4.2), the hydrological and the flux-method (Kaser et al. 2003) which are not further discussed here.

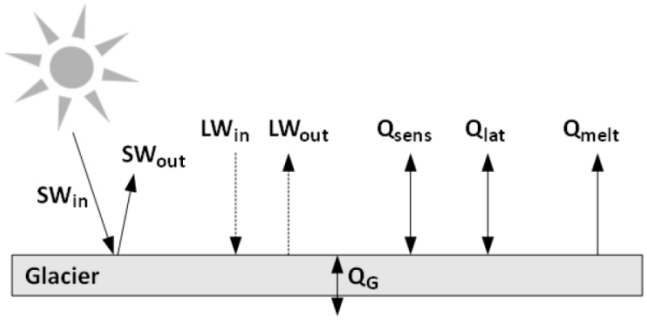

Fig. 3.7: Energy fluxes governing the near-surface layer above the glacier surface (Huintjes 2014). Incoming shortwave radiation (SW_{in}), outgoing shortwave radiation (SW_{out}), incoming longwave radiation (LW_{in}), outgoing longwave radiation (LW_{out}), ground heat flux (Q_G), sensible heat flux (Q_{sens}), latent heat flux (Q_{lat}) and melt energy (Q_{melt}).

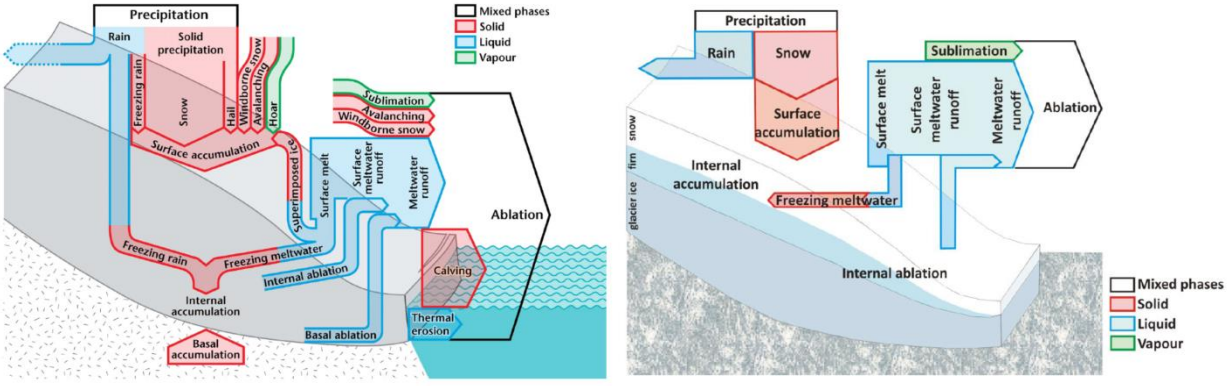

Fig. 3.8: Components of glacier mass balance after Cogley et al. 2011 (left) and as considered in the MB model applied in this thesis in Chapter 6 (right, Huintjes 2014). The arrows widths serve as illustration and do not indicate physical pathways of mass transfer.

In this thesis the reference-surface balance, which refers to an unchanged glacier surface altitude and surface area over the entire period, is used. Calculation within the remote sensing approach and the modelling approach assume an unchanged glacier area within the observation period. In reality, the glacier surface altitude and surface area might change due to topographic feedback mechanisms and ice flow dynamics (Cogley et al. 2011). However, since the reference-surface balance does not incorporate changes in glacier hypsometry it is more suitable to study climate forcing of a glacier (Hooke 2005; Cogley et al. 2011).

3.4.2 Remote sensing methods regarding glacier MB

It follows a short overview of remote sensing approaches focussing on applications concerning glacier MB studies. For a comprehensive study of the basics of remote sensing technics please be referred to for example Hall et al. (1985), Hall (2012), Rees et al. (2005), Dietz et al. (2012) or Carsey (1992).

Remote sensing can be interpreted as observing an object without physical contact with it. Usually it is referred to airborne or space borne observations using electromagnetic radiation. Passive remote sensing as utilized in this thesis is measuring naturally occurring radiation. Naturally occurring radiation consists of reflected solar radiation and terrestrial longwave radiation. The reflected solar radiation is largely confined to the visible and near-infrared parts of the electromagnetic spectrum. Active remote sensing makes use of generating radiation by the remote sensing instrument itself and measures the reflected radiation (Rees 2005). The general difficulties of remote sensing approaches in high mountainous areas are the rugged topography and steepness which complicates the exact display of the surface area and can lead to shading effects.

Precise topographic maps and accurate aerial imagery or air borne laser measurements (Light detection and ranging (LIDAR)) are not commonly available for remote areas as the TP (Kääb 2005). Hence in the following it is focussed on space borne remote sensing where sensors are mounted on-board a satellite or space shuttle. Remote sensing studies concerning glacier MB focus on either area or volume change or change in mass. The velocity of a glacier can be studied by remote sensing methods like feature tracking (e.g. Yasuda and Furuya 2012; Yan et al. 2015) or interferometry. These approaches will not be further discussed within this thesis.

Glacier area change

Change rates of glacier area can be interpreted as advancing or retreating glacier with an inference to prevailing climatic forcing. Area changes can be derived by manual digitization or automated unsupervised and supervised classifications of multispectral images (Paul et al. 2002). For debris covered glaciers multispectral analysis can be combined with a digital elevation model (DEM) (Paul et al. 2004). These methods are also used to create glacier inventories. The global Randolph Glacier Inventory (RGI; Arendt et al. 2014) is a comprehensive merged product. In many areas on the TP it is superior to earlier products as Global Land Ice Measurements from Space (GLIMS; Bishop et al. 2004) and the Chinese Glacier Inventory (CGI; Shi et al. 2009).

Appropriate sensors for these methods are TM/ETM+ on Landsat satellites, HRV/HRVIR on Satellites Pour l'Observation de la Terre or Earth-observing Satellites (SPOT)), Advanced Spaceborne Thermal Emission and Reflection Radiometer (ASTER) on Terra satellite, Advanced Very High Resolution Radiometer (AVHRR) on Metop-A/NOAA-15 satellites. Glacier area change studies on the TP have

been carried out based on historical maps, Landsat and ASTER data (e.g. Liu et al. 2004; Shangguan 2004; Shangguan 2005; Shangguan 2006; Bolch et al. 2010; Wei et al. 2014).

Data voids due to cloud cover do affect all optical images. Uncertainties in snow detection arise since snow has a similar reflectance structure as clouds. Changes in the glacier mass may not necessarily be reflected by glacier area change. Surging events or ice avalanches which might be connected to warming can lead to an 'advance' of the glacier. In interpreting the advance or retreat of a glacier one has to further bear in mind its reaction time. The reaction time is the time required for a change in forcing of mass balance to result in an observable response of the geometry of the glacier (Cogley et al. 2011). Hence the area change is used as an integral measure of multiannual aggregated change of the MB rather than a proxy for interannual variability.

Geodetic method

While glacier area and length changes can be derived relatively easily from remote sensing imagery only changes in glacier thickness can directly be related to glacier mass changes. Geodetic methods determine glacier MB by the volumetric change of the ice mass through time from repeated and combined mapping of the surface area and the surface elevation (Hubbard and Glasser 2005). Volume change of glaciers is done by DEM differencing (Rees et al. 2005). DEMs can be produced utilizing a wide variety of datatypes and with varying methodologies. However, there are three broad categories: stereo imagery, InSAR (interferometric synthetic aperture radar) and altimeters based on laser or radar (Pope et al. 2014).

Appropriate space-borne sensors for stereo imagery are High Resolution Stereoscopic (HRS) on SPOT satellites and ASTER on the Terra satellite. A widely used InSAR sensor was the SIR-C/X-SAR on the Shuttle Radar Topography Mission (SRTM). Common radar altimeters are SAR-X on TerraSAR-X and TanDEM-X. Geoscience Laser Altimeter System (GLAS) instrument aboard the NASA Ice, Cloud, and land Elevation (ICESat) satellite is a space borne laser altimeter (Dietz et al. 2012; Pope et al. 2014). Glacier MB studies using the geodetic method on the TP have been published e.g. by Bolch et al. 2012, Gardelle et al. 2013, Neckel et al. 2013, Neckel et al. 2014 and Holzer et al. 2015.

By DEM differencing spatial information on thickening or thinning of glaciers can be derived. Radar and laser supply valuable data at day and night and in all weather conditions for creating DEMs. The conversion from volume or elevation change to MB values can be achieved with information on the density of the lost or gained mass (Cogley et al. 2011). In study areas without in-situ measurements the density of snow and firn has to be approximated, which is one of the largest error sources in the conversion (Pritchard et al. 2010; Neckel et al. 2013; Neckel et al. 2014). Another relevant error source is the radar penetration depth, depending on surface and wavelength (Gardelle et al. 2012; Kääb et al. 2012; Kääb et al. 2015). The regional averaged volume change can be derived between the two acquisition dates of the DEM. Thus DEM differencing does not provide annual MB proxies.

Gravimetry

Direct measurements of glacier mass change can be achieved by methods of gravimetry. Until now this has been applied widely only within the Gravity Recovery And Climate Experiment (GRACE). The GRACE mission was launched in 2002 and measures earth's gravity field anomalies (e.g. Swenson et al. 2002; Jacob et al. 2012). Since gravity is determined by mass, gravity anomalies can show how mass is spatially distributed. Analysis of GRACE derived monthly averaged regional distribution of water revealed mass gain on the TB between 2003 and 2010 (Jacob et al. 2012), which initially has

been attributed to positive glacier mass balances by the authors. However this mass gain was found to likely arise from the increased water within endorheic lakes on the drainless parts of the plateau (Zhang et al. 2013).

Methods used in this study

The focus of this thesis is to derive an annual MB proxy time series for remote glaciers on the TP. The introduced analysis of glacier area change and the geodetic method usually provide multiannual MB proxies, which again provides information on long-term glacier changes only. However, the aim of the thesis is to derive annual ELA proxies which then can be linked to the glacier MB (cf. 3.4.1). Therefore, the progression and altitude of transient snow lines at the end of ablation period was investigated here.

The detection of snow cover is a common approach in remote sensing. The underlying concept is the reflectance differences of different surfaces. These differences are captured by measurements of multispectral sensors. The commonly used normalized-difference snow index (NDSI) makes use of the different spectral reflectance characteristics of snow and ice versus non-snow-covered surfaces and clouds in visible and shortwave infrared (IR) wavebands (Hall et al. 2002; Pepe et al. 2005). Instruments that provide freely available data for snow mapping with a spatial resolution of at least 1500 m are shown in Table 3.1.

In deciding on the data basis three criteria for the selection arose: temporal and spatial resolution as well as the inherent possibility to differentiate between snow, ice and clouds. Firstly, a preferably long time series with a high temporal resolution is desired. To derive the highest SLA within the end of the ablation period we look at a period of less than 100 subsequent days in each year. To display an informative progression of the transient snow lines and to increase the possibility to portray the true highest position of the strongly variable transient snow line daily data coverage is desirable. Even more since the rate of impracticality of optical data due to cloud coverage is empirically quite high. The spatial resolution of the data needs to be as high as to display adequately resolved glacierized areas. Within the scope of this thesis regional MB proxy were focussed on. Nevertheless, the terminus of the individual glaciers within a region still needs to be represented within the spatial data resolution. The study region in chapter 4 comprises glacier tongues that are at least 500 m wide. Studied regions discussed in chapter 5 comprise glacier tongues with widths less than 500 m wide. In consequence, the requirement for the spatial resolution is to be at least 500 m. To derive transient snow lines the method needs to differentiate between snow and ice covered surfaces. Manually digitization of the snow line can be done applying a spectral band ratio of multispectral data which makes the snow line visible. Within this thesis a visibility is derived using a RGB color image created from Landsat band ratios of bands 5, 4 and 3 (e.g. Fig. 4.7, Fig. 6.5).

Table 3.1: Freely available data appropriate for snow mapping with a spatial resolution higher than 1500 m.

Satellite	Instrument	Number spectral bands	Maximal spatial resolution [m]	Temporal resolution	Temporal coverage
Landsat	TM/ETM+	7	30	every 16 days	1982 - ongoing
SPOT 4/5	HRV/HRVIR	4	10	every 26 days	1998/2002 – 2010
Envisat	AATSR	3	1000	every 3 days	2002-2012
Envisat	MERIS	15	300	every 3 days	2002-2012

Metop/NOAA	AVHRR	6	1100	daily	2006 - ongoing
Terra/Aqua	MODIS	36	250	twice a day	2000 - ongoing

Generally, remote sensing methods using optical data are suitable to detect snow/ice cover as described earlier. The automated snow mapping algorithms based on NDSI detect snow and ice. A differentiation between snow and ice, on the other hand, can be done by using the difference in albedo, which is defined as the broadband hemispherical averaged reflectance in the spectral range 300 to 2800 nm (Brock et al. 2000), or by using the difference in multispectral reflectance (Fig. 3.9). To fixate a characteristic albedo of snow and ice is difficult since it is influenced by grain size and impurities (Dumont et al. 2011; Dietz et al. 2012). Nevertheless approximations proved to be valuable (Hall and Martinec 1985; Paterson and Cuffey 1994).

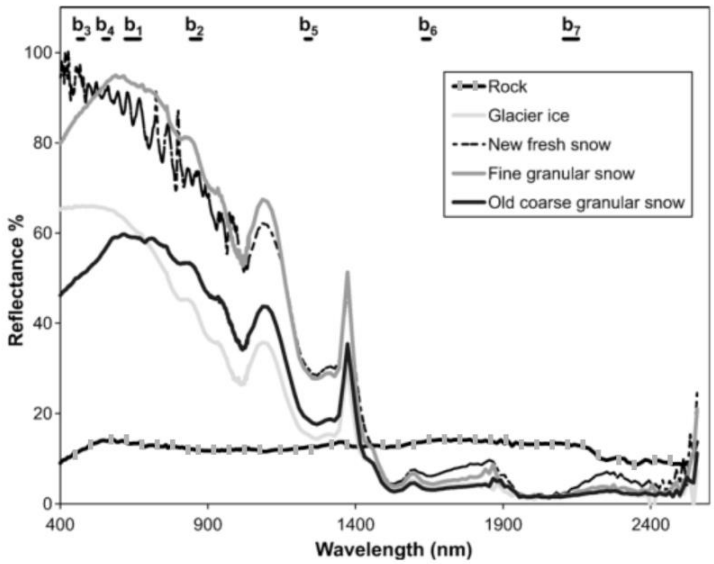

Fig. 3.9: Reflectance characteristic of different surfaces in the visible to near infrared light. Spectral bands of Moderate resolution Imaging Spektroradiometer (MODIS) indicated on the top of the figure (modified after Lopez et al. 2008).

The decision on a data basis while keeping the mentioned criteria in mind results in following evaluations. Landsat products are most easily to obtain and provide a good theoretical spatial resolution. Nevertheless, Landsat 7 scenes have data gaps due to the Scan Line Corrector (SLC) failure since 2003 (Pfeffer et al. 2014) and their temporal resolution is only moderate (Table 3.1). SPOT imagery provides a good spatial resolution, but the temporal resolution is not sufficient. SPOT images were made freely available only in 2014 (up to five years in the past). The Globsnow snow extent product mainly based on the Envisat instruments is not suitable for rugged mountainous regions because of its course resolution (Metsämäki et al. 2015). Likewise spatial resolution provided by AVHRR is insufficient. Pepe et al. (2005) derived a snow cover product with a good spatial and temporal resolution using a supervised fuzzy statistical classification using Medium Resolution Imaging Spectrometer (MERIS) and Advanced Along-Track Scanning Radiometer *(*AATSR). Nevertheless, in choosing Moderate resolution Imaging Spektroradiometer (MODIS) data we rely on widely used data in glaciological studies (Lopez et al. 2008; Möller et al. 2011; Pelto et al. 2011; Dumont et al. 2012; Shea et al. 2013; Pope et al. 2014; Brun et al. 2015). The favourable combination of feasible spatial and temporal resolution of the MODIS data represents the best choice in the scope

of the study. MODIS raw data provide atmosphere corrected reflectance data using a super spectral imaging sensor with 36 spectral channels. The bands have narrower bandwidths, enabling the finer spectral characteristics of the targets to be captured by the sensor (chapter 5 and 6). The quality assessed MODIS snow product has a spatial resolution of 500 m with inherent albedo values to differentiate snow and ice (chapter 4). The MODIS snow mapping algorithm uses a grouped-criteria technique with NDSI and other spectral threshold tests. The biggest drawback of MODIS data are data gaps due to cloud cover. However MODIS provides a compatible cloud mask with a reasonable resolution of 500 m.

4 MODIS derived equilibrium-line altitude estimates for Purogangri Ice Cap, Tibetan Plateau, and their relation to climatic predictors (2001-2012)

The variation of the equilibrium-line altitude (ELA) can be used as indicator for glacier mass balance variability. Snow lines at the end of the ablation period are suitable proxies for the annual ELA on glaciers. We investigate snow lines at Purogangri ice cap on the central Plateau in order to study the interannual variability of glacier mass balance. Datasets of the daily Moderate Resolution Imaging Spectroradiometer (MODIS) snow product MOD10A1 were used to infer transient snow line variability during 2001-2012 and to derive regional-scale, annual ELA. The MODIS snow albedo embedded within the snow product was compared to high resolution Landsat imagery. An albedo threshold was established to differentiate between ice and snow and the 13th percentile of the altitudes of snow-covered pixels was chosen to represent the snow line altitude. The second maximum of the snow line altitudes in the ablation period was taken as a proxy for the annual ELA. A linear correlation analysis was carried out a) between interannual variability of the ELA at Purogangri ice cap and various climate elements derived from the High Asia Reanalysis and b) between interannual variability of the ELA and the circulation indices North Atlantic Oscillation and Indian Summer Monsoon. Results suggest that air temperature and meridional wind speed above ground in July, as well as the lower tropospheric zonal wind in June and August play a crucial role in the development of the annual ELA.

4.1 Introduction

The Tibetan Plateau is sometimes referred to as the “Third Pole” or the “Asian Water tower” (Qiu 2008; Immerzeel et al. 2010), underlining the importance of the highest and largest Plateau in the world. Indeed the glacierized areas on the plateau enclose important water resource. Most of the glaciers on the Central Plateau feed endorheic lakes (Neckel et al. 2014). These basins do not have outflow to the sea. Therefore, changes in water level in those basins do not affect global sea level. Their direct impact on the flora and fauna is important for the livelihood of local farmers. For example flooded pastures due to increasing lake levels in Selin Co (by up to 10.9%) and Nam Co region (by up to 2.2%) from 1970 to 2000 have been observed (Yao et al. 2007). An average positive trend of 0.31 m a^{-1} in the period 2000–2009 at Nam Co has been shown by Kropáček et al. (2012).

Over the past decades the Tibetan Plateau has shown distinct warming by 0.36/decade from 1960 to 2007 at stations on the TP (cf. Kang et al. 2010) and glacier retreat has been observed in many areas

of the Tibetan Plateau (Bolch et al. 2012; Yao et al. 2012 and Neckel et al. 2013). Regional differences in glacier change across the Tibetan Plateau are evident. Kääb et al. (2012) found negative glacier elevation trends for the Himalaya and slightly positive trends in the Karakoram between 2003 and 2008. Neckel et al. (2014) found negative mass budgets for the Qilian Mountains and eastern Kunlun Mountains while a mass gain was found in the westerly-dominated north-central part of the Tibetan Plateau between 2003 and 2009.

Due to the sparse coverage of meteorological stations and the difficulties in reaching most glaciers on the Plateau (Lei et al. 2012), remote sensing or modelling approaches are preferable methods in order to monitor Tibetan glacier change (Ye et al. 2006; Bolch et al. 2010; Liu et al. 2012; Yao et al. 2012; Neckel et al. 2014). Gapless time series of glacier mass balance fluctuations with high temporal resolution that enable the interpretation of recent glacier variability can be produced using mass balance- and energy balance models forced by atmospheric reanalysis data (e.g. Zhang et al. 1998; Mölg et al. 2012, 2014). Global remote sensing data sets are another straightforward option to obtain comparable time series with high temporal resolution concerning the status of glaciers (e.g. Dumont et al. 2012; Shea et al. 2013). Given the scarcity of ground-based glacier data, modelling and remote sensing approaches can be used to crosscheck, validate, and consolidate results, and improve interpretations of climate-glacier interactions on the Tibetan Plateau.

The aims of this study are to find a proxy for the interannual variation of glacier mass balance at Purogangri ice cap, northern central Tibetan Plateau by means of remote sensing and to analyse its connection to atmospheric circulation. Purogangri ice cap, in the northern central Tibetan Plateau was chosen as study site because of its size and its position relative to different atmospheric influences (Fig. 4.1). The possible application of the method in regions across the Plateau would enable a deeper understanding of regional patterns of climate forcing of glacier variability.

The equilibrium-line altitude (ELA) can be used as a proxy for the mass balance of a glacier (Zhang et al. 1998; Shea et al. 2013; Brun et al. 2015). The transient snow line, which can be tracked using remote-sensing approaches, equals the ELA at the end of the mass balance year if no superimposed ice was formed (Cogley et al. 2011). Hence, remote sensing-based snow line tracking can be used to derive information about the mass balance of glaciers.

4.1 Study site

Purogangri is Tibet's largest ice cap with over 390 km² of glacierized area (Yi et al. 2002; Shi et al. 2009; Neckel et al. 2013). The elevation of the glacierized area ranges from 5230 m a.s.l. to 6350 m a.s.l. At about 5900 m a.s.l. the ice cap forms a rather flat plateau which holds the largest part of the glacierized area (Fig. 4.2). The ice cap is located in the continental central part of the Tibetan Plateau (33.9°N, 89.1°E; Fig. 4.1; Thompson et al. 2006). It is located in the transition zone between the monsoon circulation and the westerlies. The region receives about 70% of its precipitation between May and September and is influenced by strong westerly winds during winter (Fig. 4.1; Maussion et al. 2014a).

So far, only few studies discussed glaciological issues related to Purogangri ice cap. Yi et al. (2002) studied quaternary glaciation by looking at geological features in the surrounding of the ice cap. Thompson et al. (2006) and Yao et al. (2006) studied paleoclimatic records from two ice cores taken on its main plateau. These studies reveal regionally different processes driving climate change on the Tibetan Plateau and an abrupt warming starting in the early 20th century which still continues today.

Yao et al. (2012) summarized a mean glacier retreat rate of 1.7 m a^{-1} at Purogangri from 1974 to 2010 and approximated a corresponding mean annual ELA to 5735 m a.s.l. Neckel et al. (2013) calculated the geodetic mass budget of −44 ± 15mm w.e. a^{-1} of the ice cap between 2000 and 2012 based on interferometry.

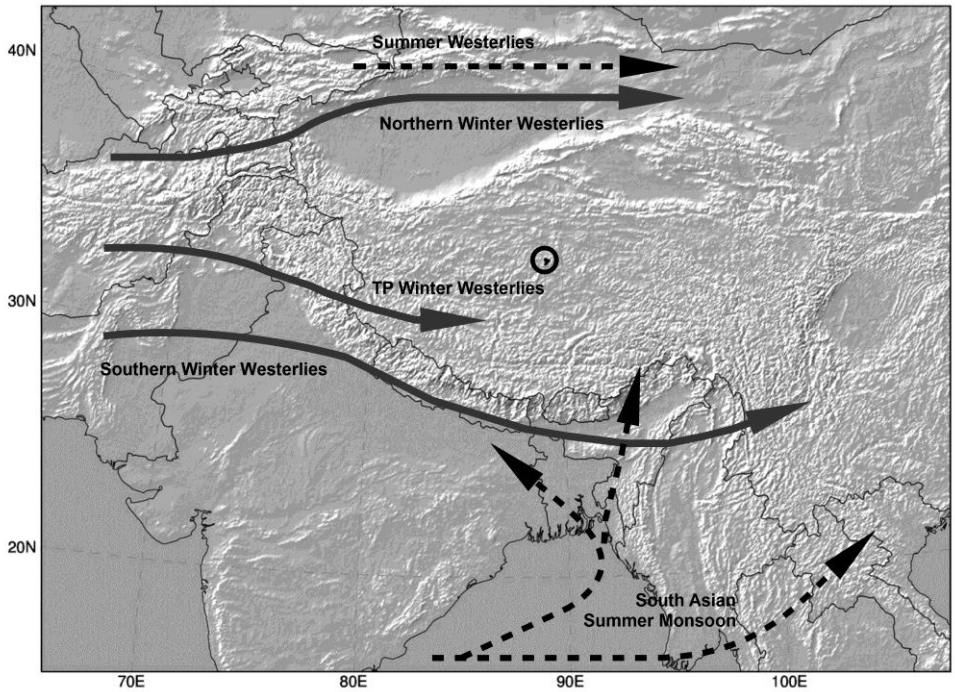

Fig. 4.1: The Tibetan Plateau and its integration into global circulation; westerlies in winter (continuous arrows), westerlies and monsoon circulation in summer (dotted arrows); location of the Purogangri ice cap (black circle); based on Bolch et al. (2012) and Yao et al. (2012).

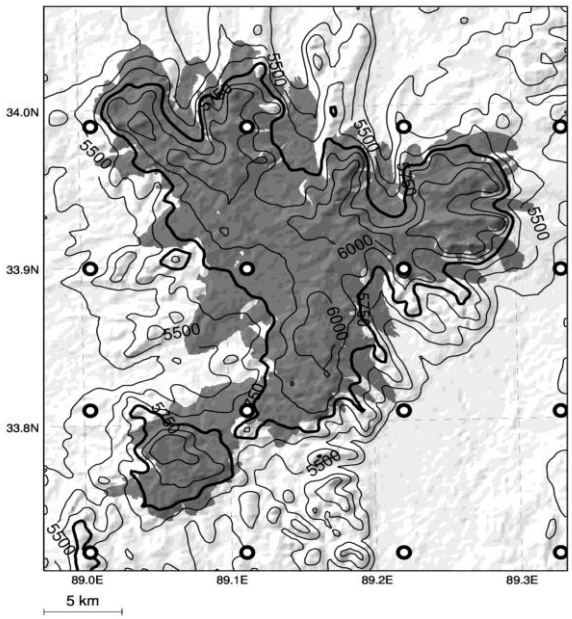

Fig. 4.2: Topographic map of Purogangri ice cap (grey) and its surroundings. Elevations are given in m a.s.l. and contour lines are drawn at intervals of 125 m. Contour line of anticipated ELA (5750 m a.s.l.) is thick. HAR grid points as circles.

4.2 Data

4.2.1 MODIS data

The Moderate Resolution Imaging Spectroradiometer (MODIS) snow product, version 5 (MOD10A1 and MYD10A1) provides a daily snow albedo dataset with embedded albedo values for pixels classified as snow within the snow product. For delineation of the transient snow line at high temporal resolution, we use these albedo values to conclude the surface type based on the reflectance feature. MODIS sensors on the Terra and Aqua satellites measure spectral radiance in 36 different bands. The Terra satellite crosses the Tibetan plateau around noon and provides data starting in 2001. The Aqua satellite crosses in the afternoon and its data cover the period from 2002 onwards (Hall et al. 2006). Daily snow albedo fields with a horizontal resolution of 500 m from the MODIS snow products MOD10A1 and MYD10A1 from 2001 to 2012 were used for this study. The MODIS snow cover products are automatically generated from bands 1 (0.659 µm), 2 (0.865 µm), 4 (0.555 µm) and 6 (1.64 µm) of the MODIS sensor and by incorporating cloud-cover data from the MOD35 cloud product (Hall et al. 1995). The generation procedure includes corrections of atmosphere and terrain-related influences. The MOD10A1 algorithm utilizes a Normalized Difference Snow Index (NDSI) for the binary snow classification. The MODIS snow classification as well as the land-classification do both potentially include ice surfaces. Debris cover is classified as land within the snow product. It does not contain albedo values and is therefore not considered for our calculation. The daily snow albedo is not a daily averaged albedo but the 'best' single observation in a day based on clouds, as well as viewing and illumination angles (Hall et al. 2007). The high temporal resolution and the thorough preprocessing of the data are favourable features in regard to data accessibility and off-the-shelf availability for this study.

The MOD10A1 and MYD10A1 calibrated and geolocated Level 3 MODIS product was provided by the NASA Distributed Active Archive Centre (DAAC) located at the National Snow and Ice Data Centre (NSIDC) (Hall et al. 2006).

4.2.2 Landsat Imagery, ASTER Digital Elevation Model and glacier mask

Cloud free Landsat scenes were used for validation of the MODIS derived snow lines. The requirement of a clearly visible snow line and simultaneous MODIS data availability of high quality in the study period was only fulfilled by one Landsat TM5 scene (15.08.2010, 1.30 pm local time, path 140, row 36). Landsat data were provided by the U.S. Geological Survey (USGS, http://earth explorer.usgs.gov/).

Terrain elevations were derived from the ASTER Global Digital Elevation Model (GDEM), Version 2. The ASTER GDEM is available from the NASA Land Processes Distributed Active Archive Center (LP DAAC, https://lpdaac.usgs.gov/) as a contribution of METI and NASA. Its spatial resolution is 30 m. We resampled the ASTER GDEM to 500 m resolution and coregistered it with the MODIS snow product scenes in order to derive one single altitude per MODIS pixel.

For calculation on glacier area we used a local glacier mask which was derived by conducting an unsupervised 2-class classification of Landsat ETM+ images from 2012 (Neckel et al. 2013).

4.2.3 Climate data

To study climatic influences on the ELA a correlation analysis is performed. A direct physical relation is expected between precipitation and the ELA as well as between temperature and the ELA since

both control melt and accumulation of snow. To track the atmospheric circulation wind speed, wind components and the water vapour mixing ratio were correlated as well. The teleconnection indices are used to track the large-scale climatic control of the mass balance of Purogangri ice cap. Namely we use the North Atlantic Oscillation (NAO) and the Indian Summer Monsoon (ISM) indices.

High Asia Refined analysis (HAR) data are provided by the Technical University of Berlin (Maussion et al. 2014a, http://www.klima.tu-berlin.de/HAR). For this study, mean monthly data with a spatial resolution of 10 km were used (HAR10). For the local climatic HAR variables, a region covering the extension of the glacierized area with a one pixel HAR margin is considered for the calculation of monthly mean values. This area corresponds to 40 x 50 km and a total of 20 pixels within the HAR dataset (cf. Fig. 4.2). The climate elements derived from the HAR dataset that are used as predictors in this study are 2 m air temperature (°C), precipitation (mm/h), wind speed (m/s) at 10 m above ground and at the 400 and 300 hPa levels as well as its zonal and meridional components (cf. Fig. 4.3a and Fig. 4.4a). Furthermore, the total amount of water vapour mixing ratio (g/kg) within the air column from the 500 to the 75 hPa level was used.

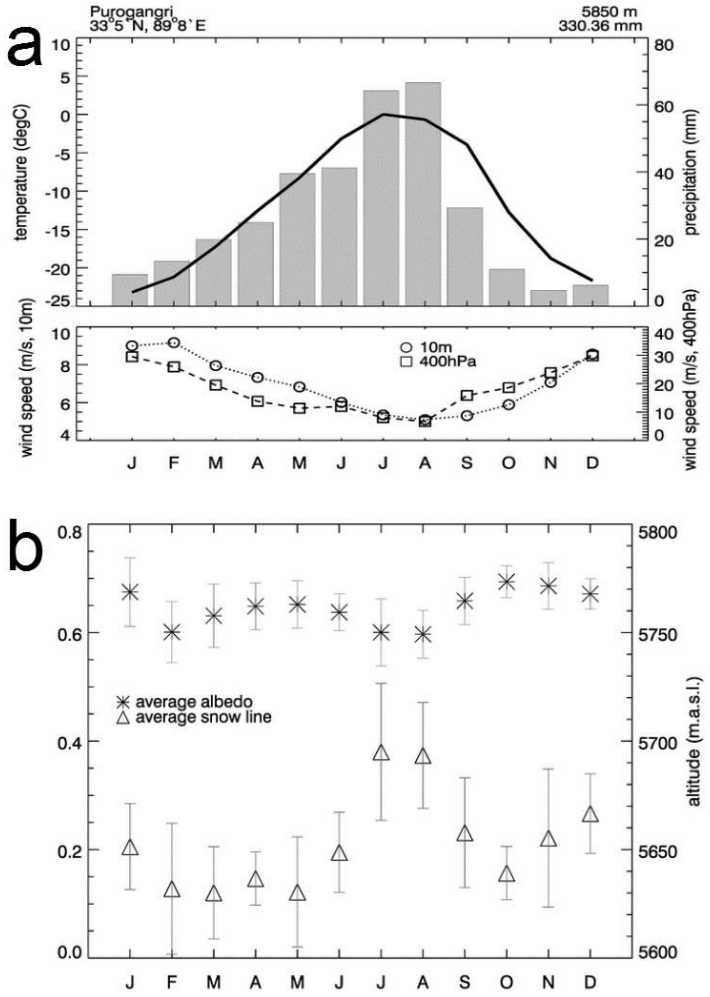

Fig. 4.3: HAR average annual cycle of temperature at the median of the glacier area altitude; precipitation (a, top), wind speed at 400hPa level and at 10 m above ground (a, bottom). Average annual cycle of albedo and monthly mean average snow line altitude; including scenes with a minimum of 10% data coverage within the glacier mask; ±sigma error bars (b).

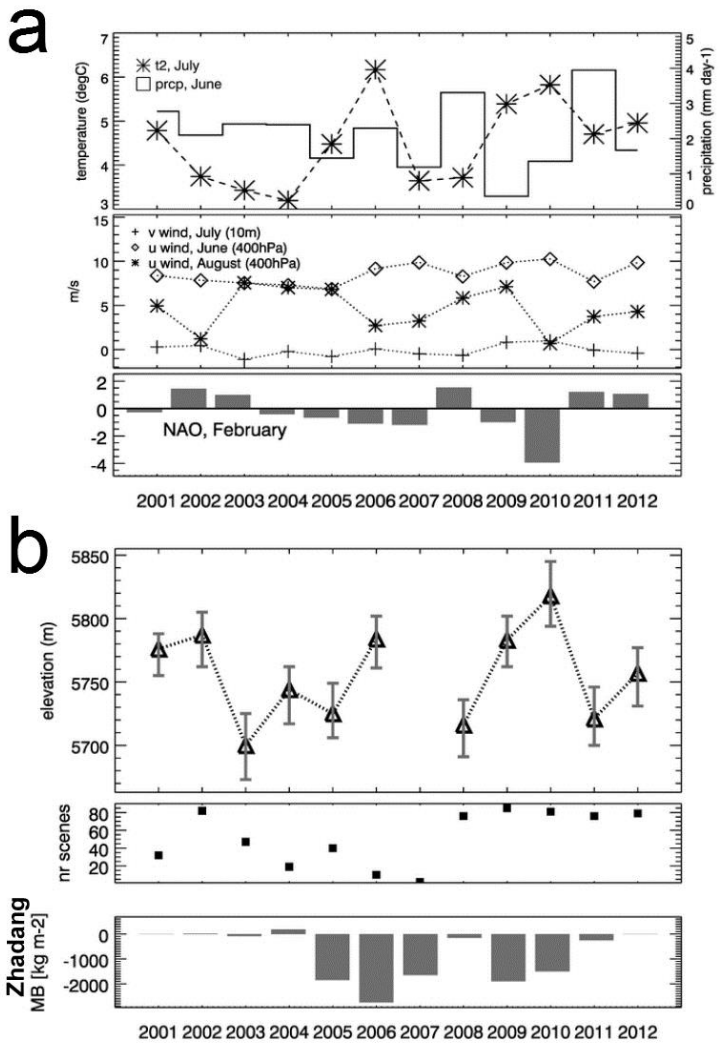

Fig. 4.4: Interannual variability of HAR annual mean temperature (July), annual mean precipitation (June) (a, top), v-wind above ground (July), u-wind at 400hPa level (June, August) (a, middle) and NAO in February (a, bottom). ELA at Purogangri calculated based on scenes ≥ 45% valid pixels with an albedo threshold of 38% using the 13th percentile of the resulting snow pixels (b, top), error bars display uncertainty including albedo threshold of 35 and 41% with respective application of the 10th and 16th percentile, number of scenes included in the calculation of the ELA (b, middle) and Mass Balance (MB) of Zhadang glacier after Mölg et al. 2014 (b, bottom).

The Hurrell North Atlantic Oscillation index (NAO) is calculated applying a principal component analysis of sea level pressure anomalies over the Atlantic sector, 20°-80°N, 90°W-40°E (Hurrell 2013). It is provided by the Climate Data Guide of the National Centre of Atmospheric Research (NCAR UCAR, https://climatedataguide.ucar.edu/climate-data/ hurrell-north-atlantic-oscillation-nao-index-pc-based). The Indian Summer Monsoon Index (ISM) is defined as the difference in the zonal wind speed at the 850 hPa level between 40°E-80°E, 5°N-15°N and 70°E-90°E, 20°N-30°N. It was obtained from the Asia Pacific Data Research Centre (APDRC, http://apdrc. soest.hawaii. edu/projects/monsoon/seasonal-monidx.html, 13 May 2014) where it was calculated using the NCEP NCAR Reanalysis data (Kalnay et al. 1996). A monsoon onset record is used as well (cf. Mölg et al. 2012). It is defined considering active and break periods of monsoon via a horizontal wind shear

index (HWSI), defined as the difference in the 850 hPa zonal wind between a northern (20-30°N, 70-90°E) and southern region (5-15°N, 40-80°E).

4.3 Method

In this study we used the daily MODIS snow products MOD10A1 and MYD10A1 (Hall et al. 2006) at a resolution of 500 m to calculate the regional transient snow lines. We then derived the ELA which in turn was used as a proxy for the mass balance (Fig. 4.5). Similar approaches by Brun et al. (2015), Shea et al. (2013) and Dumont et al. (2012) also work with this relation. The latter two rely on the higher spatial resolution MOD02QKM data. These approaches were adapted to the MODIS Level 3 snow product and the conditions of the Tibetan Plateau. The standard MODIS snow products offer a fast and simple approach, as the data are pre-processed and quality-assessed. The aim was a reliable overview of the development of the ELA in mountain areas on the Tibetan Plateau. This approach did not aim at the precise intraannual development of the transient snow line but rather at deriving the interannual variability of the annual ELA. As the coarse spatial resolution of the MODIS data does not allow to process data for individual glaciers we studied the ELA as the averaged altitude of the equilibrium line across Purogangri ice cap.

4.3.1 Preprocessing

Accounting for the known limitation of the MODIS snow product which mostly occurs due to cloud coverage (Hall et al. 2006) a set of preprocessing steps was performed to improve data coverage across the study area. The spatial coverage of the daily product was improved by combining Terra and Aqua scenes (Zhang et al. 2012). Whenever a pixel was classified as snow within one scene it was assumed to be snow covered in the other scene of the same day. The information of two scenes was merged into one image per day, increasing the data coverage from 57.3% (Terra) and 46.2% (Aqua) to 74.7% of the days in the considered time span.

A total of 1635 MODIS pixels lay within the glacier mask and were considered for further calculation. The snow albedo values were used in two filters to reduce the cloud cover and improve the data quality. A spatial cloud filter was applied to assign the mean albedo value of the surrounding pixels whenever more than two thirds of a 5x5 moving-window was classified as snow. A further temporal cloud filter assigns the mean albedo value of the subsequent days if they are classified as snow. If the subsequent days show no snow classification for this pixel the filter is extended to a five day period. The resulting improved snow classified pixels are used for the derivation of the snow line based on a threshold albedo. An example for the filter improvements can be seen in Fig. 4.6.

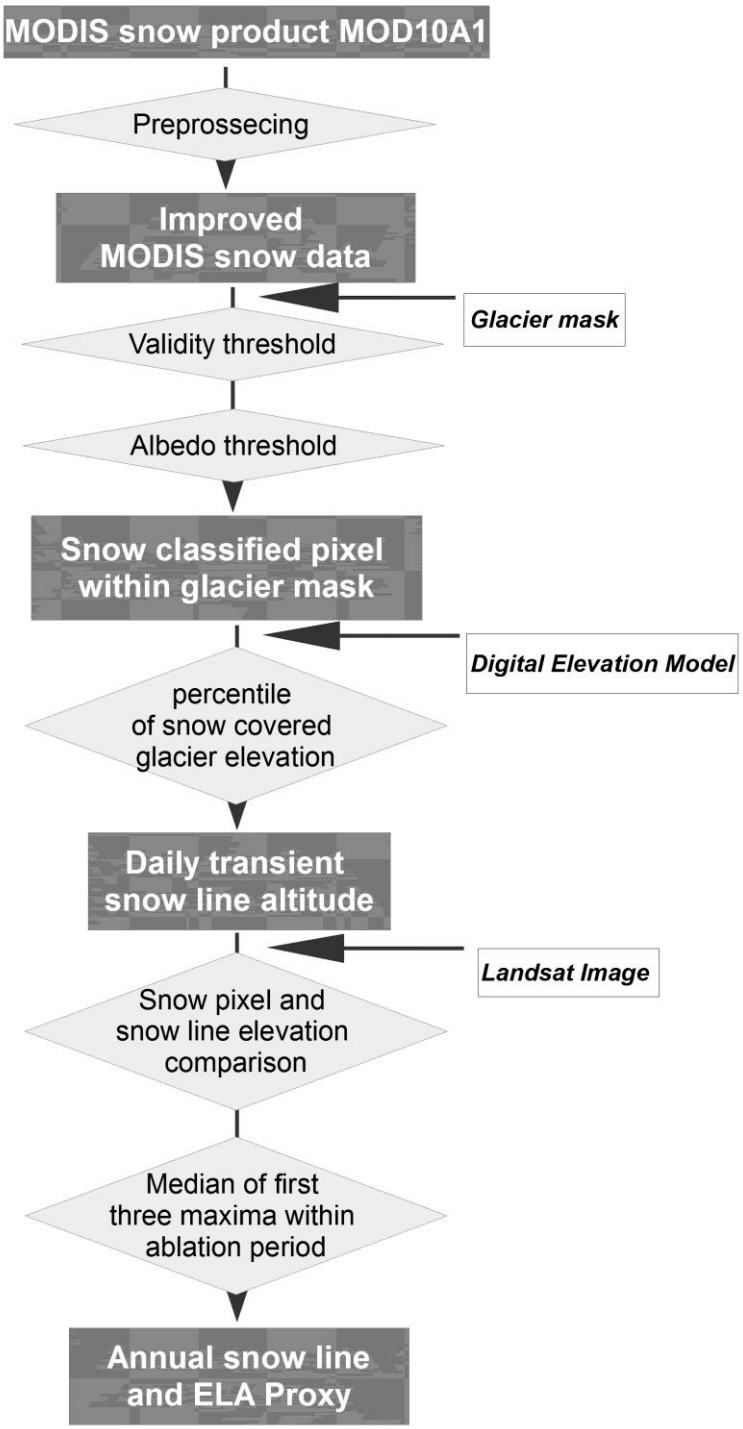

Fig. 4.5: Flow chart of the methodical procedure to derive interannual ELA variability; diamond shapes display processes, quadrats display outputs and boxes to the right display additional inputs.

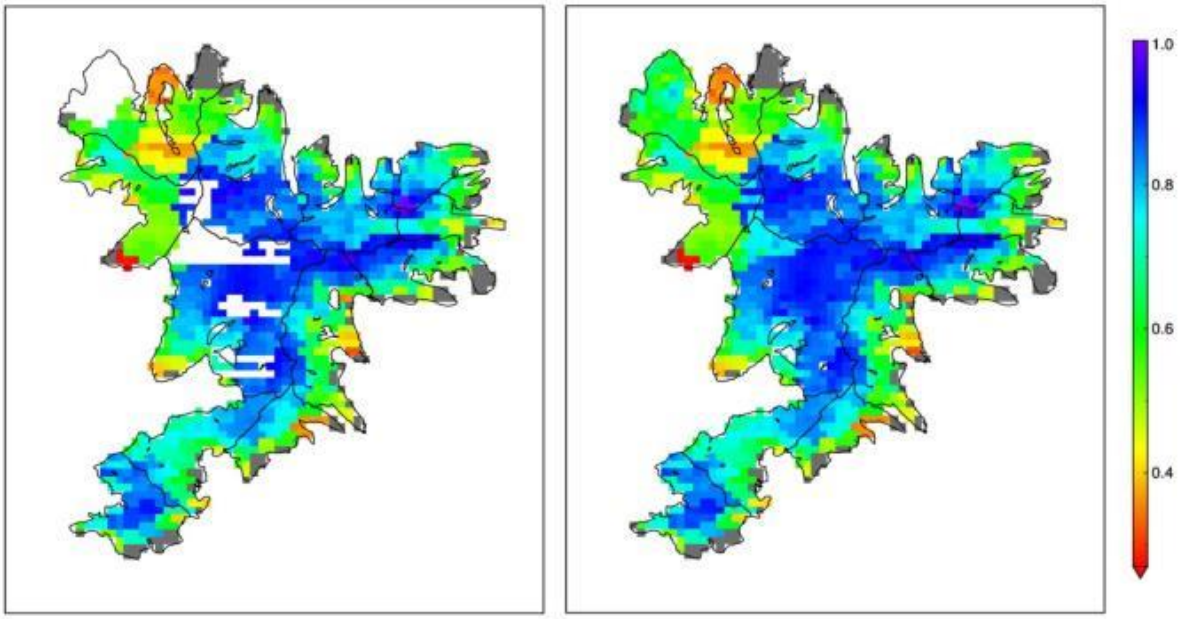

Fig. 4.6: MODIS snow product: snow classified pixels with albedo values and 'land' classified pixels (grey); original (left) and after the application of spatial and temporal filtering (right) to reduce the cloud cover (white within the glacier mask), 15. Aug 2010.

Table 4.1: Comparison of the classified snow pixels area ratio (SAR), mean snow line altitude (SLA) and standard deviation of snow line altitudes from MODIS and Landsat satellite data for 15 Aug 2010.

Landsat				
SAR		0.62		
SLA (m a.s.l.)		5774		
MODIS				
Albedo threshold	37%	38%	39%	Std Dev (m)
SAR	0.64	0.62	0.60	
SLA 20th percentile (m a.s.l.)	5808	5810	5816	4.16
SLA 14th percentile (m a.s.l.)	5778	5783	5788	5.00
SLA 13th percentile (m a.s.l.)	5773	5776	5783	5.13
SLA 12th percentile (m a.s.l.)	5762	5768	5775	6.50
SLA 10th percentile (m a.s.l.)	5748	5753	5758	5.00
Std Dev (m a.s.l.)	22.32	21.08	21.20	

4.3.2 Transient snow line

We only analysed scenes where more than 45% of pixels within the glacier mask were valid. Validity concerns both, land- and snow classified pixels.

The 20th percentile of the snow covered glacier elevation was successfully used by Shea et al. (2013) to approximate the spatially averaged snow line altitude. Hence we calculated a fixed percentile of the snow classified pixels elevation for each scene. For this approach it was necessary to differentiate between ice and snow on the surface, because the MODIS snow product includes snow and ice surfaces within the snow classification. Using the albedo information embedded in the MOD10A1 and MYD10A1 products, we apply a threshold to distinguish between snow and ice. Apart from dirty snow the minimum albedo of snow is considered to range around 35 to 40% (Hall and Martinec 1985; Paterson and Cuffey 1994).

To adjust the locally precise percentile and albedo threshold we exemplary compared the resulting MODIS snow albedo values with high resolution Landsat imagery. For the study region only one cloud free Landsat image (TM, 15.08.2010 12.30 local time, path: 140, row: 36) could be used for comparison within the observation period since the snow line had to be clearly visible and the date needed to be compatible with a MODIS scene containing enough valid pixels. The Landsat scene with a resolution of 30 m provides a mapped snow line with a negligible error considering the MODIS calculation basis of 500 m spatial resolution. Besides a visible comparison a quantitative calculation of the number of snow pixels within the Landsat and the MODIS image was carried out (Table 4.1). For that the MODIS pixels within the shape file of the digitized snow line were compared to the MODIS derived snow covered area. The snow pixels area ratio has been calculated and is used for a better comparison of the snow classified pixels. The number of MODIS snow pixels approach the number of Landsat snow pixels when applying an albedo threshold of 38%. The visual comparison can be seen in Fig. 4.7. Furthermore the mean altitude of the digitized Landsat snow line was compared to the corresponding daily MODIS snow line. The best fit at Purogangri was hence found for a 38% albedo threshold and the altitude of the 13th percentile (Table 4.1).

To incorporate the initial 20th percentile for snow line derivation in Shea et al. (2013) we correlated resulting ELAs based on different parameter sets. Highly significant correlations of the resulting interannual ELAs variability confirm that the varying of the parameters does affect the absolute altitude of the ELA but not so much its interannual variability.

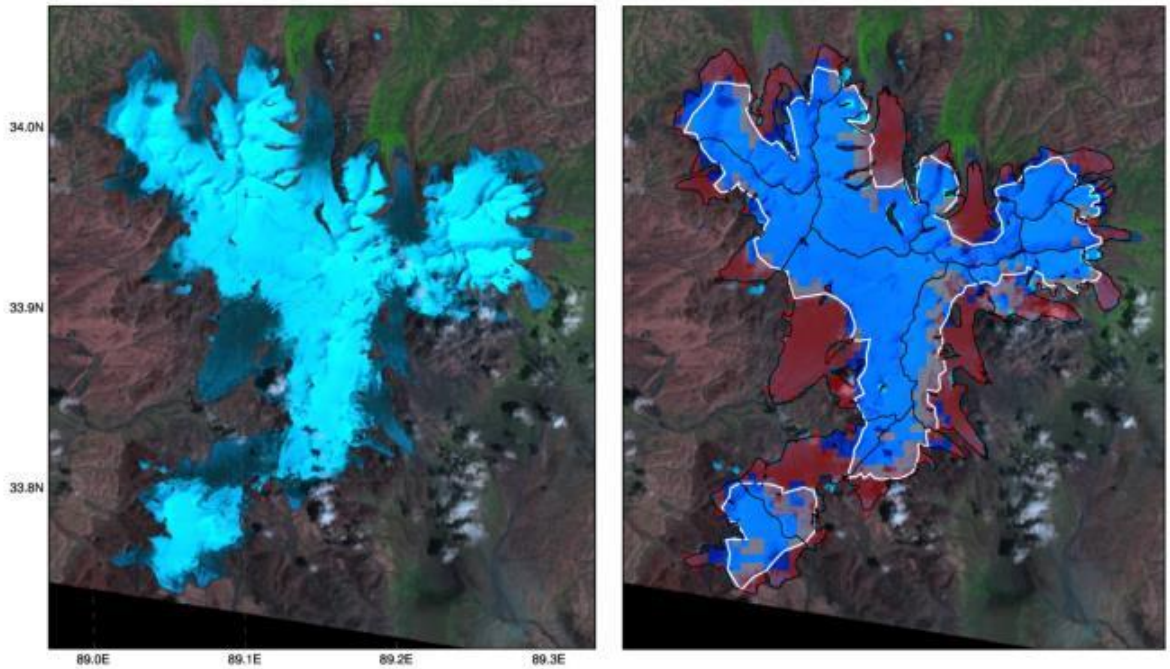

Fig. 4.7: Landsat TM image original (left), MODIS snow (dark grey) or ice (light grey) pixels (right) after application of the 38% albedo threshold; digitized snow line from Landsat image (white) and glacier mask (black), 15. Aug 2010.

4.3.3 Equilibrium-line altitude

To calculate the ELA proxy we focused on the end of the ablation season when the snow line approaches its highest elevation in the annual cycle. The considered period in this respect is 01 July to 30 September of each year, which equals 92 days.

For each of these days the mean transient snow line altitude across Purogangri was calculated if more than 45% valid pixels were located inside the glacier mask (Fig. 4.8). The maximum snow line altitude within this 92-days period is assumed equal to the ELA. To account for a possible outlier this value was fitted by taking the second maxima as the ELA proxy (cf. Fig. 4.9 and Fig. 4.8). This approach is slightly different than the method described in Shea et al. (2013) who used the maxima from a loess-smoothed time-series of transient snow line elevations.

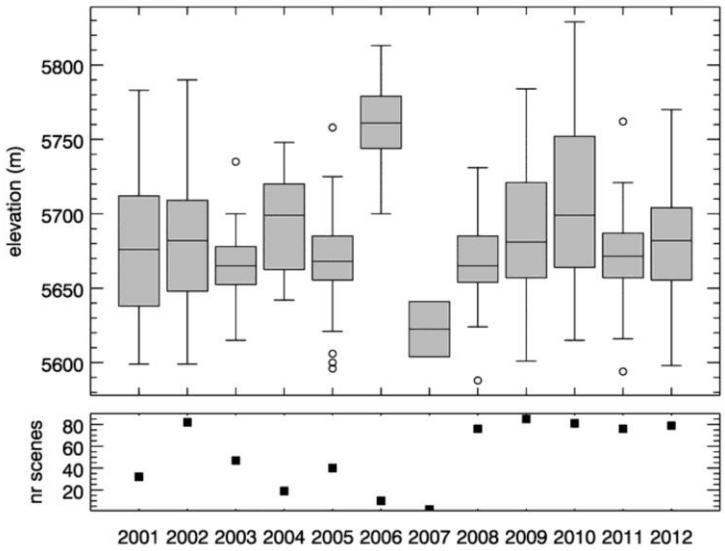

Fig. 4.8: Yearly boxplot of the daily transient snow line from 1. July to 30. September, showing the median, encloses the 75th and 25th quartiles and extends to the minimum and maximum (error bars) (top). Numbers of scenes with more than 45% valid data (bottom).

4.3.1 Correlations

A linear correlation analysis was performed in order to relate the interannual variability of the annual ELA to the underlying climate forcing represented by various predictors as introduced in the data section. The data independence was confirmed beforehand by conducting autocorrelation analysis of the ELA time series. Linear Pearson correlation coefficients are tested for significance using p-values.

4.3.2 Assessment of uncertainty

Since band 6 on Aqua satellite failed shortly after launch, the NDSI is calculated with the ratio of band 7/band 4 instead of band 6/band 4. Therefore, we checked performance of ELA calculation based on NDSI from both satellite individually. The interannual variability which is the scope of this study is not influenced by different calculation of the NDSI for the two satellites.

The validation of the parameter set of albedo threshold and the number of the percentile is considered reliable concerning the interannual variability of the ELA. Varying the two parameters (albedo threshold and percentile of snow covered pixels) within a reasonable range (35 to 41% albedo, 10^{th} to 20^{th} percentile) to derive the snow line altitude does not change the resulting interannual ELA variability which is the main focus of this study.

The validation is not satisfactory regarding the absolute altitude of the snow line for all scenes even though the approximation with one Landsat scene returns reasonable agreement. It can be assumed that no change in snow cover has occurred in roughly two hours, between the acquisition times of

the Landsat image and the MODIS scenes. The methodology requires that the glacierized region is sufficiently large to balance the coarse spatial resolution of the satellite data. If no superimposed ice or firn is present the end-of-summer snow line altitude and the annual ELA are equal. If superimposed ice or firn is present and if the induced altitude difference cannot be neglected, despite the coarse spatial resolution, the impact on the interannual variability is still minor. Hence we anticipate that the effect of superimposed ice and firn on the interannual ELA variability is small.

An additional source of error may be a reduced summer snow line due to frequent summer snow falls. However this cannot be quantified in more detail due to the lack of ground truth data from the study site.

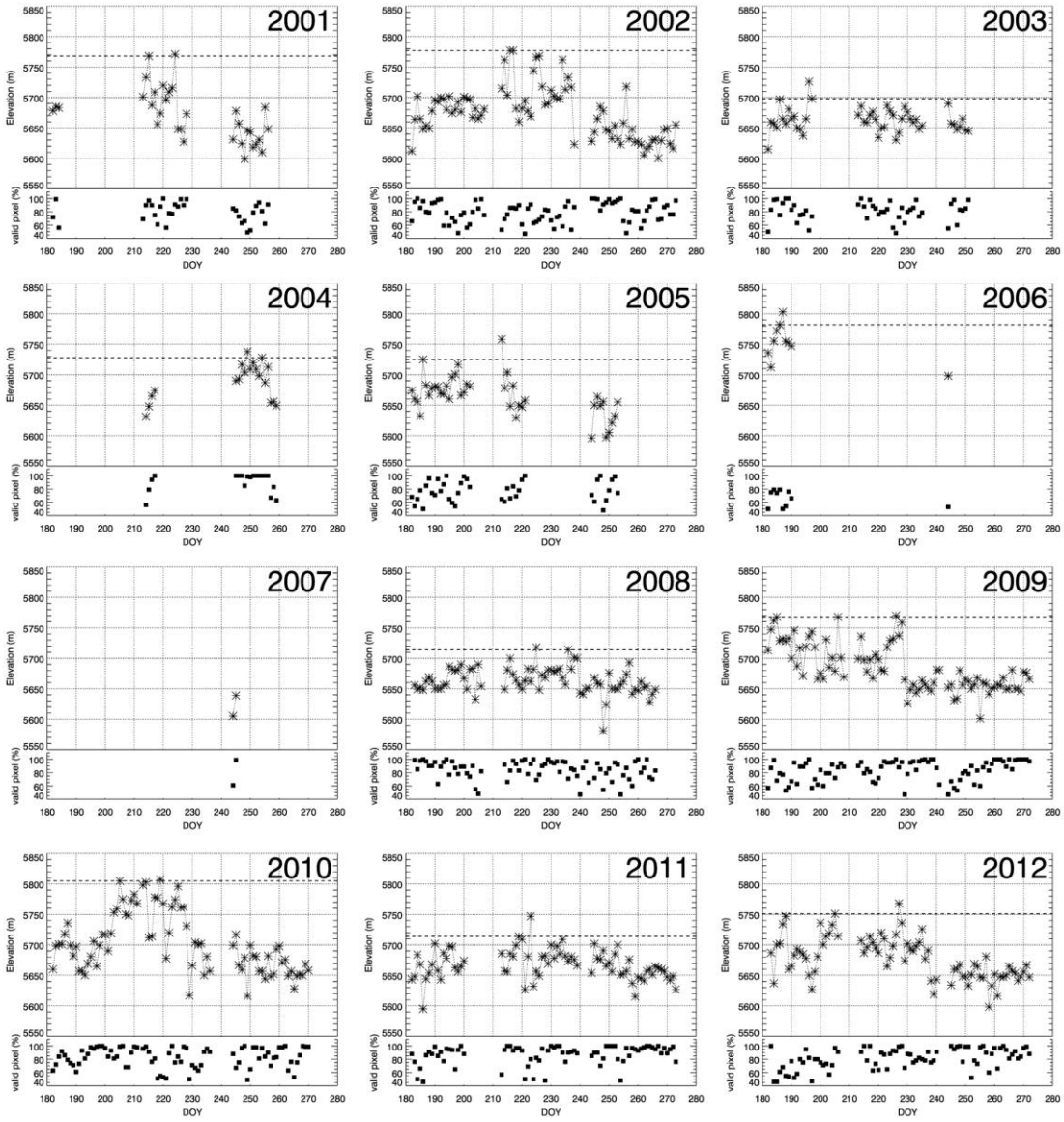

Fig. 4.9: Daily transient snow line altitude (top) and percentage of valid pixels (bottom), second maximum as ELA proxy (dotted line) as derived in chapter 4. This figure is not included in Spieß et al. (2015, Geografiska Annaler: Series A).

4.4 Results

The results include the average annual snow line at Purogangri, the annual ELA proxy as well as its interannual variability. Correlation coefficients indicate the relation between the latter and other climate related variables.

The average snow line altitude at Purogangri is at its highest position in summer. Also in winter the snow line altitude rises to its second maximum in December (Fig. 4.3b). Accordingly the average monthly albedo of the MODIS snow classified pixels within the glacier mask shows an increase in spring with the increasing snowfall. It declines in the summer months at times of strongest melt (Fig. 4.3b). The annual cycle of albedo reveals a secondary minimum in February. We interpret this as an effect of snow drift. The hypnosis is that the albedo decreases when older snow is exposed subsequently to snow drift events.

Displayed in Fig. 4.4b is the interannual variability of the ELA. The error bars display uncertainty including albedo threshold of 35 and 41% with respective application of the 10^{th} and 16^{th} percentile. In order to provide a realistic assessment of the respective ELA the number of scenes included into the calculation was additionally documented (Fig. 4.4b, middle). The year 2007 does not allow the calculation of the ELA proxy because the minimum of three days holding valid albedo data in the observation period is not reached (Fig. 4.8 and Fig. 4.4b). The year 2006 is questionable because it is based on only 10 scenes in the observation period. Overall uncertainties relate to the albedo threshold and percentile used to approximate the ELA are ± 44 m (Fig. 4.4b).

Spatial variability of the ELA on different glaciers across the ice cap is existent. But the scope of this study is an average annual ELA of the whole ice cap. Therefore, we have not addressed this kind of error in more detail. The mean ELA in the years 2001 to 2012 was calculated to 5748±37 m a.s.l. (mean ± one standard deviation). The lowest position of the ELA is at 5698 m a.s.l. in 2003 and the highest position at 5805 m a.s.l. in 2010. An overall slightly increasing trend in the ELA from 2003 to 2012 can be deduced, even though the time series is too short to perform a secured trend analysis.

The results of the linear correlation analysis between the ELA and the predictors show high correlations in the months June to August (Table 4.2). Since seasonally aggregated predictors did not result in stronger correlations we interpret the correlation of monthly values. The correlations consider conditions during the glaciological year. Values from October, November and December are examined for their influence on the following year's ELA. The physical connection of the predictors to the development of the ELA in July to September is most apparent in these months. A negative (positive) correlation with an increase of the predictor leads to a lower (higher) ELA.

In June an enhanced zonal wind speed above ground shows a significant positive correlation with the ELA (r=0.74). The precipitation in June is showing a negative correlation (r=-0.54) with the ELA. In July the temperature and the meridional wind component at 10 m above ground are significantly positively correlated with the ELA (r=0.63, 0.92). In August a negative correlation between the ELA and the zonal wind above ground and at the 400 hPa level is apparent (r=-0.81, -0.65). The total wind speed shows a distinctly positive correlation above ground (r =0.78) and a slightly negative correlation at the 300 hPa level (r =-0.48) with the ELA in August. Whilst the ISM shows no significant correlation with the ELA at all, the NAO correlates negatively in February and September (r=-0.64, -0.50) and positively in November (r=0.54).

Table 4.2: Pearson Correlation coefficient (r) for correlation between the interannual ELA and climatic predictors as well as between interannual ELA and atmospheric climate indices; ELA calculated based on scenes ≥ 45% valid pixels with an snow albedo threshold of 38% using the 13th percentile between July to September; significant correlations above the 0.05 level of significance are indicated, p<0.1(bold), p<0.05(bold, italic), p<0.01(bold, underlined).

Predictors	Jan	Feb	Mar	Apr	May	Jun	Jul	Aug	Sep	Oct	Nov	Dec
temperature (°C, 2 m)	0	0.51	0.07	0.16	0.14	0.36	**0.63**	0.04	0.11	0.31	0.51	0.01
precipitation (mm h-1)	-0.4	0.12	-0.18	-0.19	-0.2	-0.54	-0.12	0.18	-0.07	0.49	-0.05	0.29
water vapour mixing ratio (g kg-1)	-0.09	0.13	-0.05	-0	-0.2	-0.19	0.48	0.13	0.21	0.51	0.29	0.37
u-wind (m s-1, 300 hPa level)	0.24	0.29	0.1	0.39	0.41	0.29	-0.49	-0.46	-0.35	0.37	0.48	0.05
u-wind (m s-1, 400 hPa level)	0.08	0.42	0.28	0.28	**0.61**	***0.68***	-0.44	***-0.65***	-0.46	0.49	**0.63**	0.29
u-wind (m s-1, 10 m)	-0.2	0.5	0.45	0.18	0.54	***0.74***	-0.23	**-0.81**	0.13	0.44	***0.77***	0.27
v-wind (m s-1, 300 hPa level)	-0.1	0.32	-0.23	-0.54	-0.23	0.44	0.53	-0.35	0.11	0.22	-0.12	-0.13
v-wind (m s-1, 10 m)	-0.32	0.27	0.08	-0.32	-0.25	0.48	**0.92**	-0.23	0.11	0.57	0.19	0.02
wind speed (m s-1, 300 hPa level)	0.22	0.29	0.11	0.38	0.39	0.36	-0.38	-0.48	-0.25	0.37	0.5	0.03
wind speed (m s-1, 10 m)	-0.23	0.51	0.14	-0.27	-0.17	-0.5	0.15	**0.78**	-0.46	0.07	***0.76***	0.33
NAO (Hurrell PC)	-0.21	**-0.64**	-0.3	-0.03	0.09	0.13	0.14	-0.03	-0.5	0.39	0.54	-0.12
ISM	-	-	-	-	-	-0.12	-0.4	0.07	-0.35	-	-	-

4.5 Discussion

The interannual variability of the ELA is in overall agreement with the sparse existing results on mass balance (Mölg et al. 2014; Neckel et al. 2013) at Purogangri. Using the ELA as a mass balance proxy a higher (lower) ELA hints towards a more negative (positive) or less positive (negative) mass balance. The interannual variation of the mean precipitation in June and temperature in July are shown in Fig. 4.4a. As the main climatic variables directly affecting the snow cover and glacier mass balance they match the ELA variability. Here 2006, 2009 and 2010 are revealed as comparatively drier years with above average temperature resulting in a higher ELA. The years 2003, 2004, 2008 and 2011 show above average precipitation in June (Fig. 4.4a). Except for 2004 this leads to a lower ELA.

The agreement with the mass balance of the Zhadang glacier in the Nyainqêntanglha range in Mölg et al. (2014) is apparent within the years with strongly negative mass balance results (Fig. 4.4b bottom). The most negative mass balance in 2006 at Zhadang glacier coincidences with a high ELA at Purogangri. The same applies for 2009, when a decreased negative mass balance at Zhadang glacier and a higher ELA at Purogangri coincident with an especially late monsoon onset (Kang et al. 2009; Mölg et al. 2014). In 2008, the monsoon onset is earlier then in subsequent years, the mass balance is less negative at Zhadang glacier and the ELA at Purogangri is at a higher position. Both regions belong to the summer accumulation regime and are influenced by the monsoon system (Maussion et al. 2014a). However the correlation with the annual monsoon onset suggests no connection to the ELA of Purogangri.

Concerning the glacierized area of Purogangri ice cap Lei et al. (2012) conclude a decrease of 2.4% of the western part of the glaciers within the Linggo Co catchment between 1974 and 2007 from analysis of Landsat Imagery.

Neckel et al. (2013) estimated the geodetic mass balance of Purogangri ice cap in 2000-2012. They conclude the zero elevation change for Purogangri ice cap at an elevation of 5750 m a.s.l., which is only two meters above the average ELA proxy in this study. No clear trend towards a higher ELA and of a mean loss of glacier mass is distinct according to our results. This does not include trends of single glaciers. Accordingly, Neckel et al. (2013) show surface lowering of the outlet glaciers and thickening of the interior part of the ice cap, while the mass budget between 2000 and 2012 remains close to equilibrium. This pattern of surface elevation changes across ice caps has also been observed in other parts of the world (e.g. Möller and Schneider 2010). Yi et al. (2002) state that the modern snow line at Purogangri can be found between 5620 and 5860 m a.s.l., which matches the average snow line between 2001 and 2012 ranging from 5630 to 5700 m a.s.l. according to our study (Fig. 4.4b).

By conducting a linear correlation analysis we expect significant correlations whenever strong causal physical links are present. It has to be kept in mind that correlation does not imply causation. Nevertheless high and significant correlations may well indicate climate related forcing of the glacier mass balance.

June precipitation has been identified as a crucial factor for the mass balance on Zhadang glacier in a previous study by Mölg et al. (2012). Summer precipitation in June mainly falls as snow, and because it is still cold, with less than 20 days showing more than 3 hours above melting point in this year, it is adding to the accumulation and prevents melting at the glacier due to the positive albedo feedback of fresh snow. The expected negative correlation coefficient (r=-0.54) between the precipitation in June and the ELA, however, is not significant.

The 300 hPa level equals roughly the height of the jet stream (Barnes et al. 2010) whereas convective clouds reach up to the 400 hPa level. No direct correlation between the manifestation of the jet stream and the ELA at Purogangri is apparent. The significant correlation (r=0.68) between the zonal wind component at the 400 hPa level and the ELA in June indicates a reduction of the precipitation due to a stronger west wind. The precipitation negatively correlates with the west wind (r=-0.54), as shown in Table 4.3, where correlations between different climatic predictors are illustrated. In June, the Tibetan low starts to form and convective precipitation is prevailing. At Purogangri ice cap, where the main precipitation falls in summer, the part of convective precipitation accounts for about 70% of the total precipitation (Maussion et al. 2014a). An enhanced wind speed might suppress deep convection which reduces precipitation.

An increased, comparatively drier, westerly wind in June above ground might intensify turbulence and enhance sublimation (r=0.74). For example, as found in a study at Kilimanjaro by Mölg et al. (2009) and in the Everest region by Wagnon et al. (2013), regarding the overall glacier mass balance, the sublimation can be the dominant factor that accounts for even more of the mass loss than the melt. The Kilimanjaro glaciers are of the summer accumulation type as it is the case of the subtropical Purogangri ice cap. The manifestation of the sublimation should apply even more in drier environments like Purogangri.

In July, the month with highest average temperature, surface melt is the main driver for the evolution of the transient snow line, and thus for the ELA at the end of the ablation season (Fig. 4.3a). Higher temperatures lead to more melt and a higher ELA (r=0.63). In July the temperature is highly correlated with the meridional wind component at 10 m above ground with (r=0.60; Table 4). This implicates that the temperature is controlled by southerly air flow connected to the atmospheric

conditions of the Tibetan low pressure system. Furthermore, it explains the highly significant correlation between the meridional wind and the ELA in July (r=0.92).

In August the westerly winds are at their minimum speed while precipitation is at its annual maximum (Fig. 4.3a). Increased southerly wind speeds above ground leads to higher air temperatures (r=0.77; Table 4), to enhanced precipitation (r=0.63; Table 4) and thus to a higher ELA (r=0.78). Increased westerly winds, however, might block the transportation of heat from south-east and therefore cause a lowering of the ELA (r=-0.81). However, no correlation between air temperature and ELA is apparent in August to explain this connection. Neither a strong relation of the ELA to the air temperature nor to the precipitation is found for the month of August.

The overall wind speed in August at 10 m above ground shows a significant correlation with the ELA (r=0.78). Solely in August the wind speed above ground is negatively correlated with the zonal component of the wind (r=-0.83). Therefore easterly flow is dominating the wind speed at 10 m above ground in August. The positive correlation between wind speed and ELA suggests a process of easterly flow introducing melt energy in August which is in line with arguments given in Maussion et al. (2014a). In contrary to the situation in July the meridional wind component in August does not show significant correlation with the ELA which additionally indicates a shift of temperature and water-vapour source from south to east.

In November, highly significant correlations between wind speed and the zonal component of the wind above ground are identifiable (r=0.76 and r=0.77) whilst the wind speed is dominated by the westerlies (r=0.93; Table 4) and is generally high (Fig. 4.3a). Even though the spatial effect of snow drift on the snow distribution can be very small-scaled this might be an indication that higher wind speed above ground in November induces snow drift. In connection with katabatic wind systems snow drift may affect lower parts of the glaciers and increase the ELA when accumulated snow is redistributed to peripheral zones. The effect may lead to a more negative mass balance of the glacier (Sauter et al. 2013). Additionally this process enhances winter time sublimation adding to the mass loss. Snow drift and sublimation might also be accountable for the reduced albedo on the ice cap in winter (Fig. 4.3b).

The consideration of the teleconnection indices NAO and ISM in the correlation analysis provides a starting point in the study of global connection of the atmospheric circulation to glacier mass balance variability at Purogangri. Surprisingly neither NAO nor ISM shows significant correlation with the ELA in June to September.

The ISM Index describes strong monsoon circulation whenever the easterly wind speed in North India is distinctly higher than in the south of the Arabian Sea (Wang et al. 2001). Assuming that a stronger monsoon leads to enhanced water vapour transport onto the Tibetan Plateau it might eventually increase precipitation and result in a lower ELA. However, no significant negative correlation in June and July was obtained. During the monsoon core season the ELA at Purogangri does not seem to be significantly related to the large-scale variability of the monsoon as also previously described in Mölg et al. (2012) for the Nyainqêntanglha Range, southeast of Purogangri ice cap.

In the positive phase of the NAO the pressure differences between 20°N and 80°N are larger. This leads to a more zonal jet stream, a smaller number of frontal systems, higher wind speeds and a northward shift of the jet stream (Barnes et al. 2010). The NAO in February shows a connection to the ELA at Purogangri (r=-0.64). A correlation between the NAO and the temperature is significant in February (r=-0.69; Table 4.3). In February, a positive phase of the NAO seems to be connected to

lower temperatures at Purogangri, the temperature in turn is positively correlated with the ELA (r=0.51). It seems that the temperature variability in February controls sublimation and possibly also melt due to intensive solar radiation, even when the mean daily temperatures are far below melting point. According to Mölg et al. (2012) the sublimation peaks in the month prior to the monsoon onset at Zhadang glacier. In the continental region of Purogangri ice cap, with even drier conditions in winter, the sublimation seems to play an even more dominant role in mass loss of a glacier.

Table 4.3: Pearson Correlation coefficient (r) for monthly correlation between interannual climatic predictors and atmospheric climate indices; correlations above the 0.05 level of significance are indicated, p<0.1(bold), p<0.05(bold, italic), p<0.01(bold, underlined).

	Jan	Feb	Mar	Apr	May	Jun	Jul	Aug	Sep	Oct	Nov	Dec
u-wind(10m)/ precipitation	0.20	0.19	-0.17	0.01	-0.17	**-0.52**	-0.26	-0.10	***-0.58***	-0.40	-0.12	-0.48
u-wind(400hPa)/ precipitation	-0.15	0.26	-0.21	0.24	-0.30	**-0.54**	0.09	-0.33	-0.10	-0.22	0.05	-0.36
u-wind(300hPa)/ precipitation	-0.32	-0.11	-0.47	0.25	***-0.63***	-0.40	0.36	-0.42	-0.26	-0.11	0.14	-0.39
v-wind(10m)/ precipitation	0.34	0.41	-0.31	0.45	0.28	-0.21	-0.01	***0.63***	0.56	0.21	-0.12	-0.08
v-wind(400hPa)/ precipitation	0.29	0.14	-0.36	0.27	0.38	-0.53	-0.30	0.21	0.02	-0.24	-0.09	-0.08
water vapour mixing ratio / precipitation	0.28	0.35	0.52	0.50	0.36	**0.77**	***0.62***	***0.60***	**0.86**	**0.86**	0.43	0.45
wind speed(300hPa)/ u-wind(300hPa)	**1.00**	**1.00**	**1.00**	**1.00**	**0.93**	**0.97**	**0.99**	**1.00**	**0.92**	**1.00**	**1.00**	**1.00**
wind speed(300hPa)/ v-wind(300hPa)	0.11	0.23	-0.34	0.04	-0.14	0.44	0.32	***0.61***	0.52	**0.71**	0.08	0.06
wind speed(10m)/ u-wind(10m)	**0.98**	**0.98**	***0.68***	**0.71**	0.12	-0.45	-0.20	**-0.83**	0.27	**0.85**	**0.93**	**0.97**
wind speed(10m)/ v-wind(10m)	***0.68***	0.23	0.02	0.00	0.32	-0.45	0.05	-0.10	***-0.58***	0.41	0.54	0.48
u-wind(300hPa)/ u-wind(10m)	***0.69***	***0.68***	***0.66***	**0.77**	0.35	***0.69***	0.50	0.55	0.35	**0.84**	**0.79**	***0.68***
v-wind(300hPa)/ v-wind(10m)	**0.73**	**0.91**	***0.66***	**0.81**	***0.70***	**0.80**	0.56	0.05	**0.72**	0.54	***0.70***	**0.77**
wind speed(10m)/ temperature	0.52	0.26	0.37	0.24	0.42	-0.55	-0.12	0.28	0.36	0.24	0.18	-0.31
u-wind(10m)/ temperature	0.51	0.23	-0.11	0.34	-0.08	***0.66***	0.23	-0.01	0.05	0.22	0.19	-0.24
v-wind(10m)/ temperature	0.21	-0.42	-0.51	-0.19	0.40	***0.62***	***0.60***	**0.77**	-0.14	0.55	-0.14	-0.15
u-wind(400hPa/ temperature	0.37	-0.23	-0.44	0.14	-0.35	***0.68***	-0.10	-0.39	-0.55	0.34	0.32	-0.02
v-wind(400hPa)/ temperature	-0.29	-0.37	-0.33	-0.34	-0.08	***0.64***	***0.65***	0.49	-0.37	0.52	-0.49	0.14
NAO/temperature	-0.11	***-0.69***	-0.25	-0.22	-0.26	-0.08	-0.11	-0.44	0.33	0.36	0.08	0.36
NAO/u-wind(10m)	0.13	-0.24	0.24	-0.31	0.18	-0.12	***-0.66***	0.03	0.31	0.35	0.43	0.38
NAO/ precipitation	-0.22	-0.21	-0.25	-0.51	0.32	0.09	-0.34	-0.53	-0.05	-0.12	-0.57	-0.15

4.6 Conclusion

This paper presents a remote-sensing approach to derive snow lines from MODIS satellite data to estimate mass balance variability of glaciers on the Tibetan Plateau by means of the annual ELA. The approach can be readily applied to construct time series of transient snow line altitudes with daily resolution and regional annual ELAs on larger glacierized areas starting with the availability of MODIS satellite data in 2001.

The resulting mean ELA between 2001 and 2012 at Purogangri ice cap on the central Tibetan Plateau lies at 5748 m a.s.l. with a mean interannual variability of 37 m (cf. Fig. 4.2). The lowest position of the ELA is in 2003 and the highest position in 2010. The ELA does not show any clear trend in the study period. The average snow line altitude and the average albedo on the ice cap indicate winter mass loss due to snow drift and sublimation. This presumption is reinforced by a positive correlation between zonal wind above ground in November and February and ELA.

Apparent are the significant correlations of the zonal wind component above ground and at the 400 hPa level with the ELA. This significant correlation is changing sign between June and August, which indicates changed atmospheric conditions driving snow and ice melt. In winter westerlies dominate on the Plateau. There are stable conditions prevailing during this period. Precipitation is mainly driven by orography. In June, the Tibetan low pressure system starts to form on the Plateau. Convective precipitation leads to more snowfall and a lowering of the ELA. In June, a stronger zonal wind might lead to the suppression of the convection, less snow fall and finally to a higher ELA.

In the core of the monsoon season in July and August, the atmospheric conditions are distinctly different. The Tibetan low is established in July. Higher temperatures in July increase the percentage of liquid precipitation, which together with snow melt increases the ELA. In the core part of the monsoon season southerly to easterly flow above ground is influencing the ELA at Purogangri. For August we hypothesize that higher wind speed above ground promotes higher temperature due to inflow of air from southerly and easterly directions, even though no connection is apparent between ELA and temperature. Furthermore, sublimation may be enhanced contributing to glacier mass loss in summer. Interestingly, there seems to be a stable connection between the phase of the NAO in February and the ELA at Purogangri between 2001 and 2012.

To improve the results in future studies the introduced method will be adapted to MODIS data with a higher spatial resolution of 250 m. It will be promising to study the influence of the temporally and spatially different source regions of air temperature and air humidity on the Tibetan Plateau by applying the method to other glacierized regions as well. This will enable to test the hypothesis that global circulation is accountable for atmospheric stability and glacier mass balance on the Plateau. In this study only weak correlations were found between quantities relating to the Indian monsoon and the ELA. The result indicates that moisture might be rather recycled on the Plateau itself instead of originating from substantial inflow to Purogangri region from the south. More precise correlation analysis is necessary to exclude spurious correlation and reveal partial correlations. By applying the remote sensing approach to different regions across the plateau it may be possible to study different influences of atmospheric drivers of ELA variability depending on the location of glaciers on the Tibetan Plateau.

5 MODIS derived inter-annual variability of the equilibrium-line altitude across the Tibetan Plateau

Using the Moderate-resolution Imaging Spectroradiometer (MODIS) Level 1 radiance Swath Data (MOD02QKM) with a spatial resolution of 250 m, we derive snow lines during the months of July to September in 2001 to 2012 for several mountain ranges distributed across the Tibetan Plateau (TP). Radiance bands 1 and 2 are projected to the study area and processed automatically. The discrimination between snow and ice is done using a k-mean cluster analysis and the snow lines are delineated based on a fixed percentile of the snow cover altitude. The highest transient snow line altitude is then taken as a proxy for the equilibrium-line altitude (ELA). In the absence of measured glaciological, meteorological or hydrological data, our ELA time series enable a better understanding of atmosphere-cryosphere couplings on the TP. Inter-annual ELA variability is linked to local and remote climate indices using a correlation analysis. Southerly flow and higher temperatures are linked with a higher ELA in most regions. Eastern and Trans-Himalayan sites show positive correlations between winter temperatures and ELA. As winter temperatures are substantially below zero, this suggests an enhancement of winter sublimation as opposed to a reduction in accumulation. It appears that large-scale atmospheric forcing has varying and sometimes opposite influences on the annual ELA in different regions on the TP.

5.1 Introduction

The variability of the annual equilibrium-line altitude (ELA) is a valuable proxy for the variability of glacier mass balance (e.g. Zhang et al. 1998; Shea et al. 2013; Brun et al. 2015). In the absence of other measured glaciological, meteorological or hydrological data, the ELA could also be used to validate glaciological model results. The main objective of this study is to use remote sensing approaches in order to compute the ELA for eight glacierized mountain ranges across the Tibetan Plateau (TP). These ELAs are then used to reveal differences in glacier response to the various climatic forcings on the TP, where only few and spatially dispersed mass balance studies have been conducted to date.

The selected regions of interest (ROIs) are distributed heterogeneously across the TP, spanning an east to west transect (Fig. 5.1). The eight study sites are: the Purogangri Ice Cap on the central TP, two regions in the Western Nyainqêntanglha range, the Targo Gangri, Shankangsham and Surla range

in the south-central TP, the Gurla Mandhata massif in the south-west and the Muztagh Ata in the west of the TP (Fig. 5.1).

The area of the TP covers different climate regions with distinct influences on glaciers. In simplified terms: (i) the precipitation and temperature decreases from the south-east to the central western plateau, (ii) the accumulation regime changes from summer-accumulation type in the east to winter-accumulation type in the west, and (iii) the glacier types change from temperate in the south-east to polythermal and cold glaciers in the continental west (Shi and Liu 2000; Rupper and Roe 2008; Maussion et al. 2014a). All lakes fed from glaciers in the ROIs show increased water levels between 2003 and 2009, which seems to be induced by increased precipitation rates as well as by glacier meltwater (Zhang et al. 2011; Wu et al. 2014). Wu et al. (2014) found that glacier melt contributed 21% of the recent increase in the volume of Nam Co lake. Except for the south-eastern slope of the Nyainqêntanglha range, none of the ROIs have an outflow to the sea (e.g. Neckel et al. 2014).

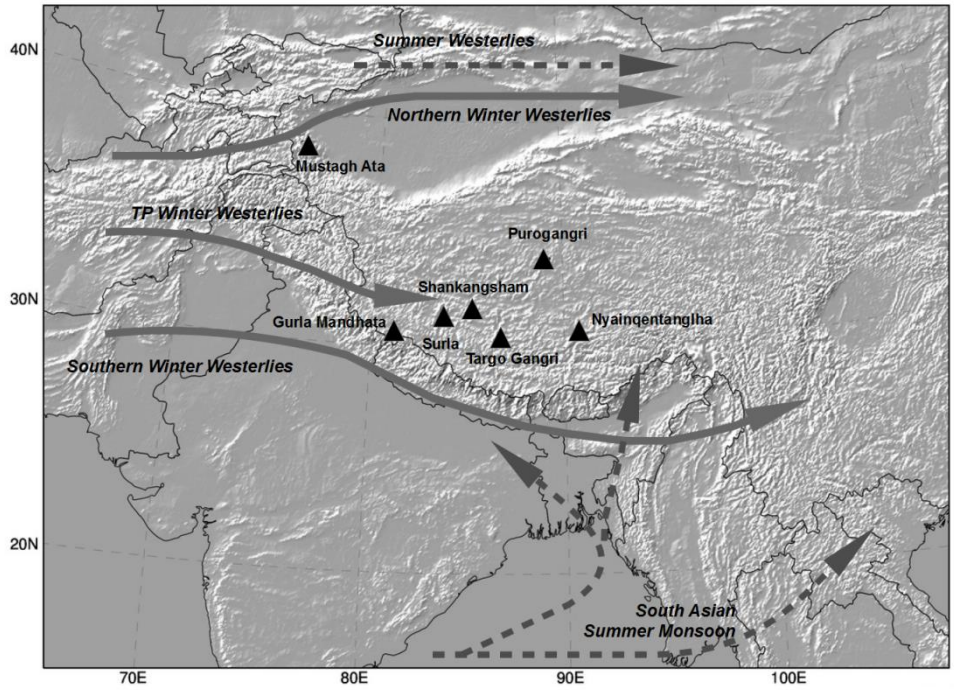

Fig. 5.1: The Tibetan Plateau (TP). Study areas (ROI) are indicated as triangles; SEN and NWN in the Western Nyainqêntanglha together are represented as one triangle; arrows indicate the basic atmospheric circulation, based on Bolch et al. (2012) and Yao et al. (2012).

5.2 Study sites

The Purogangri Ice Cap (PIC) is Tibet`s largest ice cap in the semi-arid central Plateau (Fig. 5.2; Table 5.1). Its glaciers have a spring and summer accumulation regime. The region receives about 70% of its precipitation between May and September (Fig. 5.3) and is influenced by strong westerly winds during winter (Maussion et al. 2014a). Neckel et al. (2013) found the recent PIC geodetic mass budget to be close to equilibrium, with a mass balance of −44±15mm w.e. a^{-1} between 2000 and 2012.

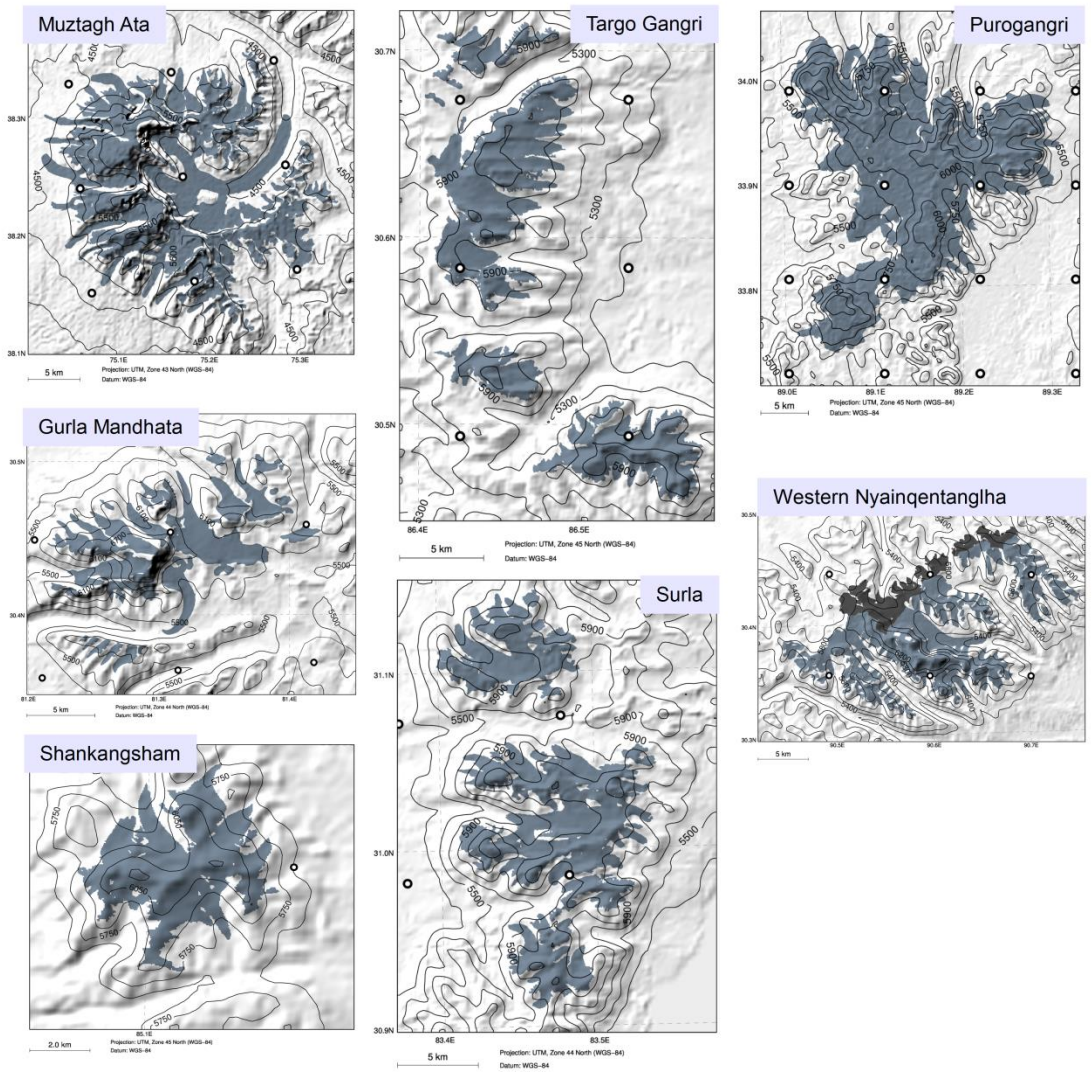

Fig. 5.2: Topographic maps of all ROIs, with glacier masks in grey, SEN and NWN are combined into one plot with NWN in a darker grey, elevations are given in m a.s.l. HAR grid points as circles.

The Western Nyainqêntanglha range is located in the southern central TP at the transition zone between temperate and subcontinental glaciers (Bolch et al. 2010; Fig. 5.2; Table 5.1). It is influenced by westerlies in winter but has a distinct summer accumulation regime in connection with the Indian monsoon. More than 90% of annual precipitation falls between May and September (Fig. 5.3). We differentiate two ROIs in the Western Nyainqêntanglha range to take into account distinctly different synoptic climatology on the two sides of the hydrological divide: a north-west oriented slope (NWN) and a south-east oriented slope (SEN; Fig. 5.2). The glaciers in the NWN drain into the lake Nam Co. The glaciers on the south-eastern slope drain eventually to the Tsangpo-Brahmaputra River. The ice cover in SEN reaches higher than on NWN (cf. Table 5.1) but both slopes showed similar glacier change rates (Bolch et al. 2010). Total glacier area decreased by −9.9±3.1% between 1976 and 2009 and no glacier was found to be advancing. Mean glacier surface elevation changes of -8.39 m from ICESat and SRTM data were found between 2003 and 2009 in the Western Nyainqêntanglha range (Wu et al. 2014). Zhao et al. (2014b) studied the Gurenhekou glacier as representative of the southern slope of the Nyainqêntanglha range, and found an average retreat rate of 8.3 m a^{-1}. Mölg et al. (2014) calculated the mass balance from 2001 to 2011 of the Zhadang glacier in the Western

Nyainqêntanglha range using a physically based model. They detected mid latitude climate as a possible driver of glacier mass balance variability in this region.

Extending the transect to the west, we chose to add three ROIs in the central Trans-Himalaya. These glaciers belong to the subcontinental and the extreme continental type. The mountain range, south of the lake Tangra Yumco, is called Targo Gangri in the following, as mentioned by Hedin (1909) (Fig. 5.2; Table 5.1). Further we chose the southernmost part of the Shankangsham range (Fig. 5.2; Table 5.1) which is mentioned by Town (2008). Its glaciers drain into the Dawa Lake to their south. Glaciers in the Surla range (Styron et al. 2013) drain into the Rinchen Tshubsu in the north and, to a lesser extent, into the Palung Co in the south-east (Fig. 5.2; Table 5.2). The glaciers in all three ROIs belong to a pronounced summer-accumulation regime type, receiving up to 70% of its annual precipitation in June to August (Fig. 5.3). Absolute values of annual precipitation within the HAR dataset must be cautiously interpreted (Huintjes 2014). They range well below 500 mm for all three ROIs.

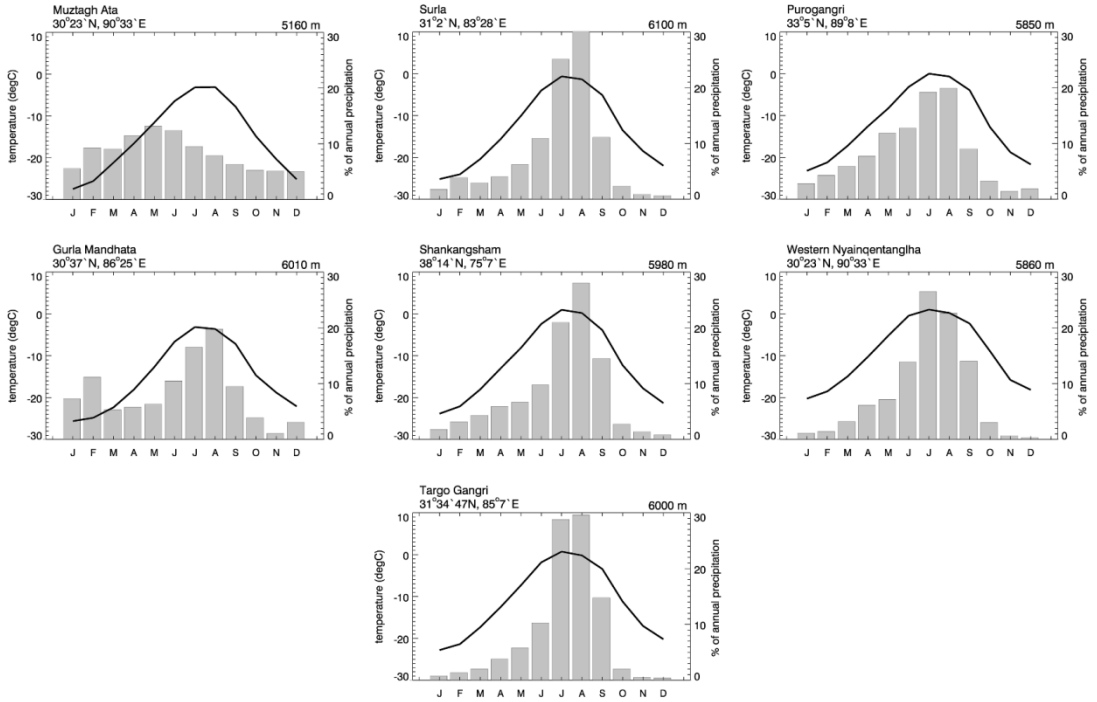

Fig. 5.3: Average annual cycle of temperature and of precipitation as percentage of the total annual precipitation for all ROI.

The Gurla Mandhata or Naimona'nyi massif is located in the south-western TP (Fig. 5.2, Table 5.1). This is an area of monsoonal and westerlies influence. Here a summer accumulation regime with a second precipitation maximum in February is identifiable (cf. Maussion et al. 2014a). Ye et al. (2006) found increasing glacier shrinkage in the Gurla Mandhata massif of 0.77 km² a^{-1} from 1999 to 2003. Tian et al. (2014) find a stronger thinning at Naimona'nyi glacier in the Gurla Mandhata massif between 2008 and 2010 (-1.34 m) than between 2010 to 2013 (-0.87 m), probably due to more than average precipitation in the latter years.

Table 5.1: Overview of spatial data and climate data of all study regions; MA: Muztagh Ata, GM: Gurla Mandhata, S: Surla, Sh: Shankangsham, TG: Targo Gangri. Elevation is given in m a.s.l.

ROI	**MA**	**GM**	**S**	**Sh**	**TG**	**PIC**	**NWN**	**SEN**
Location	38°14'N 75° 7'E	30°25'N 81°19'E	31° 2'N 83°28'E	31°34'N 85° 7'E	30°37'N 86°25'E	33°54'N 89° 8'E	30°41'N 90°6‘E	30°'4N 90°6‘E
Area (km²)	284	72,9	75	10,8	97	397	31	135
No. of pixels	4546	1089	1651	309	1455	6362	465	2025
Median altitude (m)	5160	6010	6100	5980	6010	5850	5810	5860
Elevation range (m)	3600	2300	1000	700	1000	1200	1100	1800
MOD02QKM processable (%)	41	22	26	20	27	33	25	24
Total number of scenes available for calculation	957	435	536	427	545	709	504	489
Mean transient snow line altitude, Jul - Sep (m)	4889	5895	5960	5841	5841	5687	5698	5742
Mean std. dev. (m) of transient snow line, Jul -Sep	95	54	27	37	24	37	45	37
Std. dev. of inter-annual median of transient snow line	37	30	9	16	13	11	18	10
Range ELA (m)	5018 - 5303	5923 - 6001	5972 - 6042	5875 - 5941	5856 - 5914	5705 - 5800	5728 - 5814	5766 - 5829
Mean ELA (m)	5130	5944	5997	5914	5888	5761	5784	5792
Std. dev. of ELA	90,6	23,3	23,2	21,3	21	27,8	29,6	22,2
Mean error of ELA	83,6	43,8	38,8	34,4	41,6	40,6	31,1	35,8
Average glacier slope (degree)	8	6,4	7,3	9	10,3	5,1	6,3	8,2
Mean precipitation (prec.) (mm a^{-1})	583	786	477	507	390	595	643	675
Std. dev. annual prec. (glaciological year)	71	162	134	114	109	75	129	141
Std. dev. temperature at 2 m above the ground (t2) December	1,2	1,1	1,1	1,3	1,26	1,3	1,2	1,3
Std. dev. t2 February	2,1	1,5	1,9	1,5	1,6	1,8	1,5	1,5
Std. dev. t2 June	1,4	1,0	0,7	0,7	0,6	1	0,8	0,8
Std. dev. t2 August	1,0	0,4	0,5	0,7	0,6	0,9	0,6	0,6
Std. dev. prec. December	12	13	3	3	2	5	2	2
Std. dev. prec. February	26	57	16	12	3	7	7	7
Std. dev. prec. June	33	57	41	39	34	30	34	37
Std. dev. prec. August	25	79	56	54	42	34	45	48
Mean wind speed (m/s) (400 hPa, July to September)	16,2	4,9	5,4	6,8	4,6	10,2	4,2	4,3
Mean prec. (mm/month) (July to September)	47	116	105	111	95	95	137	145

The detached Muztagh Ata massif is situated in the eastern Pamirs (Fig. 5.1). In the western margin of the TP, the monsoon influence (if any) is very weak. The westerlies are predominant with a precipitation maximum in spring (Maussion et al. 2014a). The glaciers belong to the extreme continental or cold glacier type (Huintjes, 2014).

Huintjes (2014) calculated the mass balance of Purogangri ice cap, Zhadang glacier, the Muztagh Ata glacier and the Naimona'nyi glacier in the Gurla Mandhata range from 2001 to 2012 using a physically based energy balance model. Yao et al. (2012) derived annual mass balances from in situ measurements for Muztagh Ata glacier (2002, 2003, 2006, 2008 and 2010) and Naimona'nyi glacier in the Gurla Mandhata massif (2006, 2008, 2009 and 2010) among others. Glacier mass loss generally decreases from the Himalayas to the continental interior, with slight positive mass balances observed on Muztagh Ata glacier in the eastern Pamir. Glacier thickness changes for the entire Pamir-Karakorum-Himalaya arc between 2003 and 2008 (Kääb et al. 2015) show lowering in eastern Nyainqêntanglha and the Gurla Mandhata region, but a slight thickening for the Gurla Mandhata region and even a slight thickness increase of up to 0.15 m per year for the easternmost Pamir comprising Muztagh Ata.

5.3 Data

5.3.1 MODIS data

We use the Terra and Aqua Level 1B Collection 05 MODIS swath data (MOD02QKM and MYD02QKM) with radiance calibrated on-board and global coverage every one to two days. The data set provides calibrated and quality assessed radiance. We work with band 1 (visible light, 620-670 nm) and band 2 (near infrared, 841-876 nm) which are provided at a spatial resolution of 250 m. The Terra (Aqua) satellite crosses the TP around noon (in the afternoon) at local solar time (Hall et al. 2006). We used Terra (Aqua) data from 01 July to 30 September in the years 2001 (2002) to 2012 (2012). We utilized the cloud mask provided in the Terra and Aqua snow cover level 2 swath data (MOD10L2 and MYD10L2) with a 500 m resolution (Hall et al. 2006).

5.3.2 ASTER Digital Elevation Model and glacier mask

Terrain elevations were derived from the ASTER Global Digital Elevation Model (GDEM), Version 2 available at the NASA Land Processes Distributed Active Archive Center as a contribution of METI and NASA. Its spatial resolution is 30 m. For each ROI, ASTER data was resampled to 250 m resolution using the nearest neighbour method and coregistered with the MODIS scenes to derive a single altitude per MODIS pixel. For calculation we considered MODIS pixels located in the glacier masks derived from the glacier outlines. The PIC glacier mask was obtained from Neckel et al. (2013). The masks for the Nyainqêntanglha range were taken from the Randolph glacier inventory (RGI, Pfeffer et al. 2014) Version 3.2, available at http://www.glims.org/RGI/. In this particular region the RGI glacier masks proved to be very accurate compared to the older Chinese glacier inventory (CGI, Shi et al. 2009) (Bolch et al. 2010). The glacier masks for the regions of Targo Gangri, Surla and Shankangsham (pers. comm. T. Bolch) were derived by a threshold approach on a Landsat band ration (band 3/band 5). The glacier masks of the Gurla Mandhata and Muztagh Ata massif from 2000 were provided by Nicolai Holzer, TU Dresden.

5.3.3 Climate data

Mean monthly climate data at 10 km resolution was obtained from the High Asia Refined reanalysis data (HAR10; Maussion et al. 2014a, http://www.klima.tu-berlin.de/HAR). For each ROI, an area covering the extent of the glacierized area plus a one pixel margin is considered (cf. Fig. 5.2). We selected the climate variables for their possible direct (2 m air temperature [°C] and precipitation [mm/h]), or indirect (wind speed [m/s], meridional and zonal component at 10 m above ground, 400 hPa and 300 hPa levels) influence on glacier mass balance.

To study large-scale climatic controls we used several standard teleconnection indices. The Hurrell North Atlantic Oscillation index (NAO) is defined as sea level pressure differences over the Atlantic sector (Fig. 5.4). It is provided by the Climate Data Guide of the National Centre of Atmospheric Research (NCAR UCAR, https://climatedataguide.ucar.edu/climate-data/ hurrell-north-atlantic-oscillation-nao-index-pc-based). The Indian summer monsoon index (ISM) is defined as the difference in the zonal wind speed at the 850 hPa level between 40°E-80°E, 5°N-15°N and 70°E-90°E, 20°N-30°N. It was obtained from the Asia Pacific Data Research Centre (APDRC, http://apdrc. soest.hawaii. edu/projects/monsoon/seasonal-monidx.html, 13 May 2014). The Southern Oscillation (SO), Arctic Oscillation (AO), Polar/Eurasia (POL), East Atlantic/Western Russia (EAWR), West Pacific (WP) and Pacific/North America (PNA) all present differences in sea level pressure as shown in Fig. 5.4. The Multivariate ENSO Index (MEI) includes six variables over the tropical Pacific to capture the ocean-atmosphere coupling of the ENSO phenomenon. The latter seven indices are obtained from the NOAA Climate Prediction Center, available at http://www.cpc.ncep.noaa.gov/. The Dipole Mode Index (DMI) is defined as a gradient between the sea surface temperature in the western and the eastern equatorial Indian Ocean (Fig. 5.4), obtained from the Japan Agency for Marine Earth Science and Technology, at http://www.jamstec.go.jp/.

Fig. 5.4: Locations of action of the considered circulation indices; sea level pressure [circle] or sea surface temperature (DMI), multivariate variables (MEI) or zonal wind (ISM) [box] anomalies; the signs indicate the anomalies during the respective positive phase.

5.4 Methods

5.4.1 Preprocessing

The swath data was projected using the ENVI plugin MODIS Conversion Toolkit (MCTK) providing automatic bow-tie correction. The reflectance data is returned as dimensionless numbers between 0.0 and 1.0. The snow cover data was resampled to a 250 m resolution using nearest neighbour interpolation and the binary cloud mask was extracted subsequently. For every ROI we saved each Terra and Aqua reflectance scene together with the respective glacier mask, digital elevation model and cloud mask. Each scene was then screened for quality assessment.

5.4.2 Snow/Ice Classification and Transient Snow Line Altitude

Considering the data within the glacier mask, we first applied the cloud mask and excluded erroneous pixels and scenes with linear distortions. After applying a spatial cloud filter (Spieß et al. 2015) scenes with less than 45% data coverage were excluded.

To differentiate snow and ice surfaces, a k-means cluster analysis was performed (cf. Shea et al. 2013). The result was monitored to exclude scenes which are fully snow covered and not suitable for a cluster analysis.

The mean altitude of the transient snow line was taken as the 13^{th} percentile of the snow covered altitudes, following a similar approach to that of Shea et al. (2013). In our earlier study using MODIS 500 m data at PIC, the absolute altitude using this threshold was validated against Landsat imagery (Spieß et al. 2015). For this study, four cloud-free Landsat images could be used for validation (Table 5.2; Fig. 5.5). The number of scenes is limited because the snow line has to be clearly visible and a MODIS scene with enough valid pixels has to be available for the corresponding acquisition date. A snow pixel area ratio (SAR = A_snow / A_total) was calculated was calculated for Landsat and MODIS scenes and the altitude of the digitized Landsat snow line was compared to the corresponding daily MODIS snow line altitude (Table 5.2). Within these four scenes the mean difference between the SAR of Landsat and the SAR of MODIS is minor. The mean difference between the mean snow line altitude (SLA) of Landsat and the 13^{th} percentile of MODIS snow pixel is 23 m. The Surla scene displays the largest discrepancy with the MODIS derived SLA being 73 m higher than the Landsat derived SLA. This can be ascribed to the poor MODIS data coverage of 56%. To account for the fact that incomplete data coverage of the single scene might result in an overestimation of the highest snow line altitude, the transient snow line altitudes are weighted by the percentage of the underlying data coverage (cf. Shea et al. 2013). In the considered Surla scene the SLA difference is thus reduced to 39 m after weighting. Varying the selected percentile between 10^{th} and 20^{th} leads to an absolute change of 61 m but it affects the variability of the ELA only negligibly (Spieß et al. 2015).

5.4.1 Equilibrium-line Altitude

Provided a required minimum of ten days holding valid reflectance data during the observation period is reached the resulting highest position of the transient snow line within the ablation period is taken as the ELA proxy. This approach differs slightly from those of other authors. Shea et al. (2013) who used the maxima from a Loess-smoothed time series of transient snow line elevations, Mernild et al. (2013) who used a second order polynomial regression to estimate the highest position of the transient snow line, Dumont et al. (2012) and Brun et al. (2015) who used the minimum albedo value to estimate the annual mass balance.

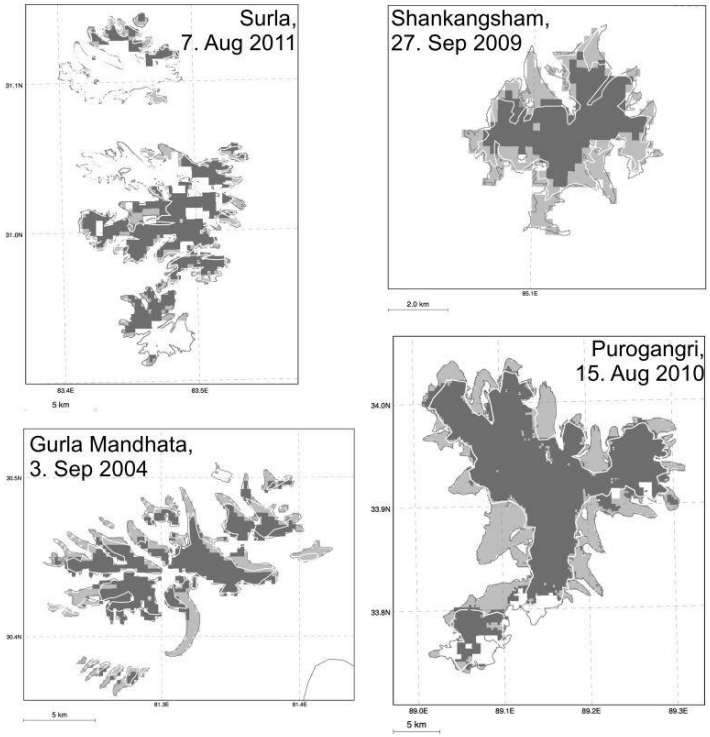

Fig. 5.5: MODIS snow (dark grey) or ice (light grey) pixels; digitized snow line from Landsat image (white line) within the glacier mask; Surla, Shankangsham, Gurla Mandhata and PIC.

Table 5.2: Comparison of the classified snow pixels area ratio (SAR), mean ($\overline{x}$) and standard deviation (σ) of snow line altitudes of Surla (S), Shankangsham (Sh), Gurla Mandhata (GM) and PIC from MODIS and Landsat satellite data. Elevation is given as m a.s.l.

	S	**Sh**	**GM**	**PIC**
Acquisition date	7 Aug 2011	27 Sep 2009	3 Sep 2004	15 Aug 2010
Valid pixel (%)	56	100	99	94
Landsat				
Path/Row	143/39	142/43	144/39	140/36
Sensor	TM 4/5	TM 4/5	L 7 ETM+	TM 4/5
SAR	0.45	0.67	0.58	0.61
$\overline{x}$ (m)	5880	5870	5891	5774
MODIS				
SAR	0.40	0.52	0.61	0.61
SLA 20th percentile (m)	5995	5905	5943	5828
SLA 14th percentile(m)	5965	5871	5896	5797
SLA 13th percentile (m)	5953	5870	5893	5790
SLA 12th percentile (m)	5948	5865	5890	5784
SLA 10th percentile (m)	5934	5857	5866	5768
σ (m)	22.99	18.41	28.02	22.10

The average annual cycle of albedo derived from the MODIS snow product data for Purogangri, Gula Mandhata und Targo Gangri shows its minimum within this period from July to September, even though the albedo also considerably declines during winter when there is little ablation but also no

accumulation. We used the same set of parameters for all ROIs to obtain a comparable proxy for the variability of the ELA, rather than aiming at retrieving true absolute altitudes.

5.4.2 ELA and climate

Finally, a single linear correlation analysis was performed in order to relate the inter-annual variability of the annual ELA to the underlying climate forcing represented by various monthly predictors and teleconnection indices as introduced in the data section. The correlations refer to conditions during the glaciological year from October of the preceding calendar year until September of the actual year (Spieß et al. 2015).

5.5 Results

5.5.1 Transient Snow Line Altitude

The transient snow line altitudes for all ROIs (Fig. 5.6A - Fig. 5.9A) are presented as yearly boxplots. The mean transient snow line altitude as well as the mean annual ELA is lowest at Muztagh Ata (4889 m a.s.l., 5130 m a.s.l.) and highest at Surla (5960 m a.s.l., 5997 m a.s.l.) (cf. Table 5.1). The mean standard deviation of yearly transient snow line ranges from 24 m at Targo Gangri to 97 m at Muztagh Ata. The standard deviation of the annual median transient snow line ranges from 9 m at Surla to 37 m at Muztagh Ata.

5.5.2 ELA

Inter-annual ELA proxies are shown in Fig. 5.6B - Fig. 5.9B. Uncertainty in the estimated ELA is related to the percentile used to calculate the transient snowline altitude, which was varied in this study between 10th and 16th. The errors range between 31 and 84 m. The year 2001 does not allow the calculation of the ELA proxy in most ROIs because the required minimum of ten days with valid reflectance data during the observation period is not reached. In Fig. 5.8B the inter-annual variability of the ELA proxy resulting from a previous method based on 500 m spatial resolution MODIS data (Spieß et al. 2015) is added for PIC. Both time series are highly and significantly correlated (r=0.91), showing that our method is robust. Additionally we show the inter-annual variations of various monthly climate predictors (Fig. 5.6C - Fig. 5.9C) and indices (Fig. 5.6D - Fig. 5.9D) featuring pronounced correlation with the inter-annual ELA proxy variability.

For example a significant correlation of the inter-annual ELA variability is present between SEN, NWN and Purogangri as well as between SEN and Shankangsham. A less significant correlation exists between SEN and Gurla Mandhata as well as between Targo Gangri and Gurla Mandhata (Table 5.3). But the time series do not all systematically correlate with each other. This is due not only to different reactions of the glaciers to climatic forcing but also the fact that the inter-annual variability of the climatic predictors is not uniform across the TP. Even ROIs spatially close to each other show differences in the inter-annual variability of temperature and precipitation (Fig. 5.7C, cf. Fig. 5.10). The standard deviation of the inter-annual temperature is higher in the winter months (highest at Muztagh Ata, Fig. 5.6) whereas the precipitation has a higher inter-annual variability in the summer months (Table 5.1). Not only the amplitude of the variability but also its algebraic sign can be different in the same year across the TP, confirming the essential different climatic patterns due to

large scale circulation and local factors. SEN and NWN show similar patterns of ELA proxies with a significant correlation (r=0.71; Table 5.3). The mean annual ELA of SEN lies 10 m higher and the variation is less pronounced (Table 5.1). The three ROIs in the central Trans-Himalaya show a similar progression in the inter-annual ELA, except for 2011 at Surla and 2007 at Shankangsham (Fig. 5.7B). The mean standard deviation of the inter-annual ELA ranges between 21 and 29 m in all ROIs, except for Muztagh Ata with 91 m (Table 5.1). The maximum difference in ELA between any two consecutive years is rarely above 50 m except for Muztagh Ata where this value exceeds 100 m. The skill of the percentile approach in estimating the transient snowline altitude (and consequently the ELA) can be seen by comparing the median altitude of glaciers in each ROI (Table 5.2). Median glacier elevation is commonly used to infer the ELA (e.g. Braithwaite and Raper, 2010).

Table 5.3: Pearson correlation coefficient (r) for correlation between the inter-annual ELAs of all ROIs. Significant correlations above the 0.1 level of significance are bold, correlations with p<0.01 are bold and underlined; MA: Muztagh Ata, GM: Gurla Mandhata, S: Surla, Sh: Shankangsham, TG: Targo Gangri.

ROI	MA	GM	S	Sh	TG	PIC	NWN	SEN
MA								
GM	-0.29							
S	0.17	0.10						
Sh	-0.01	**0.45**	0.09					
TG	-0.16	**0.57**	**0.44**	**0.73**				
PIC	-0.39	**0.46**	-0.22	**0.48**	0.33			
NWN	0.24	0.17	-0.16	0.20	0.11	**0.62**		
SEN	-0.16	**0.57**	**0.44**	**0.73**	0.29	**0.64**	**0.71**	

5.5.3 Climate and ELA

Correlations of annual ELA with climatic predictors from particular months are shown in Table 5.4 - Table 5.8. Some significantly correlated climatic predictors are shown in Fig. 5.6C/D - Fig. 5.9C/D.

At PIC stronger wind speed, easterly wind velocity and a negative phase of the AO are connected to a lower ELA (r=-0.75, r=-0.74, r=0.69). A negative (positive) phase of the NAO (WP) in February increases the temperature (r=-0.74, r=0.51) which favours sublimation and raises the ELA (r=0.65) (Table 5.4). The WP and POL form a quadrupole in February and March. A negative phase of the EAWR decreases the wind speed and raises the ELA (r=-0.61) in February and June. The precipitation in June lowers the ELA (r=-0.69) and increased wind speed at the 400 hPa level might reduce the convective precipitation (r=0.72). In July the temperature increases with southerly flow and raises the ELA (r=0.78). In September a higher wind speed is connected to a lower ELA. Neckel et al. (2013) found the mass budget of PIC to be close to equilibrium (-44 ± 15mm w.e. a^{-1} between 2000 and 2012) with slight thickening at higher and thinning at lower glacier elevations. This might be related to an increase in ablation due to higher temperatures and an increase in accumulation due to higher precipitation rates.

At the Nyainqêntanglha range a warmer and/or drier environment in November to February is leading to a higher ELA, possibly due to enhanced sublimation (e.g. NWN Feb.: r=0.78, r=-0.70, Table 5.5). At SEN a positive phase of the EAWR as well as of the NAO in February decreases the temperature and lowers the ELA (r=-0.69, r=-0.68). The precipitation effect in June as described by Mölg et al. (2014) is not seen in our data. In June and July the temperature increases the melt and raises the ELA (SEN: r=0.67, r=0.73). In July the temperature increase with southerly flow and raises

the ELA (SEN: r=0.77) whereas increased zonal wind seems to block this connection (SEN: r=-0.58). At NWN a positive phase of the MEI (El Niño) and DMI (warmer western Indian Ocean) from October to February leads to a lower ELA.

At Targo Gangri the lowest inter-annual variability in ELA may be connected to the largest mean slope (Table 5.1). Steep slopes do not favour clear correlation results. Positive phases of NAO and POL in February are connected to lower ELA and southerly flow in July to a higher ELA (Table 5.6).

Shankangsham is the smallest ROI with a mean slope of 9°, which makes the ELA proxy less reliable. Lower temperature and higher wind speed in March are connected to a lower ELA (r=0.60, r=-0.63). A positive phase of the DMI especially in June to August is connected to a lower ELA. In July southerly flow is connected with higher ELA (r=0.64) (Table 5.6).

Surla is the highest ROI with a median height of 6100 m a.s.l. (Table 5.1). No connections to the temperature and the precipitation are apparent (Table 5.6). Only the April correlations show significance, strengthened wind speed in that month is connected to a lower ELA (r=-0.63). Positive phases of the NAO and EAWR, which are here correlated with each other, lead to weaker wind speed in April and a lower ELA (r=0.58, r=0.77). Also in April a positive phase of the WP is connected to a lower ELA (r=-0.64). In July to September a connection to the DMI is visible (r=-0.61, -0.68), which hints towards a monsoon coupling.

For Gurla Mandhata the small-scale climate directed by the surrounding valleys and their orientation might be more important than large-scale forcing. Still some correlations are noticeable, with many in July, even though they do not involve temperature and precipitation (Table 5.7). In April enhanced wind speed raises the ELA (r=0.61). Higher temperatures throughout winter and spring also tend to raise the ELA. In July the dominant south-west wind direction might not bring snowfall which would explain the positive correlation of zonal and meridional wind (r=0.52, r=0.55). A positive phase of the WP in July, which prevails also in August is connected to a higher ELA (r=0.60, 0.58). Increased south-easterly flow in August is correlated with lowered ELA, but increased westerly winds correspond with an increased ELA (r=0.55). A positive phase of the ISM, which is associated with a stronger monsoon lowers the ELA (r=-0.76). During June to September the monsoon corresponds to a lower ELA. Positive ENSO phases from June to September tend to result in increased ELA (r=0.55, 0.52, 0.46, 0.40).

At Muztagh Ata only few correlations are evident in summer, except for precipitation in June and July (r=-0.52, -0.67) (Table 5.8). Here the summer precipitation at higher elevation mainly falls in solid form (Huintjes 2014). Increased precipitation in November and December, the months of minimum snowfall, lowers the ELA (r=-0.67, -0.63). The wind speed, dominated by the westerlies, lowers the ELA (r=-0.86 etc.). Additionally, positive phases of the NAO and AO enhance the wind speed, increase precipitation and lower the ELA (r=-0.75, -0.53, r=-0.72, -0.52). MEI is negatively correlated, especially in April and May when the maximum of precipitation occurs. El Niño is connected to a lower ELA (r=-0.64, -0.73). The SO shows the highest correlation in April, with a positive phase of the SO connected to a higher ELA (r=0.73).

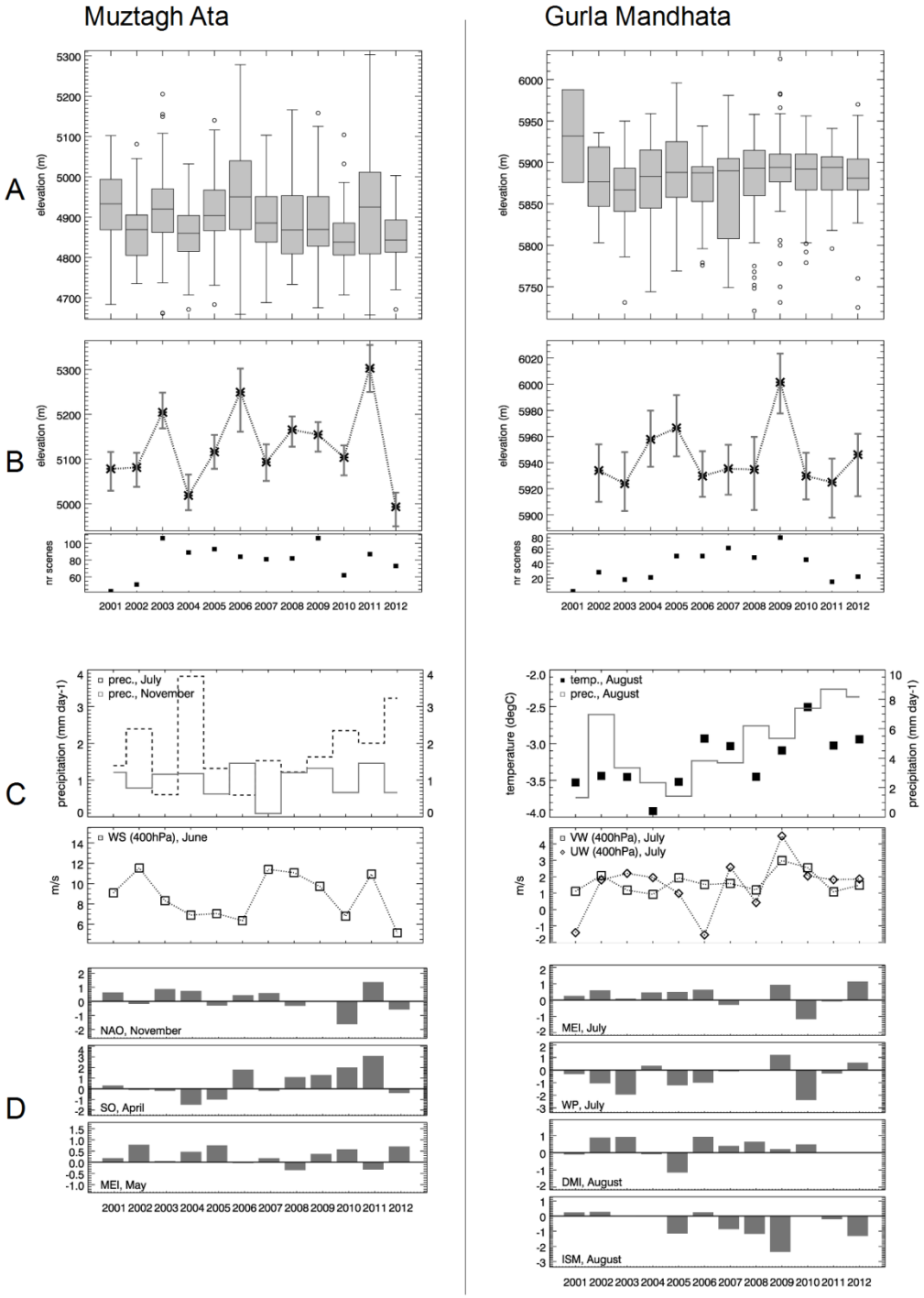

Fig. 5.6: Results for Muztagh Ata and Gurla Mandhata. A: Boxplot of the daily transient snow line calculated based on scenes with ≥ 45% valid pixels using the 13th percentile of the resulting snow pixels for each ROI from 1 July to 30 September for 2001-2012. Each box encloses the 75th and 25th quartiles, with a bar representing the median, and extends to the minimum and maximum (error bars); outliers shown as circles. B: Annual ELA calculated as highest weighted transient snow line altitude, error bars display uncertainty obtained by application of the 10th and 16th percentile (upper); number of scenes included in the calculation of the ELA (bottom). C: inter-annual variability of climatic predictors showing high correlation with the ELA. D: inter-annual variability of teleconnection indices that show high correlation with the ELA.

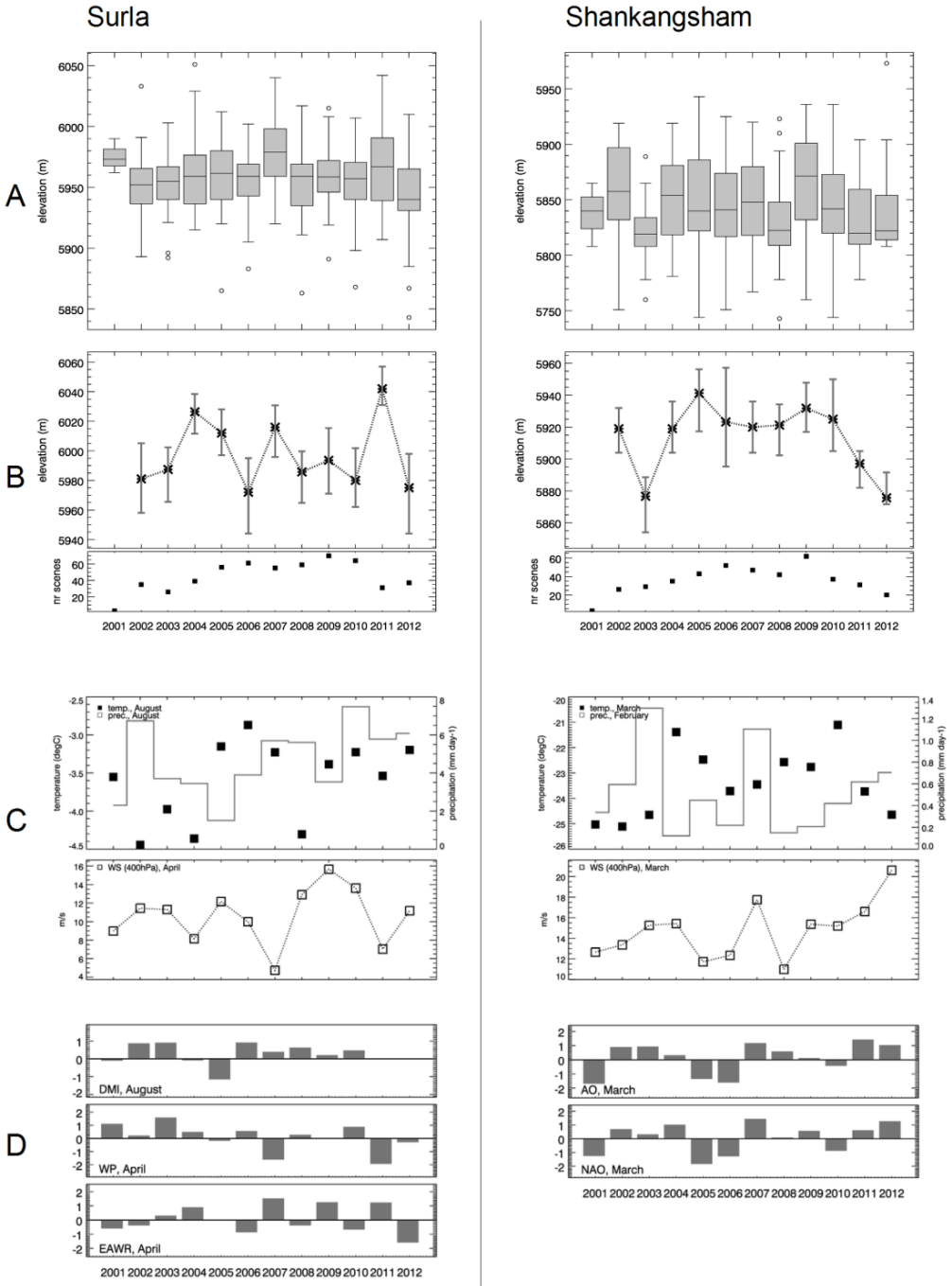

Fig. 5.7: Results for Surla and Shankangsham. As in Fig. 5.6.

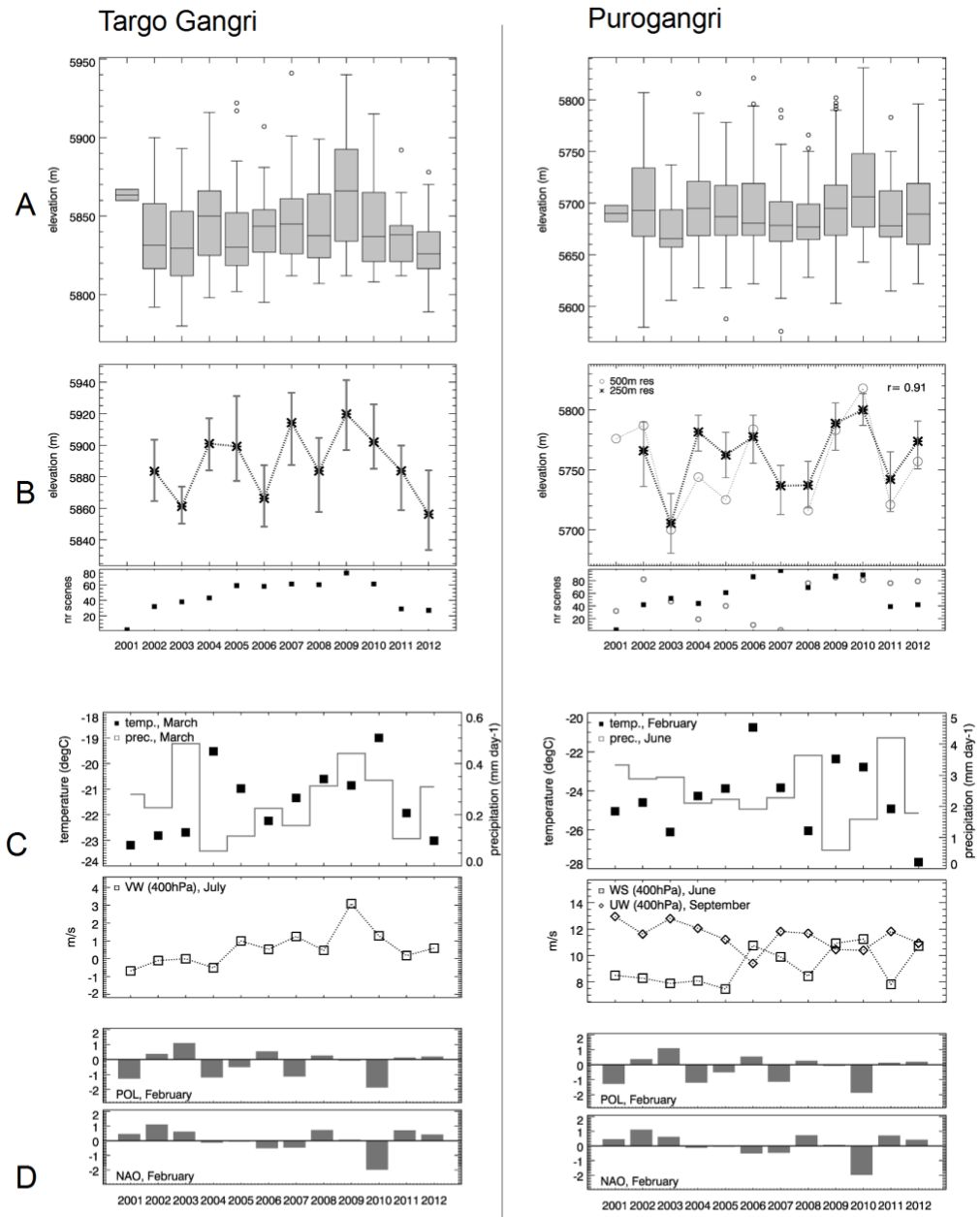

Fig. 5.8: Results for Targo Gangri and Purogangri. As in Fig. 5.6.

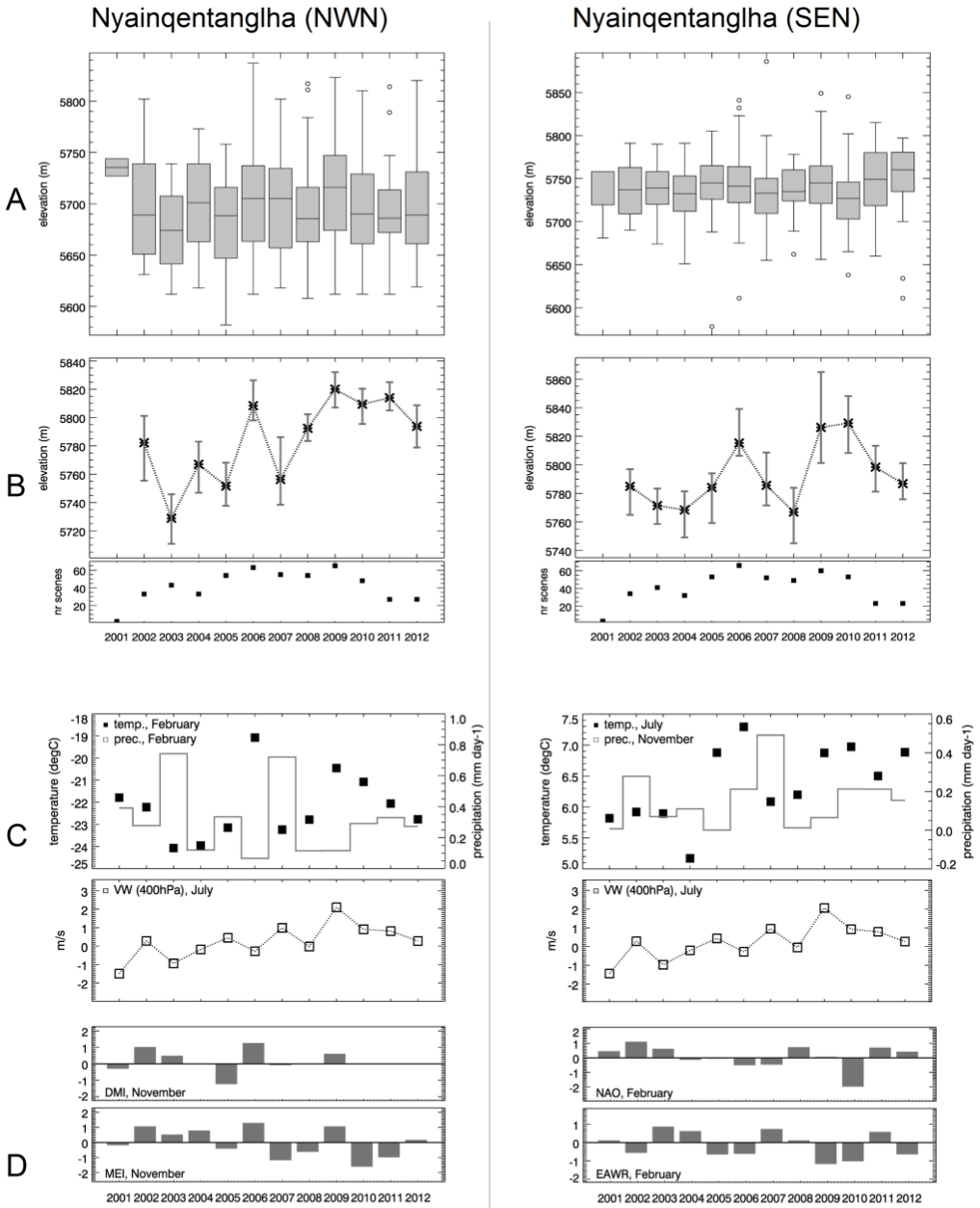

Fig. 5.9: Results for NWN and SEN. As in Fig. 5.6.

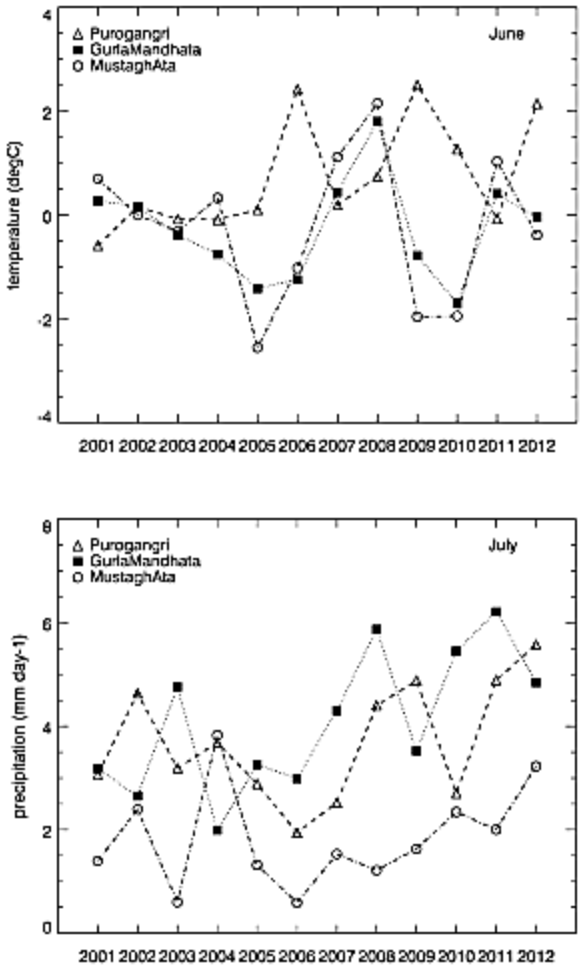

Fig. 5.10: Interannual monthly HAR temperature (top) and precipitation (bottom) for different study sites. This figure is not included in Spieß et al. (2016a, Annals of Glaciology).

Table 5.4: Pearson Correlation coefficient (r) for correlation between the inter-annual ELA and climatic predictors as well as between inter-annual ELA and atmospheric climate indices for glaciers at PIC; only relevant correlations are shown; significant correlations above the 0.1 level of significance are bold, correlations with p<0.01 are bold and underlined; WS: wind speed, UW: zonal wind, VW: meridional wind.

	November			February			June			July			September		
	WS (400)	UW (400)	AO	Temp.	NAO	EAWR	POL	WP	Temp	Prec	WS (400)	EAWR	Temp	VW (400)	VW (300)
PIC	**-0.75**	**-0.74**	**0.69**	**0.65**	**-0.74**	**-0.61**	**-0.64**	**0.51**	**0.52**	**-0.69**	**0.72**	**-0.64**	**0.61**	**0.51**	**0.59**

Table 5.5: As in Table 5.4 but for the western Nyainqêntanglha range.

	November						Dec.	January			February				June	July			
	Temp	Prec	WS (400)	UW (400)	DMI	MEI	Temp	Temp	Prec	MEI	Temp	Prec	NAO	EA WR	Temp	Temp	VW (400)	VW (300)	UW (300)
NWN	**0.74**			0.35	**-0.58**	-0.67	**0.71**	0.34	-0.43	**-0.64**	**0.78**	**-0.70**		**-0.57**			**0.55**	0.45	**-0.62**
SEN	0.35	**-0.67**	**0.65**	**0.62**				**0.60**	**-0.71**		**0.85**	-0.30	**-0.68**	**-0.69**	**0.63**	**0.73**	**0.64**	**0.77**	**-0.58**

Table 5.6: As in Table 5.4 but for glaciers in the Trans-Himalaya.

	January	February			March					April				July	August			Sept.
	Prec.	Prec.	NAO	POL	Temp	WS (400)	NAO	EAWP	AO	WS (400)	NAO	EAWR	WP	VW (400)	DMI	DMI	AO	PNA	DMI
S										**-0.59**	**0.58**	**0.77**	**-0.64**		**-0.61**	**-0.68**	**-0.67**		**-0.68**
Sh	**-0.53**	**-0.61**			**0.60**	**-0.64**	**-0.57**		**-0.62**						**-0.61**	**-0.59**			**-0.44**
TG			**-0.53**	**-0.70**	**0.68**			**-0.55**						**0.58**		**-0.51**		**0.70**	**-0.50**

Table 5.7: As in Table 5.4 but for Gurla Mandhata (GM).

	April	June	July								August				Sept.
	UW (300)	MEI	VW (400)	VW (300)	UW (400)	UW (300)	DMI	WP	MEI	AO	DMI	WP	MEI	ISM	MEI
GM	**0.61**	**0.55**	**0.55**	**0.58**	**0.52**	0.49	-0.47	**0.60**	**0.52**	**-0.65**	**-0.59**	**0.58**	0.46	**-0.76**	0.40

Table 5.8: As in Table 5.4 but for Muztagh Ata (MA).

	November							December				April		May	June	July
	Prec	WS (400)	UW (400)	NAO	EAWR	POL	AO	Prec	WS (400)	UW (400)	NAO	SO	MEI	MEI	Prec	Prec
MA	**-0.67**	**-0.89**	**-0.86**	**-0.75**	**-0.65**	**0.63**	**-0.72**	**-0.63**	**-0.55**	**-0.54**	**-0.53**	**0.73**	**-0.63**	**-0.73**	**-0.52**	**-0.67**

5.6 Discussion

The reliability of the calculation of the transient snow line altitude depends largely on the initial quality of the data. MODIS imagery, with spatial resolution of 250 m, is better able to cover glaciers of extensive plan form, such as ice caps, than valley glaciers. Increased glacier slope also decreases the richness of detail of a satellite picture. The precipitation regime affects the data coverage due to cloud cover. Additionally, a summer accumulation regime might make it harder to detect the highest transient snow line in the ablation period because of continuous snowfall. In this case the transient snow line is likely to reach its highest position in the post-monsoon months in September or early October (cf. Brun et al. 2015). We analysed the average annual cycle of albedo derived from the MODIS snow product data for Purogangri, Gurla Mandhata und Targo Gangri, which shows its minimum within the period from July to September. For summer-accumulation-type glaciers the scene with the highest snow line is more likely to be missing due to cloud cover, in which case the ELA may be underestimated.

Regional ELAs have been used to infer regional mass balance (Shea et al. 2013; Pelto and Brown 2012). However, within the same ROI, the transient snowline elevation can vary across individual glaciers. For example, the transient snowline elevation calculated for 15 August 2010 at 18 PIC glaciers varies from 5544 to 5807 m a.s.l. Despite this variation, the mass balances of different glaciers in a specific region often show very high correlations (Pelto and Brown 2012; Gardelle et al. 2013). Temporal variability in the mean ELA is thus likely to be similar to that of the individual glaciers within a ROI.

The variability of the ELAs across the TP is equal neither in form nor in strength. Gurla Mandhata and Muztagh Ata have significantly higher inter-annual variation in precipitation than the other ROIs. Muztagh Ata displays not only the highest intra-annual variability of the transient snow line but also the highest inter-annual variability of the ELA proxy and median of the transient snow line. The spring accumulation regime, with considerable precipitation throughout the year, distinguishes Muztagh Ata from the other ROIs. From July to September Muztagh Ata receives the least precipitation (Table 5.1). Hence the distinct pronounced difference in the snow line altitudes at Muztagh Ata could result from sudden severe precipitation. At Muztagh Ata the high inter-annual variability of the temperature in summer (Table 5.1) might indicate a temperature forcing even though it cannot be seen in mean monthly temperatures below melting point. From July to September wind speed is the highest at Muztagh Ata, which favours sublimation (Table 5.1). Sublimation accounts for more than half of the mass loss at Muztagh Ata despite high moisture content of the air (Huintjes 2014). Another explanation for the strong ELA variability would be a higher mass turnover, since it increases the altitude range of glaciers (Table 5.1). The mean total amount of precipitation does not support this hypothesis (Table 5.1) but due to uncertainties in the

absolute values of the HAR data and the very high portion of solid precipitation (Huintjes 2014), it may again be a plausible explanation.

The inter-annual variability of the ELA at Muztagh Ata shown in Yao et al. (2012) between 2006 and 2010 agrees well with our results. Yao et al. (2012) further reported a mean glacier retreat rate of 1.7 m a^{-1} at Purogangri from 1974 to 2010 and approximated a corresponding mean annual ELA of 5735 m a.s.l., which is only 30 m below our mean ELA from 2001 to 2012 (Table 5.2). We confirm the higher ELAs in the continental-climate-dominated interior and the lower ELAs of glaciers in the Pamir as stated by Yao et al. (2012). The results in this study indicate an apparently negative mass balance trend between 2003 and 2009 in the Western Nyainqêntanglha range (Fig. 5.9) while Kääb et al. (2015) report clearly negative mass balance for the Eastern Nyainqêntanglha range for 2003 to 2008.

When interpreting the correlations of the ELA with climatic predictors (Table 4-8) one has to bear in mind the limitation of the method, the short time series duration and the possibility of unreliable correlations with climatic predictors. Furthermore, correlation does not imply causation. Nevertheless high and significant correlations may well indicate climate-related forcing of the ELA proxy variability (Spieß et al. 2015). The absence of correlation, on the other hand, does not negate a physical connection to the evolution of the annual ELA proxy since the connection may be masked by other factors or may not show up as inter-annual variability.

We focused on monthly instead of seasonal correlations with climatic predictors. We conducted a correlation analysis between all considered predictors but they were not all shown in detail for clarity. Annual and seasonal climate indices were also examined. In general the correlations with the monthly indices reach higher significance. In only three cases did the annual positive or negative phase seem to influence the ELA more than a monthly or seasonal connection. An annual positive phase of the WP leads to a higher ELA at Gurla Mandhata (r=0.74). The annual EAWR is correlated to the ELA at Western Nyainqêntanglha range. At SEN the corresponding correlation coefficient (r=-0.72) exceeds the monthly correlation in winter. At Shankangsham an annual positive phase of the DMI is connected to the inter-annual ELA (r=-0.69).

The variation of glaciological responses to climatic forcings between ROIs is very complex because not only the response but also the climatic driving forces are different even between spatially close ROIs. There are strong differences in precipitation between regions and seasons on the TP (Curio et al. 2015). Teleconnections are even more complex to interpret when considering possible recycling of atmospheric moisture on the TP. Curio et al. (2015) find that local moisture recycling provides about 60% of the moisture on the TP. Also the snowfall in winter might have a storage function. Stored atmospheric moisture in snow might be recycled in the following warm season (Curio et al. 2015).

5.7 Conclusion

The examination of remotely-sensed ELAs, dynamically downscaled meteorology, and climate indices in this study demonstrates the varying and complex glacier-climate relations across the Tibetan Plateau. In very general terms summer air temperature is most important for the central and eastern parts of the Tibetan Plateau while winter precipitation has much relevance for glaciers in the west of the plateau. However, when looking into the details of spatially varying influences of various factors

on the inter-annual variance of the ELA it becomes obvious that individual patterns are much more complex.

The inter-annual variability of the ELA is less pronounced in summer-accumulation type glaciers, and it differs in form and strength even between spatially close ROIs.

Whereas increased westerly air flow in November enhances sublimation at PIC and Nyainqêntanglha, it is the driver of increased snowfall in the Pamirs leading to a contrasting regional pattern of ELA variability.

Higher temperatures throughout winter and spring tend to raise the ELA at Muztagh Ata, Gurla Mandhata, Shankangsham and the Nyainqêntanglha range, even though temperatures are well below freezing point. This finding suggests that sublimation is favoured by rising temperatures even during periods with temperatures below freezing point especially under arid conditions.

Strong southerly flow in July is connected to higher temperatures and is correlated with an increased ELA. Only at Muztagh Ata and Surla is this pattern not visible. Direct influence of the monsoon indicated through the ISM is only visible at Gurla Mandhata in August and NWN in July, but it is implied through the DMI at Gurla Mandhata, Surla and Shankangsham between June and September. Additionally, at Gurla Mandhata there might be a monsoon-ENSO coupling between June and September. An ENSO signal is traceable in the westernmost ROIs. El Niño in spring (summer) is connected to a lower (higher) ELA at Muztagh Ata (Gurla Mandhata). Whereas a positive phase of NAO in February or March is connected to higher wind speed and a lower ELA at PIC, SEN, Targo Gangri and Shankangsham, it is connected to lesser wind speed in April and a higher ELA at Surla.

Our study shows a wealth of interesting relations that can be obtained by the explication of remote sensing data of the snowline related to climate forcing. To expand our study's spatial coverage, future research activities will be focussed on ice fields along the northern fringe of the Tibetan Plateau. Most observational mass-balance studies to date aim at trends or temporally integrated glacier change of single glaciers and the relevant driving forces behind these changes. Our study however aims at inter-annual regional mean glacier mass balance variability. It would be of interest to concentrate on single glaciers to improve the validation by comparing with mass balance studies. The use of longer time series in the future and an enhanced correlation analysis may offer even more conclusive results with which to investigate climatic forcing mechanisms to glacier response on the TP.

6 Comparison of modelled- and remote sensing- derived snow line altitudes at Ulugh Muztagh, northern Tibetan Plateau

The ice cap Ulugh Muztagh in the central Kunlun Shan at the northern fringe of the Tibetan Plateau is a very isolated region with arid cold conditions. No observational meteorological or glaciological ground truth data is available. Using the Moderate-resolution Imaging Spectroradiometer (MODIS) Level 1 radiance Swath Data (MOD02QKM) with a spatial resolution of 250 m, transient snow lines during the months of July to September in 2001 to 2014 are derived. Results are used to calibrate the physical based Coupled Snowpack and Ice surface energy and Mass balance model (COSIMA). The model runs on a representative detail region of Ulugh Muztagh (UM) on a digital elevation model with the same spatial resolution as the MODIS bands. In the absence of field observations the model is driven solely by dynamically downscaled global analysis data from the High Asia Refined Analysis (HAR). We compare remote sensing derived and modelled mean regional transient snow line altitudes in the course of consecutive summer seasons in 2008 to 2010. The resulting spatially distributed snow cover, snow line altitude (SLA) and annual equilibrium line altitude (ELA) proxy of both methods coincide very well in their interannual variability in accordance with interannual variability of climatic conditions. Since SLAs of both methods do not consistently agree on a daily basis a usage of remote sensing derived SLAs for model calibration in the absence of field observation data is only limited feasible for daily analysis. ELA approximation using the highest SLA at the end of ablation period may not be applied to UM because the negative winter mass balance (MB) is not reflected in the summer SLA. The study reveals moderate negative MB for UM throughout the modelling period. The mean regional MB of UM accounts for -523±410 mm w.e. a^{-1} in the modelling period. Hence UM seems not to belong to the area of the 'Karakorum anomaly' comprising a region of positive mass balances in recent years which has its centre presumably in the Western Kunlun Shan.

6.1 Introduction

Within the current discussions on the climate response of glaciers in High Asia Mountain Area the Kunlun Shan is of distinct interest. Substantial glacier mass loss is documented across the Tibetan Plateau (TP) at Western Nyainqêntanglha Range (Bolch et al. 2010; Mölg et al. 2013; Wu et al. 2014), Eastern Nyainqêntanglha Range and the whole Himalaya Arc (Gardelle et al. 2013; Gardner et al. 2013; Neckel et al. 2014; Kääb et al. 2015). In contrast, the mass gain anomaly documented in the

Pamirs and Karakorum, the so called 'Karakorum anomaly', seems to have its centre further east in the Kunlun Shan (Kääb et al. 2015).

We studied and compared snow lines derived from a remote sensing approach with snow lines derived from the Coupled Snowpack and Ice surface energy and Mass balance model (COSIMA, cf. Huintjes et al. 2015a) driven solely by HAR data (Maussion et al. 2014). Thereby the daily mean altitude of the regional transient snowline (SLA) within the end of ablation period (01 July to 30 September) were derived using Moderate Resolution Imaging Spectroradiometer (MODIS) following approaches lined out in Shea et al. (2013), Brun et al. (2015), Spieß et al. (2015) and Spieß et al. (2016a).

The presented remote sensing method is used because it does not rely on in situ data, which is very sparsely available on the TP. The method proved to be valuable in other regions on the TP (cf. Spieß et al. 2015, Spieß et al. 2016a). Only few glaciological studies have been conducted so far at UM. The region promised to be feasible for application of the introduced method since it presents one of the biggest glacierized areas on the TP and is not dominated by summer precipitation, which allows investigation of snow cover at the end of the summer season by remote sensing. The presented research tests whether the combination of MODIS satellite data and the application of COSIMA results in reasonable findings for a remote area with debatable state of the glacier mass balance. The attempt was to calibrate the model to reproduce the absolute altitude span of transient snow lines, the estimated equilibrium line altitude (ELA) proxy as well as the progression of the altitude of the transient snow line within the end of ablation period as observed in MODIS imagery. Further, it is aimed at potentially providing an option to model energy balance and MB in a region with no available measured glaciological, meteorological or hydrological data for COSIMA model calibration based on MODIS remote sensing data.

6.2 Study site

The Ulugh Muztagh massif (UM) is an icecap comprising the eponymous peak in the highest part of the central Kunlun Mountains (westernmost part of the Eastern Kunlun Shan) close to the northern fringe of the TP (Molnar 1987a; Molnar et al. 1987b; Ward 1989; Fig. 6.1 A). The UM is situated at 35°23`N, 87°21`E. The first ascend of UM peak took place in 1985 (Molnar 1987a). The glacierized area at UM covers more than 600 km² (Guo et al. 2013). Its altitude ranges from 5200 to 6980 m a.s.l. with a median altitude of 5690 m a.s.l. Northward the topography of UM is rough with deep carved valleys. To the south (and to a minor extent to the east) the massif descends only 1500 m more smoothly to the plateau connected with the existence of outlet glaciers. In all directions the glaciers of UM drain into presumably endorheic, saline lakes. Permafrost occurs everywhere and glaciers are of the extremely continental type (Shi and Liu 2000).

UM is under the constant influence of continental air masses causing great annual and diurnal temperature variation and a distinct cold and arid climate (e.g. Wang et al. 2009). As given by HAR data (cf. chapter 3) the average annual air temperature is -11°C and monthly air temperature shows an annual range of 28°C (Fig. 6.2). At the median altitude of 5690 m a.s.l. the average monthly temperature in July is just about 0°C and often falls to −28°C in winter. Mean daily air temperatures above zero degree (positive degree day (PDD)) occur from Mid-June to Mid-September. According to HAR data the strongest of generally high wind speeds occurs in winter from western directions. The westerly jet starts to shift to the north in March marking the beginning of the precipitation season in

northern TP (Maussion et al. 2014a). The precipitation maximum at UM is reached in May to June (Fig. 6.2). In connection with the formation of the Tibetan Low the main wind direction at UM starts to change to northeast in May (Maussion et al. 2014a). In September the wind field shifts back to the zonal flow. During the ablation period the main wind direction changes from northeast in June and August to northwest in September. Information about the precipitation amount is sparse and imprecise. Summer precipitation contribution of about 60% based on Aphrodite data is quoted by Yatagai et al. (2012). Whereas Maussion et al. (2014a) found a JJA precipitation contribution of below 50% and a precipitation regime classified as early summer regime (AMJ) based on HAR data (Fig. 6.2). The annual precipitation given by HAR data in the UM region accounts for 668 mm y^{-1}. This value seems to be too high when compared to other citations (cf. chapter 5.2). At two weather stations in the Tarim basin, 240 km and 300 km from UM, a significant temperature increase is measured between 1954 and 2004 of above 0.17°C per decade whereas a slight increase in precipitation is documented at these stations (Guo et al. 2013).

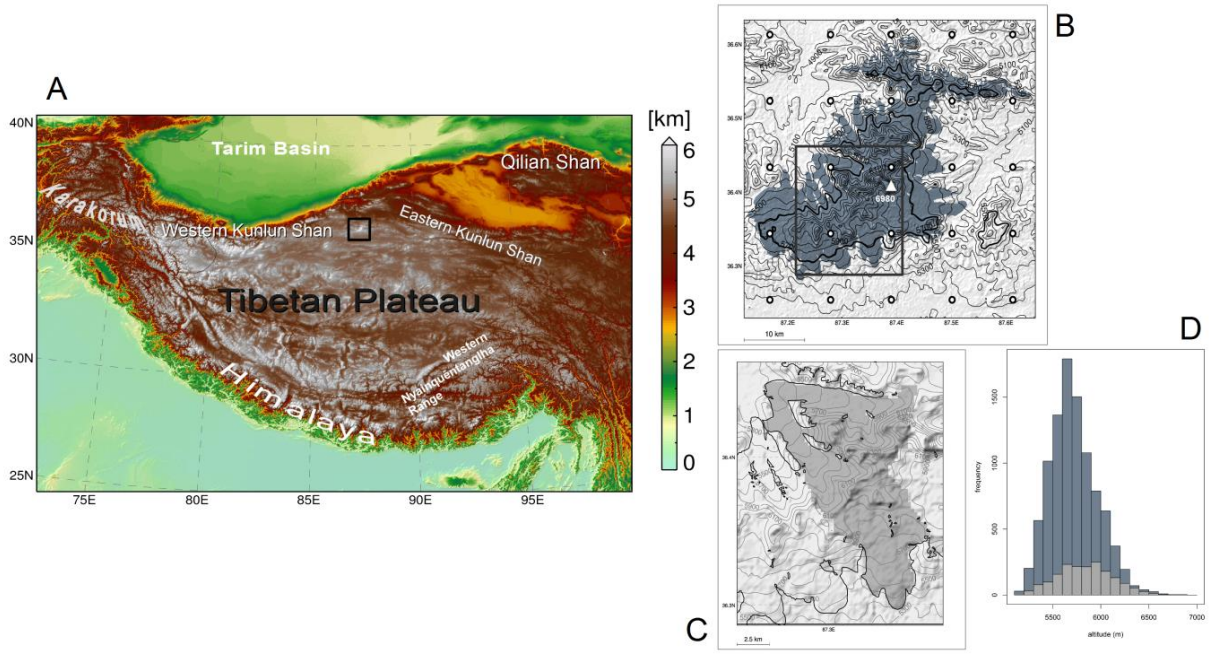

Fig. 6.1: The Tibetan Plateau (TP) with the location of the study region Ulugh Muztagh indicated as square (left). UM with High Asia Refined (HAR) Pixel centres shown as points (top right). The median altitude of the glacierized area in grey (5690 m a.s.l.) is indicated as a bold contour line, Ulugh Muztagh peak is indicated as white triangle. Contour lines are drawn in intervals of 100 m. The location of the detail region (UMdetail) is indicated as black square. UMdetail shown as greyed out area with the glacier mask as black line (bottom middle). Contour lines are drawn in intervals of 100 m. Altitude distribution of UM (dark grey) and UMdetail (light grey) (bottom right).

The ice fields along the northern fringe of the TP are not studied extensively on-site due to harsh environment and its remoteness. High altitude, extreme temperatures with low humidity, strong winds and the absence of roads makes field work very ambitious and expensive (Molnar 1987a; Burchfield et al. 1989; Qiu 2008). UM is studied for its intrusive rock deposit derived by melting in a thickened continental crust (Burchfield et al 1989; McKenna 1990; Yin and Harrison 2000; Molnar et al. 2010). Furthermore the Eastern Kunlun Shan is of high interest in seismic and tectonic studies because it represents a strike–slip fault accommodating the eastward motion of the plateau and connected to strong earthquakes (Van der Woerd et al. 2004; Qi et al. 2011; Shan et al. 2015). In the

western part of the Kunlun Shan three short term glaciological studies are mentioned by Bao et al. (2015). Within the Western Kunlun Shan some remote sensing approaches concerning glacier velocity were conducted (Yasuda and Furuya 2012; Guo et al. 2013; Yan et al. 2015) and Kääb et al. (2015) monitored MB using laser altimetry from ICESat. Chen et al. (2014) studied daily snow line altitudes derived from Landsat images between 2000 and 2013 on one east facing glacier at UM. Wu et al. (2013) measured snow depths and reflectance spectra in different slopes and aspects on April 14 to 26, 2012 at the far southeastern fringe of UM. To our knowledge no further observational climate or glacier data exists for UM.

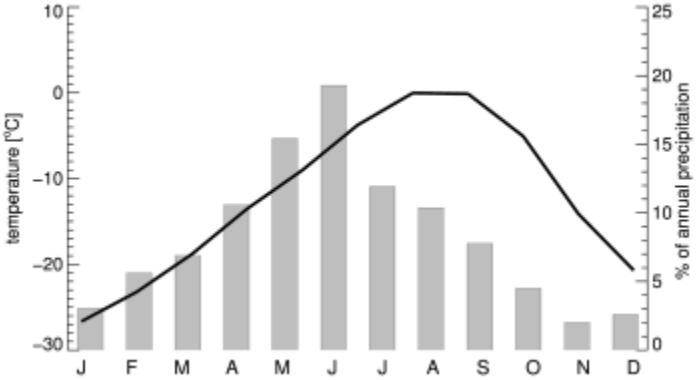

Fig. 6.2: Average annual cycle of monthly mean High Asia Refined (HAR) air temperature data at median altitude of 5690 m a.s.l. (ATO +0.5°C) and precipitation as percentage of the total annual precipitation.

The computational power available for this study did not allow for modelling of the whole UM. Due to extensive calculation time, it was necessary to limit the study region in the form of a representative profile across the ice cap. The detail region (UMdetail) comprises three main glacier tongues. One wide tongue is facing towards the south and two separated valley glaciers are facing towards the northwest joining at their fronts (Fig. 6.1 C). The latter two are named North Yulinchuan glacier and Central Yulinchuan glacier and their termini retreated by 440 m and 150 m between 1972 and 2004 respectively (Guo et al. 2013). Guo et al. (2013) found a surge event taking place on the Central Yulinchuan glacier between May 2008 and July 2009 using feature tracking resulting in a total of 590±26m glacier advance. The detail area covers roughly 119 km² and its altitude ranges from 5223 to 6827 m a.s.l. with a median altitude of 5874 m a.s.l. The altitude distribution of UMdetail is similar to that of UM with a slightly smaller range of altitudes and a little higher mean and median altitude (Fig. 6.1 D).

6.3 Data

6.3.1 MODIS data

We used Terra and Aqua Level 1B Collection 05 MODIS swath data (MOD02QKM and MYD02QKM) with radiance calibrated onboard and global coverage every one to two days. The data set provides calibrated and quality assessed radiance. Band 1 (visible light, 620-670 nm) and band 2 (near infrared, 841-876 nm) are provided at a spatial resolution of 250 m. The Terra (Aqua) satellite crosses the TP around noon (in the afternoon) at local solar time (Hall et al. 2006). Terra (Aqua) data from 01

July to 30 September were used from the period 2001 (2002) to 2014 (2014). The cloud mask is provided in the Terra and Aqua snow cover level 2 swath data (MOD10L2 and MYD10L2) with a 500 m resolution (Hall et al. 2006).

6.3.2 ASTER Digital Elevation Model and glacier mask

Terrain elevations were derived from the ASTER Global Digital Elevation Model (DEM), Version 2 available at the NASA Land Processes Distributed Active Archive Centre as a contribution of METI and NASA. Its spatial resolution is 30 m. For calculation we considered MODIS pixels located in the glacier masks derived from the glacier outlines. The glacier mask was manually digitized from Landsat 5 TM (07 September 2010, path 141, row 34) band combination 743.

6.3.3 Climate data

Hourly climate data at 10 km resolution from the High Asia Refined reanalysis data (HAR10; Maussion et al. 2014a; http://www.klima.tu-berlin.de/HAR) were used in this study. Altogether 17 HAR pixels were considered which include part of the glacierized area of Ulugh Muztagh according to the glacier mask (Fig. 6.1 B). As input data for COSIMA runs seven HAR variables were used. These include hourly means of incoming shortwave radiation (W m2), air temperature at (°C, 2 m), total precipitation (mm), surface air pressure (hPa), relative humidity at 2 m (%), wind speed at 10 m (m s-1) and cloud cover fraction. Average monthly mean and daily mean temperature and precipitation, as well as PDD were derived based on hourly HAR data, were averaged over those 17 HAR pixels comprising the glacierized area at UM (Fig. 6.2and Fig. 6.3).

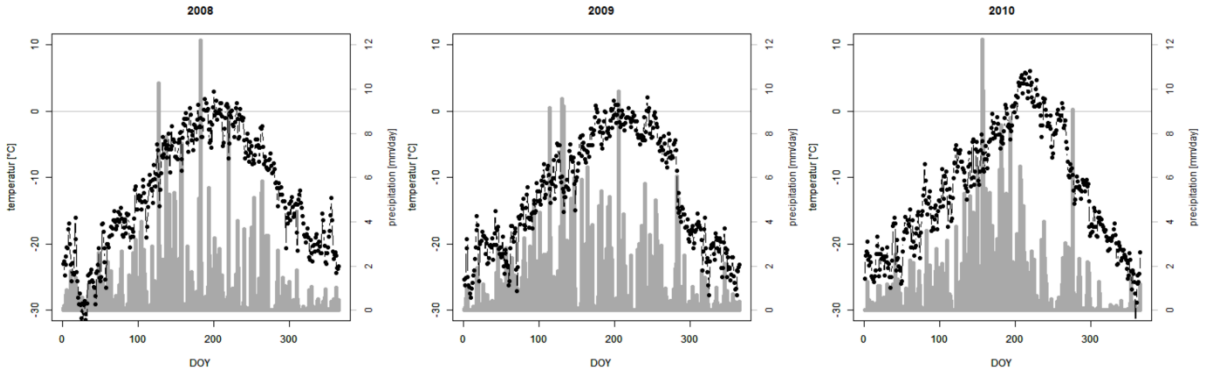

Fig. 6.3: High Asia Refined (HAR) daily temperature (ATO +0.5°C) and precipitation (PSF 0.5) data at median altitude of 5690 m a.s.l. displayed for the years 2008 to 2010.

6.4 Methods

Both, a remote sensing approach and a modelling approach were followed to derive transient snow lines at Ulugh Muztagh and to compare with each other.

6.4.1 Remote sensing approach

6.4.1.1 Preprocessing

The DEM was resampled to 250 m resolution using the nearest neighbour method and coregistered with the MODIS scenes to derive a single altitude per MODIS pixel. The MODIS swath data were projected using the ENVI plug-in MODIS Conversion Toolkit (MCTK) providing automatic bow-tie

correction. The reflectance data are returned as dimensionless numbers between 0.0 and 1.0. The snow cover data were as well resampled to a 250 m resolution using nearest-neighbour interpolation. The binary cloud mask was extracted subsequently.

First Terra and Aqua reflectance scenes were clipped to the glacierized region using the glacier mask. Then the cloud mask was applied to the two bands (Spieß et al. 2016a). In the course of quality assessment the scenes with linear distortions were excluded first. Afterwards a spatial cloud filter was used to reduce the data gaps due to cloud cover as in Spieß et al. (2016a) and essentially as proposed by Tang et al. (2013). Therein the mean reflectance value of the surrounding pixels was assigned whenever less than two thirds of a 5x5 moving-window was classified as cloud respective to the MODIS cloud mask. Finally, scenes with less than 45% valid data coverage were excluded for the classification of snow cover.

6.4.1.2 Classification of snow cover

To distinguish between ice and snow cover a k-means cluster analysis of the two MODIS bands was conducted to classify all glacierized and cloud-free pixels as either snow covered or snow free (cf. Shea et al. 2013; Spieß et al. 2016a; Fig. 6.4). To improve the physical accuracy of the unobserved cluster analysis the reflectance was checked for credibility subsequently: Based on results about spectral characteristics of Lopez et al. (2008), Dietz et al. (2012) and Goetz (2012) reflectance combinations of both bands with band 1 (band2) above 0.71 (0.54) were considered snow and reflectance combinations below 0.55 (0.46) were considered ice. An altitudinal cloud filter was applied consecutively two times to the classified map to further reduce cloud covered pixel: For all snow pixels with neighbouring cloud covered pixels a 5x5 pixel window was applied. Within this window each cloud covered pixel with a higher altitude than the centre snow pixel is assigned to snow. After these improvement procedures only scenes with more than 95% valid data coverage were considered for SLA calculation. To approximate the regional mean transient snow line altitude of the entire UM the 13th percentile of the snow covered altitudes was utilized (Shea et al. 2013; Spieß et al. 2015; Spieß et al. 2016a).

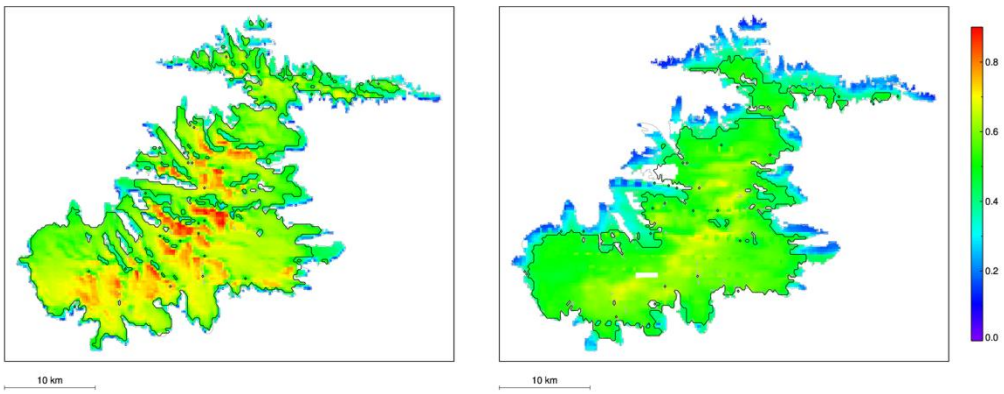

Fig. 6.4: MODIS band 1 (visible light, 620-670 nm) from 20 September 2003, 0725 (left) and 07 September 2010, 0410 (right). The black line indicates the border between snow covered and snow free pixels resulting from cluster analysis.

The selection of the period to be modelled was based on the quality of MODIS data. Years with a high amount of MODIS scenes in combination with a preferable uniform distribution within the study period and a notable inter- and intraannual variability of SLAs are desirable. Since the MODIS snow lines in 2010 were strikingly high and the subsequent years 2009 and 2008 hold a high amount of MODIS scenes we selected these three years for modelling. The corresponding remote sensing study of UMdetail exhibits one difference in the approach to derive the regional mean snow line altitude compared to the overall UM region. For the three-year-period selected for modelling with COSIMA, rather than using a percentile of the snow covered area elevation the transient snow lines on the glacier tongues were manually digitized. The altitudes of the line representing the transition between snow free and snow covered glacier were then averaged.

6.4.1.3 ELA approximation

To estimate glacier mass change one can exploit the close relation between a glacier's annual MB and its ELA. The highest SLA within the end of ablation period mirrors the ELA (Cogley et al. 2011; Rabatel et al. 2012; Shea et al. 2013). In distinction from earlier methods (Spieß et al. 2015; Spieß et al. 2016a) the method derives SLA from scenes with an improved physical accuracy and minimum data coverage of 95% per scene. Thereby the underlying number of scenes is reduced but the scenes are qualitatively more reliable.

6.4.1.4 Validation using Landsat satellite data

The MODIS derived snow lines were compared to Landsat imagery. Based on the necessity of snow line visibility, cloud free conditions and compatibility of acquisition date two Landsat scenes proofed to be reasonable for comparison on a daily basis (Table 6.1). At 20 September 2003 (07 September 2010) the regional mean SLA derived from high resolution Landsat imagery differs from the MODIS derived mean regional snow line by 8 m (29 m) with an accumulation area ratio of 0.77 (0.67). The spatial comparison showed good results even though there is a tendency to underestimate the snowline in the south and east and to overestimate the SLA in the north and west declivity (Fig. 6.5). The local time of MODIS acquisition is 03.25 pm and 12.10 pm.

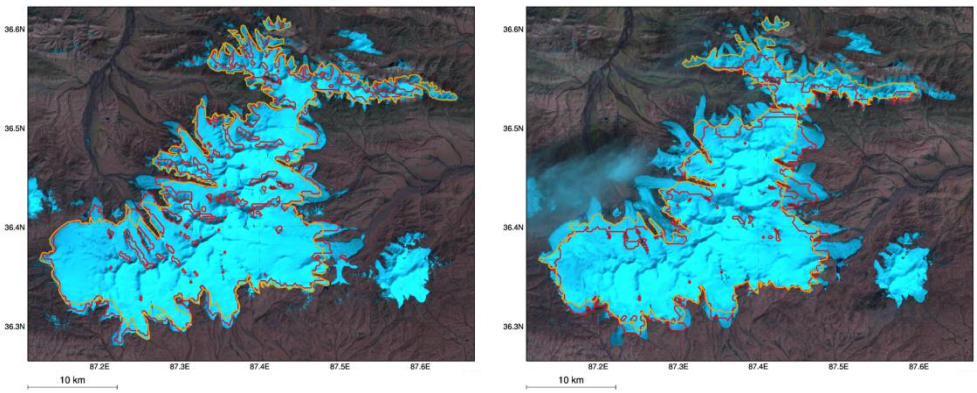

Fig. 6.5: MODIS derived snow line (red) and manually digitized (yellow) on Landsat scene; 20 September 2003, 0725 (left) and 07 September 2010, 0410 (right)

Table 6.1: Comparison of Landsat manually digitized and MODIS derived snow line altitude (SLA), altitude difference (\) and accumulation area ratio (AAR). Error estimates are explained in the text.

Date	LANDSAT SLA [m a.s.l.]	MODIS SLA [m a.s.l.]	\ [m]	MODIS AAR
2003_09_20_0725	5505 ±24	5513±85	8	0.77
2010_09_07_0410	5574 ±24	5603±85	29	0.67

6.4.1.5 Uncertainty assessment

Errors in the classification of snow were reduced via thoroughly use of spatial cloud filter. Uncertainty in spatially incomplete coverage was minimised using only scenes with data coverage of at least 95%. Errors due to topographic shading were minimised by using scenes acquainted at 03.25 pm and 12.10 pm. Since solar noon is at about 02.15 pm local time, shading on north facing glaciers might still occur. The effect of shading is not quantified but qualitatively might increase the risk of misclassification as ice.

Many regions on the TP are influenced by the Indian summer monsoon (Mölg et al. 2012; Mölg et al. 2014; Maussion et al. 2014a). In contrast precipitation maximum at UM appears in spring to early summer. Non-continuous cloud cover at the end of the ablation period at UM allows the investigation of snow lines in satellite pictures (cf. Spieß et al. 2016a). For the comparison of SLA of UM with Landsat data the uncertainty of the MODIS derived SLA was calculated by Gaussian error propagation of the standard deviation (2002-2014) and the maxima difference in ±3 percentile for the SLA (Table 6.1; Spieß et al. 2015; Spieß et al. 2016a).

Since no percentile is used in deriving the SLA of UMdetail the standard deviation of the SLA at the end of ablation season of 2008 to 2010 was used for uncertainty instead. Inaccuracies in the manually digitized snow line from Landsat imagery can occur due to subjective assessment of the spatial snow line pattern. To quantify the uncertainty we applied an accuracy of ±5% of the daily snow covered glacier area adapted from Paul et al. (2013) given the sufficient contrast of the ice to the surrounding regions. This uncertainty translates into an error of the inferred daily SLA corresponding to a maximum of 25 m (Table 6.1) Exact altitude of the mean altitude of the transient snow line is limited due to the spatial resolution of 250 m. On the glacier tongues where snow lines appear maximum elevation steps in steep terrain between neighbouring pixels account for up to 150 m. Considering thin and patchy snow cover commonly exists on the TP small scale spatial differences in snow cover might not be represented in the 250 m resolution.

6.4.2 Modelling approach

For this study COSIMA was run on a DEM with a spatial resolution of 250 m as well as with a resolution of 1000 m in case of calibration runs. The model is described in detail in Huintjes et al. (2015a). We here only supply a short overview of its functionalities.

6.4.2.1 COSIMA

COSIMA couples a surface energy balance (SEB) and a multilayer subsurface snow and ice model. The parameterization of subsurface energy and mass fluxes within COSIMA is directly coupled to the surface processes. COSIMA calculates meltwater percolation, the refreezing process within the snowpack under consideration of latent heat release and resulting subsurface melt, as well as the effects on subsurface temperature, snow density, and ground heat flux. To compute MB and SEB

several modules are combined in COSIMA for e.g. solving the heat equation, calculating surface temperature and energy balance, calculating percolation, refreezing and densification of snow.

Surface MB is derived at an hourly time-step as the sum of mass gains by solid precipitation, refreezing of liquid water in the snow pack and deposition, and of mass losses by surface melt, sublimation and subsurface melt (Huintjes et al. 2015a). The SEB is calculated from incoming shortwave radiation (SW_{in}), surface albedo (α), incoming and emitted longwave radiation (LW_{in} and LW_{out}), the turbulent fluxes of sensible and latent heat (Q_{sens} and Q_{lat}) and the ground heat flux (Q_G). Heat flux from liquid precipitation is neglected. Energy fluxes directed towards the surface are defined as positive. The resulting flux F is equal to the melt energy at the surface (Q_{melt}) only if the surface temperature (T_s) is at the melting point (273.15 K). T_s is calculated iteratively from the energy available at the surface. This procedure requires an equilibrium between the SEB fluxes.

The subsurface module of COSIMA is designed in a vertical layer structure that consists of layers with an equal thickness of 0.1 m (Huintjes et al. 2015a). Each subsurface layer is characterized by a temperature, density, liquid water content and depth. The initial temperature profile is linearly interpolated between the air temperature and a constant bottom temperature of -5°C adopted from measurements at Zhadang glacier (Huintjes et al. 2015a). In this study, glacier-wide initial snow depth was set to zero. Thus, the subsurface density profile is initialized with a constant density of 917 kg m^{-3} for glacier ice (Huintjes et al. 2016).

6.4.2.2 Preparation of data

Forcing parameters are incoming shortwave radiation (W m^{-2}), air temperature (K, 2 m), relative humidity (%, 2 m), air pressure (hPa), wind speed (m s^{-1}, 10 m), all-phase precipitation (mm), and cloud cover fraction. The meteorological HAR input parameters, except shortwave radiation, were taken directly from the highest central HAR Pixel at UM with a mean altitude of 5739 m a.s.l. Altitudinal gradients of climate variables were calculated from 17 HAR grid cells covering UM (Table 6.2) and used for the distributed COSIMA run. For cloud cover no distinct altitude dependency could be determined. Glacier-wide initial snow depth was set to zero since no information about the actual height is adducible. The starting point of modelling was at the end of the ablation period with a snow free scene theoretically conceivable. The HAR shortwave radiation was downscaled using the solar radiation model after Kumar et al. (1997) which calculates clear sky direct and diffuse shortwave solar radiation considering terrain shadowing and geographical position on the model run resolution. A ratio was calculated between the Kumar radiation and the averaged Kumar radiation corresponding to the highest HAR pixel with minimum terrain shadowing. By multiplying each ratio with the respective HAR cloud cover corrected radiation the input shortwave radiation considers both high resolution (250 m/1000 m) terrain shadowing and cloud coverage (cf. Huintjes et al. 2015b).

The years 2008 to 2010 contained a comparatively high MODIS scene coverage and evident intra- and inter-annual variability in SLA favourable for this pilot study. The model was run for a five year period from 01 October 2005 to 30 September 2010. The first two years were used as spin-up period and were not discussed as results. In the following the period between 01 October 2007 and 30 September 2010 is referred to as ‘modelling period’ and the three periods 01 July to 30 September in the years 2008 to 2010 are referred to as ‘observation period’. The model outputs used in this study were SEB and MB components as well as daily distributed mass balance, spatial snow field and snow height data.

6.4.2.3 Mass balance and mean regional SLA

For each glaciological year the climatic mass balance was calculated as spatially averaged mean mass balance of the glacierized area. The SLA was derived from COSIMA snow field output data by averaging the altitude of all snow cover pixels that were directly neighbouring snow free glacier pixels. If the whole glacier area was covered by snow or if the glacier was completely snow free the SLA was undefined.

Table 6.2: Altitudinal gradients calculated from 17 HAR grid cells covering UM and applied within COSIMA run.

Variable	Altitudinal gradient
Precipitation	0.0051 mm/100 m
Air pressure	-6.8100 hPa/100 m
Relative humidity	1.7870 %/100 m
Temperature	-0.7088 C/100 m
Wind speed	0.3940 m s^{-1}/100 m

6.4.2.4 Model calibration

The model was calibrated to fit the absolute altitude span within the ablation period and the annual ELA proxy, described as maximum SLA at the end of ablation period, of remote sensing derived snow line. Allowing a spin-up time of one year all calibration runs cover the period from 01 October 2006 until 30 September 2010, except for the first run from 01 October 2007 to 30 September 2010 (Table 6.3). Application of a lower spatial resolution of 1000 m was necessary to reduce calculation time. The goal was to fit the model for a general good reproduction of the remote sensing derived SLA progression within the observation period. The absolute altitude was additionally supervised by a spatial comparison with daily remote sensing derived snow line.

Mölg et al. (2012), Huintjes et al. (2015a) and Huintjes et al. (2015b) found a good representation of the seasonal HAR precipitation cycle at Zhadang and Purogangri on the TP but had to correct the precipitation amount with a factor of 0.56 and 0.7 respectively. With an annual precipitation of 668 mm y^{-1} given by HAR data a precipitation bias is conceivable in the study area but it is not verifiable without ground truth data. Hence the PSF was estimated considering published information (Mölg et al. 2012; Huintjes et al. 2015a; Huintjes et al. 2015b). We applied a precipitation scaling factor (PSF) varying between 0.4 and 0.7 in the calibration runs. First results with PSF 0.7 and 0.6 exposed no snow lines at all in the ablation periods. Since the PSF reduces the precipitation proportionally but never produces zero precipitation the precipitation amount was further analysed. We decided to account for snow drift and relocation processes, not included within COSIMA, by setting a threshold of minimum hourly all phase-precipitation amount above which snowfall is considered to actually locally settle on the glacier surface. This threshold was set to 0.5 mm h-1 considering snowfall below 1 mm h-1 as light snow (Rasmussen et al. 2003) which is easily blown away.

With this the absence of snow lines continued for the whole observation period. The resulting snow heights at lower glacier areas disclosed very low but positive values. Keeping in mind the coarse spatial resolution of the MODIS imagery a thin patchy snow cover is likely not to be seen within MODIS. This argument led to the determination of a snow height threshold. Pixels with resulting snow heights below 2.5 cm are taken as ice surface before comparing model results with MODIS

data. Applying both thresholds and setting a PSF down to 0.6 (results in annual precipitation of 368 mm y^{-1}) produced SLAs in 2010 eventually (Table 6.3).

However, SLAs derived using PSF 0.5 were lower than the ones derived from MODIS data. Actually, barely no snow line appeared in the year 2009 (Table 6.3) in contrary to what can be observed in the MODIS imagery. Taking into account that the temperatures within HAR data rarely reach the melting point in 2009, with only four annual PDD a cold bias within HAR data was assumed. Therefore, for further calibration we introduced an air temperature offset (ATO) varying from 0°C to +2°C.

An overview of the results of most calibration runs is given in Table 6.3. No calibration run revealed a highly precise congruence with the remote sensing derived SLAs on a daily basis. Nevertheless, crucial factors in deciding on a parameter combination for the model run were the interannual variability of the modelled MB and remote sensing derived ELA proxy. The combination for the final run was chosen to meet the criteria of preferably small difference between modelled and remote sensing derived SLAs. The statistical criteria were differences in mean and maximum of the SLAs in the observation period as well as a small root mean square error (RMSE) and good correlation of the temporal corresponding SLAs (Table 6.3). Two parameter combinations with PSF 0.5 (0.55) and ATO +0.5°C (+2.0°C) yielded similar results as best fits (Table 6.3). Furthermore the congruent overall progression was a deciding factor. The progression within the observation period is shown in Fig. 6.6 for the best fitting calibration runs. Weighing the results the final run discussed here was calculated on the DEM with a 250 m resolution, PSF 0.5 and ATO +0.5°C. The final parameter combination produces a reasonable annual precipitation of 334 mm y^{-1} and 41 PDD in average per year (2001 - 2014). In the following precipitation and air temperature refer to these adjusted HAR variables. As a second run for comparison the parameter combination of PFS 0.55/ATO +2.0 was used.

6.4.2.5 Uncertainty

The subject of model uncertainty is covered in detail in Huintjes et al. (2015b). COSIMA has been verified at Zhadang glacier for the point location as well as for the spatially distributed model run (Huintjes et al. 2015a). Since no atmospheric or glaciological in-situ measurements are available for the region of UM, the structure of COSIMA, the applied parameterisations, constants and assumptions set for Zhadang glacier remain unchanged. We assume that the resulting error in mass balance and snow cover due to an increased bottom temperature is not deciding since the change in overall heat conduction in snow and ice in the uppermost meters would be very small. Forcing COSIMA solely with HAR data was evaluated for Zhadang glacier (Huintjes et al. 2015a). Results accurately reproduced surface height change, MB and energy and mass fluxes. Furthermore, COSIMA shows good results at the Purogangri ice cap, central TP, as evaluated by comparison to geodetic mass balance (MB) from TanDEM-X data acquired in 2012 and SRTM-X data acquired in 2000 (Huintjes et al. 2015b). Huintjes et al. (2015a) determined a glacier-wide model uncertainty of 600kg m^{-2} a^{-1} at Zhadang glacier. Since no glaciological in situ measurements are available for UM the model uncertainty is assumed to be larger and can hardly be quantified. We addressed uncertainties in the subsurface temperature, water content and snow density by including a model spin-up period of two years. To obtain a model uncertainty for SLA at UM, accounting for precipitation- and temperature uncertainties, five model runs with varying PSF (0.55±0.5) and ATO (0.5°C±0.5) with a resolution of 1000 m and a shortened modelling period from 01 October 2006 to 30 September 2010 were performed. Exact altitude of the SLA and spatially exact snow cover representation are limited due to the spatial resolution of 250 m as it applies for the remote sensing method as well (cf. chapter

6.4.1.5). The accuracy of the altitudinal gradients are based on 17 HAR grid cells which partly cover larger non-glacierized areas. Thus they are not strictly representing gradients for the micro-climate situation on glaciers.

Table 6.3: COSIMA runs for calibration with different parameter combinations (PSF/ATO) and resulting mean annual precipitation (prcp) as well as mean annual PDD amount (PDD) from adjusted HAR climate data. COSIMA model results within the observation period (01 July – 30 September): Mass balance (MB), highest transient snow line in study period (max SLA), mean SLA based on temporal congruent scenes of both methods (mean SLA), difference between highest and lowest modelled SLA in study period (max SLA – min SLA), standard deviation of modelled SLA in study period (std). Comparison between modelled and remote sensing derived SLA within the observation period (01 July – 30 September): Difference between remote sensing derived maximum SLA and modelled maximum SLA (\max SLA), difference between remote sensing derived mean SLA and modelled mean SLA (based on temporal coinciding scenes) (\mean SLA), root mean square error (RMSE), correlation coefficient after spearman (r) and corresponding p-value (p)

				COSIMA					**Method comparison**				
PSF/ATO	Year	Prcp [mm]	PDD	MB [m w.e.]	Max SLA [m]	mean SLA [m]	max SLA –min SLA [m]	std [m]	\max SLA[m]	\mean SLA [m]	RMSE [m]	r	p
0.6/ +0.0	2008	401	30	-	-	-	-	-	-	-	166	-0.65	0.02
	2009			0.01	NA	NA	NA	NA	NA	NA			
	2010			-0.31	5453	5348	146	53	374	265			
0.5/ +0.0	2008	334	30	-1.45	5674	5525	207	78	2	-3	138	-0.39	0.02
	2009			-0.04	5430	5430	0	0	162	17			
	2010			-0.52	5658	5524	207	68	169	186			
0.4/ +0.0	2008	267	30	-1.69	5934	5852	661	118	-259	-329	313	0.18	0.17
	2009			-1.29	5886	5738	392	116	-294	-254			
	2010			-1.41	6018	5822	569	167	-191	-154			
0.55/ +1.0	2008	368	56	-0.22	5587	5463	313	66	89	56	173	0.26	0.15
	2009			0.08	NA	NA	NA	NA	NA	NA			
	2010			-0.39	5637	5470	293	77	191	205			
0.55/ +2.0	2008	368	95	-0.52	5666	5562	274	86	10	-40	138	0.49	0.0009
	2009			0.03	5438	5437	129	47	154	-14			
	2010			-0.74	5911	5625	519	152	-84	37			
0.5/ +0.5	2008	334	41	-0.46	5750	5563	477	100	-74	-42	140	0.47	0.0018
	2009			-0.08	5558	5468	119	39	34	-18			
	2010			-0.54	5825	5562	552	132	1	113			
0.5/ +1.0	2008	334	56	-0.62	5790	5601	516	117	-114	-79	163	0.395	0.006
	2009			-0.16	5566	5468	224	37	26	-21			
	2010			-0.61	5888	5581	579	165	-61	81			
0.45/ +0.0	2008	300	30	-0.90	5784	5665	218	72	-108	-142	173	0.30	0.035
	2009			-0.44	5611	5556	338	57	-19	-86			
	2010			-0.83	5911	5697	469	149	-84	-23			
0.55/ +0.5	2008	368	41	-0.77	5566	5416	257	81	110	106	192	0.049	0.8
	2009			-0.13	NA	NA	NA	NA	NA	NA			
	2010			-0.26	5610	5480	168	57	217	230			
0.45/ +0.5	2008	300	41	-1.11	5897	5705	624	1354	-221	-181	197	0.352	0.011
	2009			-0.57	5657	5574	304	5	-65	1			
	2010			-0.96	6941	5698	575	160	-115	-36			

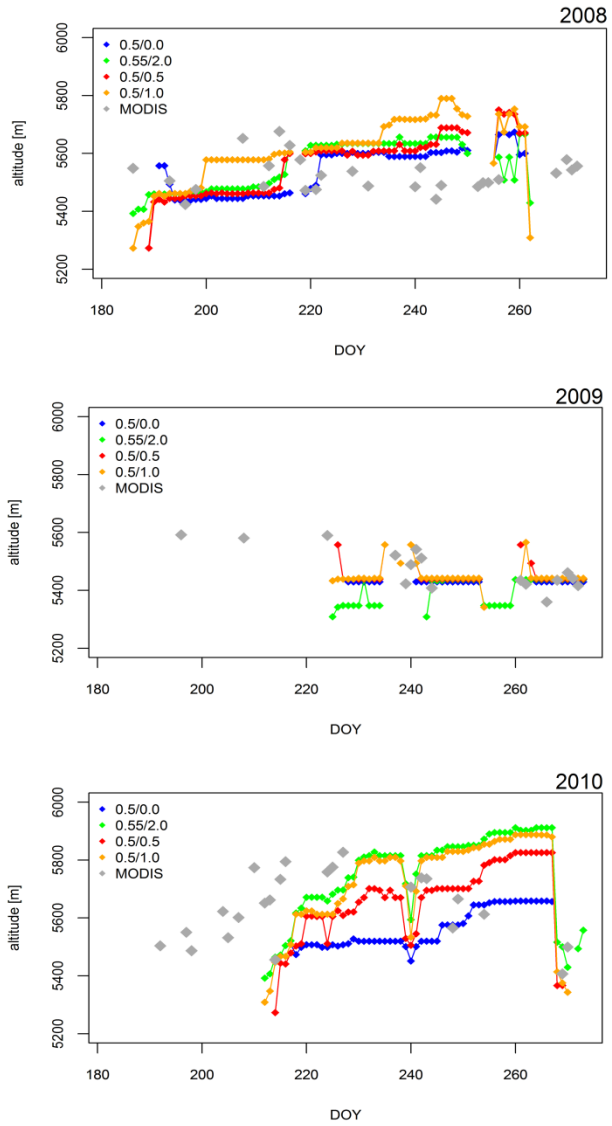

Fig. 6.6: Snow line altitudes (SLA) resulting from calibration runs with a spatial resolution of 500 m and different parameter combinations (coloured). Remote sensing derived SLA (MODIS) in grey.

6.5 Results and Discussion

Results of this study are remote sensing derived and modelled SLA. The variability and total height of the daily mean regional SLA of both methods within the observation period are compared. A visual spatial comparison of the snow line is conducted as well. A short overview is given on MB and SEB components of UMdetail given by COSIMA output.

6.5.1 Results of remote sensing approach

6.5.1.1 Entire UM

The annual distribution and interannual variability of the MODIS derived snow lines from 01 July to 30 September in 2001 to 2014 are shown in Fig. 6.7. In case more than one scene per day was available a daily mean was calculated as SLA. The year 2001 was not considered for any statistical calculation since only two efficient MODIS scenes are available within this year's ablation period. The

annual number of MODIS scenes range from 7 (2012) to 41 (2013). The annual standard deviation of the SLA ranges from 14 m (2011) to 73 m (2013), its average is 45 m. The interannual standard deviation of the annual median SLA is 26 m. The annual median SLA ranges from 5488±85 m a.s.l. (2012) to 5600±85 m a.s.l. (2010). The highest position of the transient snow line at the end of the ablation period corresponds to the annual ELA proxy. It ranges from 5519±85 m a.s.l. (2011) to 5726±85 m a.s.l. (2010) and its multiannual average is 5618±85 m a.s.l. The difference between the multiannual ELA proxy between 2002 and 2014 (5618 m a.s.l.) and the annual ELA proxy points towards a positive or negative mass balance in the respective year (Fig. 6.7). Considering the derived multiannual ELA (2002-2014) the year 2010 suggests a negative mass balance with the uncertainty range fully above the multiannual ELA proxy while 2011 suggests a positive mass balances even though based on comparatively little data coverage. The result is fairly similar to the regional ELA approximation of Yao et al. (2012) stated as 5500 m a.s.l. for UM. Chen et al. (2014) found a mean firn line altitude at about 5610 m a.s.l. and a slight trend towards a higher firn line at the east facing Binglinchuan glacier. This agrees well with our results of a mean ELA of 5618 m a.s.l. The interannual variability of the firn line altitude is correlated with the ELA proxy of this study (2006 to 2013) (r=0.6).

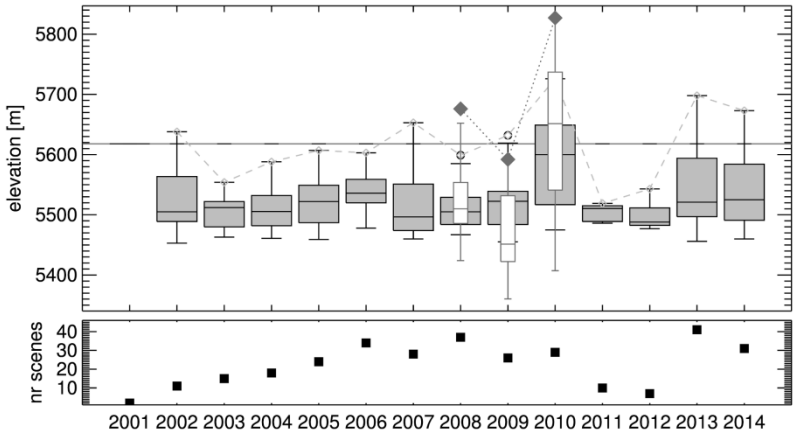

Fig. 6.7: Boxplot of interannual MODIS derived end of summer snow line altitudes of Ulugh Muztagh (UM) in grey and detail region (UMdetail) in white. The multiannual remote sensing ELA proxy (5618 m a.s.l.) is indicated as horizontal grey line. The annual ELA proxies are connected with dashed lines (top). The number of underlying scenes is given at the bottom.

6.5.1.2 UMdetail

Looking at the remote sensing study of the smaller UMdetail region a larger standard deviation is visible compared to the UM study region due to the higher natural variability of a reduced data basis and slightly different altitude distribution (Fig. 6.7, Fig. 6.1 D). The progression of SLAs in UM and UMdetail correlates highly significantly (r= 0.65 after Spearman). The interannual variability of the derived ELA proxy differs between both regions since SLAs in 2009 lie generally lower in UMdetail than in the entire UM. Results for the detail region UMdetail can be seen as transferable for the greater region.

The progression of the remote sensing derived SLAs in UMdetail for the observation period is shown in Fig. 6.8 as grey diamonds. The annual maximum SLA in the observation period appears in the first half of August in all three years and SLAs generally descend afterwards until September (Fig. 6.8). In year 2008 the progression is not totally clear within the observation period since SLAs at the

beginning of September again increase (Fig. 6.8). The altitude differences of SLAs in 2008 account for 252 m (15% of the total altitude range) (Table 6.4). Less marked altitude differences of 232 m are seen in 2009. Here only three MODIS scenes are available before the end of August due to high cloud coverage. In the second half of September 2009 very low SLAs occur with a mean of 5425 m a.s.l. Within the ablation period in 2010 the SLAs follow the expected progression with a pronounced increase at the beginning of the ablation period and a clear decrease at the end of the period. Respectively, the range of the SLA is largest in 2010 with 420 m altitude difference. The highest SLA in the three ablation periods are 5676±110 m a.s.l. (2008), 5592±110 m a.s.l. (2009) and 5827±110 m a.s.l. (2010) (Table 6.4).

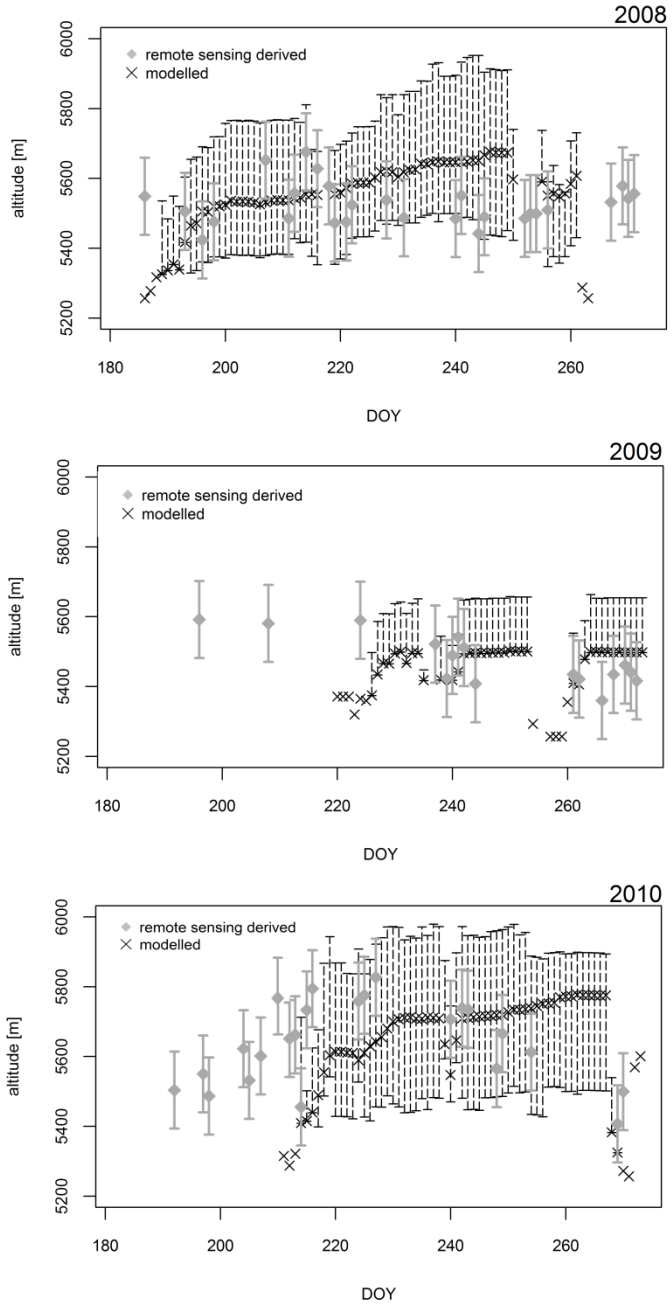

Fig. 6.8: Snow line altitudes (SLA) of the detail region (UMdetail) within 01 July to 30 September in 2008 to 2010. Mean daily MODIS derived SLA as grey diamonds, modelled SLA as black crosses. Error bars are explained in the text.

Table 6.4: Results of remote sensing approach and modelling approach within the observation period (01 July – 30 September): Mass balance (MB), highest transient snow line in study period (max SLA), mean SLA based on temporal congruent scenes of both methods (mean SLA), difference between highest and lowest modelled SLA in study period (max SLA – min SLA), standard deviation of modelled SLA in study period (std). Comparison between both methods on the right: Difference between remote sensing derived maximum SLA and modelled maximum SLA (\max SLA), difference between remote sensing derived mean SLA and modelled mean SLA (\mean SLA), root mean square error (RMSE), correlation coefficient after spearman (r) and p-value (p) of SLA (based on temporal coinciding scenes).

	Reso-lution	Model period	Year	MB [m w.e.]	max SLA [m]	mean SLA [m]	max SLA – min SLA [m]	std [m]	\max SLA [m]	\mean SLA [m]	RMSE [m]	r	p
Remote sensing	250	–	2008	–	5676	5523	252	60					
			2009		5592	5459	232	72					
			2010		5827	5662	420	120					
Model	250	2005 - 2010	2008	-0.62	5676	5554	419	107	0	-32			
			2009	-0.24	5502	5461	244	75	90	9	153	0.29	0.045
			2010	-0.71	5777	5529	520	146	50	201			
	1000	2006 - 2010	2008	-0.46	5750	5563	477	100	-74	-42			
			2009	-0.08	5558	5468	119	39	34	-18	140	0.47	0.0018
			2010	-0.54	5825	5562	552	132	1	113			

6.5.2 Results of Modelling approach

6.5.2.1 Uncertainty of precipitation input

The original mean annual HAR temperature and precipitation accounts for -11°C and 668 mm y^{-1}. Wang et al. (2009) quote a mean annual precipitation in the Kunlun Shan of 20-300 mm. Yasuda and Furuya (2012) estimated annual precipitation near the snow line on the northern slopes of Western Kunlun Shan to be about 460 mm. About 200 mm annual precipitation at median altitude at UM was found by Rupper and Roe (2008) based on NCEP NCAR data. Böhner (2006) displayed a July precipitation of about 100 mm using statistical downscaling of GCM outputs. Gerlitz et al. (2015) estimated about 300 to 400 mm y^{-1} using an artificial neural network downscaling approach based on ERA-Interim data. The same amount was found by Sakai et al. (2015) at the modelled ELA height of UM. Guo et al. (2013) stated average annual temperature and precipitation of 10.4°C and 22.3 mm (11.7 and 24.6 mm) at two weather stations in the Tarim basin 240 km (300 km) from UM between 1954 and 2004. The final PSF used in this study implies an annual precipitation of 334 mm y^{-1}.

6.5.2.2 Comparison between different spatially resolved runs

In general the statistics of the final run with a spatial resolution of 250 m differ from the ones of the calibration run with the same parameter combination and a spatial resolution of 1000 m (Table 6.4). The more precise altitude reproduction of the higher resolution results in a higher standard deviation of the SLA. The absolute values of mean and maximum SLA are slightly lower. The coherence between final modelled and remote sensing derived SLA degrades slightly compared to the calibration run (Table 6.4). SLA derivation based on a different resolved DEM results in a lower

correlation and larger RMSE. This indicates that calibration of COSIMA on a lower resolution DEM is only provisory reasonable.

Annual MB of the final run show the same interannual variability as annual MB of the corresponding calibration run with a lower spatial resolution, however the absolute values are about 200 mm w.e. lower (Table 6.4). For the calibration run we allowed only one year spin-up time. To exclude reason in spin-up time for MB difference the corresponding calibration run was implemented one more time with two years spin-up time as used in the final run. The resulting MB is with up to 30 mm w.e. slightly less negative than in the run with one year spin-up time. Thus different spin-up time does not explain the MB mismatch between different spatially resolved runs.

Areas with lowest albedo, highest surface melt, subsurface melt and sublimation largely coincide on the glaciers (Fig. 6.9). These areas match areas of highest SW_{net} and most negative MB. They mainly consist of the south facing flanks of the two north-east facing glaciers and to a less extent of the glacier front of the convex formed south facing glacier (Fig. 6.9). The former flanks of the concave formed glacier surface are accompanied by crevasses. The regional accumulation seems to be decreased at wind shielded south facing slopes as detectable in Landsat scenes. These comparatively narrow (<500 m wide) areas of highest SW_{net} and most negative MB are not represented well within the lower resolution resulting in more negative MB within the higher resolution modelled data.

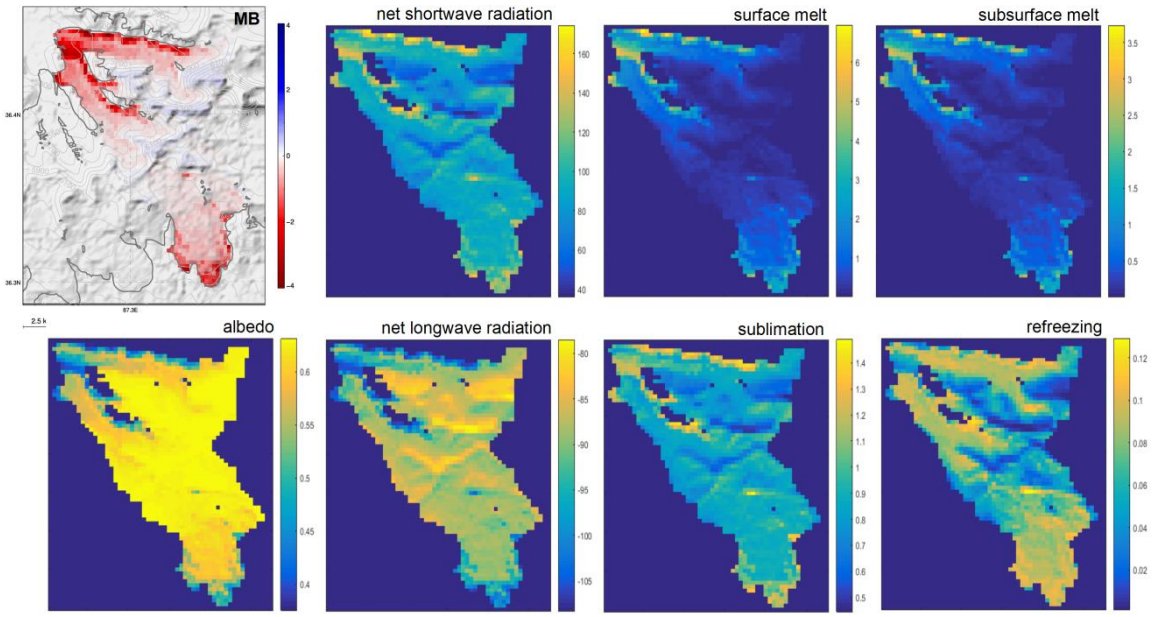

Fig. 6.9: Modelled annual mean mass balance (MB) and daily mean distribution of different parameter on UMdetail for the modelling period (01 October 2007 to 30 September 2010). Albedo, net shortwave radiation [W m^{-2}], net longwave radiation [W m^{-2}], surface melt [mm w.e.], sublimation [mm w.e.], subsurface melt [mm w.e.], refreezing [mm w.e.].

6.5.2.3 Comparison between runs with different parameter combinations

A second model run on a DEM with a resolution of 250 m has been carried out to examine the impact of different parameter combinations. The parameters were PSF 0.5/ATO +0.5°C for the first run and PSF 0.55/ATO +2.0°C for the second run. The correlation of resulting SLAs of both model runs is highly significant (r=0.89, RMSE=44 m). Apparent is a minor earlier occurrence of SLAs within the second model run (3 days earlier in 2010 and 10 days earlier in 2009) when higher air temperature

within the second run reaches the melting point earlier at the end of July. In 2009 the second model run produces SLAs about 60 m lower in average, in 2010 about 30 m lower. These results might be an indication for minor temperature sensitivity of UMdetail in the observation period. The application of the different combinations of PSF and ATO result in very similar progression of SLAs in absolute elevation and time. Since the increase of both parameters can interact and their influences regarding the snow line can cancel each other out this is not unexpected. In this study the consideration of the second model run would not change the interpretation and conclusion regarding the comparison with remote sensing derived SLA.

6.5.2.4 Daily SLA

Modelled daily SLAs for the observation period is shown in Fig. 6.8 as black crosses. The partially absence of error bars of the modelled SLA does imply no determination of uncertainty whenever the corresponding calibration run with a lower resolution returns undefined snow lines. In 2008 a snow line occurs in the beginning of July, it rises fast for the first twelve days (5260 to 5520 m a.s.l.) and then rises steadily until the beginning of September. In the second half of September the snow line declines suddenly in a nonlinear way, presumably due to snowfall, to 5260 m a.s.l. After 20 September the glaciers are again fully snow covered. In 2009 first snow lines appear on the glaciers late in the beginning of August and basically describe three short periods when SLA stays around 5500 m a.s.l. In mid-September a temporary drop of the SLA occurs down to 5260 m a.s.l. from where it quickly rearises to 5500 m a.s.l. within four days. At the end of July 2010 the first modelled snow lines are defined. Within the first ten days they rise quickly to 5600 m a.s.l. and then rise steadily until the end of September with only one small temporary drop of more than 100 m at the end of August. The highest modelled SLA in the ablation periods are 5676±238 m a.s.l. (2008), 5502±156 m a.s.l. (2009) and 5777±285 m a.s.l. (2010). The differences between highest and lowest SLA, as well as the standard deviations, are highest in 2010 and lowest in 2009 (Table 6.4).

6.5.2.5 MB and SEB

Mean monthly MB and SEB components for the observation period are illustrated in Fig. 6.10. The following interpretation of these results is kept superficial owed to the scope of the study.

The energy input is dominated by SW_{in} (+223 W m^{-2}) and LW_{in} (+150 W m^{-2}). Energy input due to Q_{sens} is low (+3.5 W m^{-2}) in the general cold environment. Between January and April Q_{sens} is very close to zero. Exceptional cold air temperatures in March 2009 even result in negative Q_{sens} values (Fig. 6.10). LW_{out} (-248 W m^{-2}), SW_{out} (-119 W m^{-2}), Q_{lat} (-34 W m^{-2}) and Q_{melt} (-6.4 W m^{-2}) are energy sinks at the glacier surface. Energy source is SW_{net} (+104 W m^{-2}). From October to January the radiation balance (R_{net}) is negative due to small water vapour pressure, decreased cloud cover and low air temperature. In March to May albedo and cloudiness increase hence R_{net} becomes positive with less negative LW_{net}.

In the modelling period surface melt accounts for 44% of region-wide mass loss (-430 kg m^{-2} a^{-1}). With air temperatures far below freezing point surface melt occurs from March onwards due to high insolation. Sublimation clearly dominates the mass loss from October to March. Over the modelling period sublimation accounts for 33% of mass loss (-330 kg m^{-2} a^{-1}). With 22% of the overall mass loss the subsurface melt is also an important factor (-216 kg m^{-2} a^{-1}). In the months June to September the subsurface melt amounts to about one third of the total melt. Solid precipitation (+402 kg m^{-2} a^{-1}) constitutes most of the mass gain of the glaciers. A strong annual snowfall cycle is apparent with very

low amounts in winter and peak accumulation in late spring to early summer. Refreezing acts as minor mass gain with +25 kg m^{-2} a^{-1}. It solely occurs in the summer months when surface melt occurs at higher altitudes on the glaciers (Fig. 6.9). Meltwater from the surface percolates and refreezes in areas where the snow layer is still below melting point.

The resulting annual MB of all three years is negative (Table 6.4). The monthly MB stays negative throughout the years except for June to July in 2009 when mass loss does not occur due to absent melt and for June 2010 when comparatively high amounts of snow add to the mass gain (Fig. 6.10). The winter MB is dominated by sublimation while melt is the determining factor in summer. The mean regional MB of UM accounts for -523±410 mm w.e. a^{-1} in the modelling period. Kääb et al. (2012) found a surface height change of +0.05±0.07 m a^{-1} for the Western Kunlun Shan between 2003 and 2008 which agreed very well with the rate given by Neckel et al. (2014) between 2003 and 2009 (+0.03±0.25 m a^{-1}). The latter found an even more positive MB rate of +370±250 mm w.e. a^{-1} for the region Zangser Kangri and Songzhi peak, about 250 km south-west of UM. For the entire region Eastern Kunlun Shan and Qilian Mountains they stated a MB rate of -770±150 mm w.e. a^{-1}. Gardner et al. (2013) stated locally MB rates of about +300 mm w.e. a^{-1} , about 200 km east of UM, and -300 mm w.e. a^{-1}, about 200 km west of UM, between 2003 and 2009. Overall our MB estimate is in agreement with the transitional location of UM between positive (in Western Kunlun Shan) and negative glacier MB (Eastern Kunlun Shan, Qilian Shan) shown in the studies of Gardner et al. (2013), Neckel et al. (2014) and Kääb et al. (2015) based on IceSat data. The concluded mass loss for UMdetail is in general agreement with Shangguan et al. (2009) who showed an area decrease for the glaciers in the basin of Qarqan river, which has its source at the north slope of UM, of -3.4% of their total area during 1977–2001 using the Chinese Glacier Inventory and Landsat images. Furthermore, Cui et al. (2013) also concluded a local mass loss at UM between 1977 and 2001 based on Landsat images. The regional mass loss of -523±410 mm w.e. a^{-1} derived in this study between 2008 and 2010 is even more negative than the value stated by Gardner et al. (2013) for a glacierized region 200 km farther east. This might be explainable by the extraordinary strong ablation in 2010 or might hint towards the fact that glaciers in the Qilian Shan seem to lose more mass than in the Eastern Kunlun Shan.

6.5.2.6 AAR

Comparison of the accumulation area ratio (AAR) averaged over a number of recent years with the AAR of an glacier in equilibrium state with a mass balance of zero (AAR_0) can indicate the current state of a glacier (Dyurgerov et al. 2009; Cogley et al. 2011; Huintjes et al. 2015b). The annual AAR at UMdetail is linearly correlated with the annual MB (Fig. 6.11).

The averaged AAR of the modelling period derived from the model output is 35%, the AAR_0 is estimated to be 76% (Fig. 6.11). The index after Dyurgerov et al. (2009) indicates the delay in the dynamic response of the glacier area relative to the climatic response of the accumulation area (i = (AAR-AAR0)/AAR0). At UMdetail it accounts for 54%, suggesting a retreat by 64 km² towards the equilibrium state under climate condition of the COSIMA simulation.

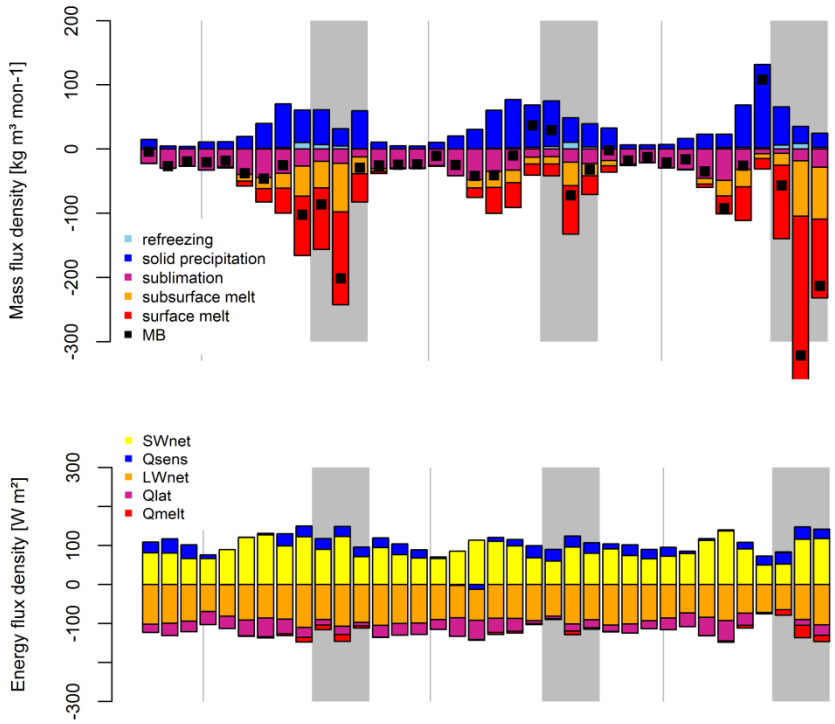

Fig. 6.10: Modelled monthly mean surface energy balance (SEB) and mass balance (MB) components for the modelling period (01 October 2007 to 30 September 2010).

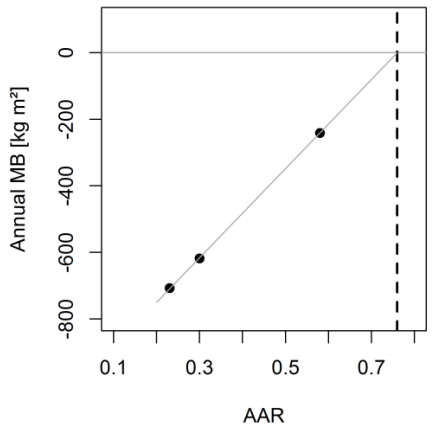

Fig. 6.11: Annual accumulation area ratio (AAR) and annual mass balance for the modelling period (01 October 2007 to 30 September 2010).

6.5.3 Method Comparison

Interannual variability of the maximum and mean SLA of both methods agrees well identifying 2009 as a year with low and 2010 with remarkably high snow lines (Table 6.4, Fig. 6.8). The generally pronounced snow cover in 2009 limits the analysis of SLA within the remote sensing approach since it decreases the number of days with identifiable SLA due to cloud coverage.

Modelled SLAs rise later and tend to stay lower than the remote sensing derived SLAs for the first half of the observation period while increase for a longer period before decreasing again (Fig. 6.8). The differences in progression of SLAs in both methods might be interpreted as a shift in time and

altitude. These shifts might be alterable by adjusting the input data to regional conditions. However the shifts are not conclusive for all three years to an equal degree and the application of a higher ATO alone does not result in a significant shift towards SLA earlier in the year (cf. Fig. 6.6).

Within observation period 67 remote sensing derived SLAs are defined (Fig. 6.7). The dates with coinciding availability of SLA from both methods is reduced to 47 days due to the fact that on days with either fully snow coverage on the glaciers or completely snow free glacier surfaces no modelled snow line is defined. The correlation of SLA of both methods is shown in Fig. 6.12. The positive correlation after Spearman is barely significant with a p-value of 0.045. Temporally agreeing SLA pairs combining modelled SLA below 5500 m a.s.l. and remote sensing derived SLA above 5600 m a.s.l. occur right at the beginning in 2009 and 2010. Excluding them would result in a significant correlation after Spearman with r=0.54. Reproduction of spatially distributed snow cover by the model shows good accordance with the remote sensing derived snow classification on a daily basis (Fig. 6.13, right). Nevertheless this result is not consistent for all scenes. In scenes of weak coherence of snow cover, usually occurring earlier in the observation period, the discrepancy occurs especially on the north-east oriented glacier tongues (Fig. 6.13, left) where highest uncertainty of the remote sensing approach might be assumed.

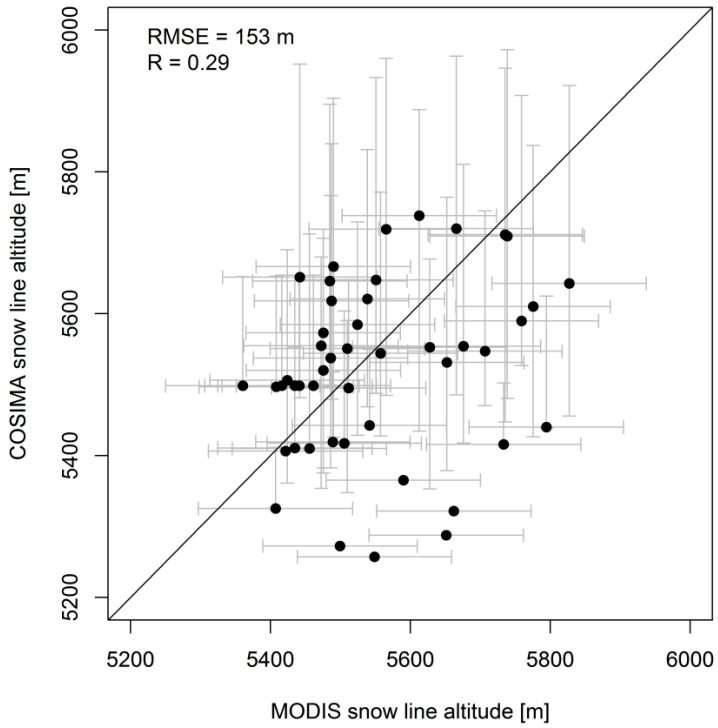

Fig. 6.12: Modelled and remote sensing derived SLA in the observation period in 2008 to 2010. The uncertainty ranges correspond to the standard deviation of remote sensing derived SLA and varied PSF (±0.5) and ATO (±0.5°C) in calibration runs (see explanation in the text).

Averaged over the years 2001 to 2014 PDD appear from mid-June to mid-September and the air temperature peaks in August while the precipitation gradually decreases from July to September. The annual progression of air temperature and precipitation in 2008 to 2010 is shown in Fig. 6.3.

In 2008 a high amount of SLAs of both methods lie in each other's error range. While the remote sensing derived SLA decrease since the beginning of August modelled SLA carry on rising until end of

August (Fig. 6.8). Solid precipitation declines until August 2008 while in September a second peak of snowfall occurs within the observation period (Fig. 6.3, Fig. 6.10). The year 2008 counts 21 PDD from mid-June to mid-August. In September 2008 daily mean air temperature stays below zero.

In 2009 simultaneous daily SLAs of both methods are scarce. All SLAs do not exceed 5500 m a.s.l. after beginning of August. An altitude drop of modelled SLA takes place in mid-September accompanied by a gap of remote sensing data presumably due to a snowfall event (Fig. 6.8). In 2009 the amount of annual PDD is below-average. A number of 15 PDD occur from the end of June to the beginning of September. But the absolute temperature is still quite low with an average PDD air temperature of 0.6°C. The solid precipitation peaks comparatively early in May (Fig. 6.3). This is in accordance with little MODIS data coverage due to cloud cover. In June to July the MB is positive. Glacier melt is lower probably due low air temperatures and high albedo of fresh snow protecting the glacier along the ablation period and influencing the annual MB (cf. Mölg et al. 2013).

In 2010 a similar pattern of SLA of both approaches is visible as in 2008. While the modelled SLA continue increasing the remote sensing derived SLA start to decline at the end of August (Fig. 6.8). In 2010 the pronounced peak of precipitation is precedent to the distinct air temperature peak (Fig. 6.3). In 2010 high amounts of 41 PDD occur comparatively late at the beginning of July until mid-September. Apart from the PDD amount absolute air temperatures are the highest within the period 2001 to 2014. The average PDD air temperature at an altitude of 5690 m a.s.l. is above +2°C with an absolute maximum of above +6°C. The resulting strong surface and subsurface melt cannot be compensated by snowfall.

Overall, the modelled SLAs progress in accordance with the picture drawn by HAR air temperature and precipitation input data. The occasionally mismatch in time and altitude of the observational remote sensing data thus hints towards a bias within the forcing data, even though orography and extreme events were well tested (Maussion et al. 2014a). Conceivable is a seasonal bias within the precipitation data that does not account for convective precipitation in autumn. Furthermore relocation processes and snow drift is not considered within COSIMA which might be an explanation approach for the difference in daily distributed snow cover on the glaciers. Since used parameter combination of PSF and ATO result in similar SLA progression in time (Fig. 6.6) the course in time of the climate data but not their absolute values can be used to reason the resulting SLA.

Following the same approach as in earlier studies (Shea et al. 2013; Brun et al. 2015; Spieß et al. 2015; Spieß et al. 2016a) the highest SLA at the end of the ablation period can be taken as a proxy for the annual ELA giving an indication towards the MB of the glacier (Cogley et al. 2011). The observation period of 1 July to 30 September is chosen correctly at UM in this context since accumulation season does not coincide with time of strongest ablation. Furthermore the minimum summer-albedo is found in mid-August in 2008 to 2010 based on COSIMA output data.

The discrepancies between modelled and remote sensing derived maximum SLA within the observation period lie within the error range but they do not coincide temporarily (Fig. 6.8). The interannual ELA variability of both methods is consequently consistent (Table 6.4). The straightforward approach to derive the ELA from the modelled annual MB as the altitude separating annual averaged accumulation and ablation area was conducted as well. Expectably the interannual variability is the same as for the other ELA proxies. Nevertheless the ELA derived from the modelled annual MB is in average located 270 m higher than the ELA proxy based on the SLA at the end of the ablation period. This distinct difference reveals that the commonly used ELA approximation as the highest position of the transient snow line at the end of ablation period is only reasonable when the

study period is characterized by a positive winter MB. At UM the strongly arid climate favours high sublimation amounts and very little snowfall during winter shaping the annual mass loss without being detectable in the SLA in the observation period.

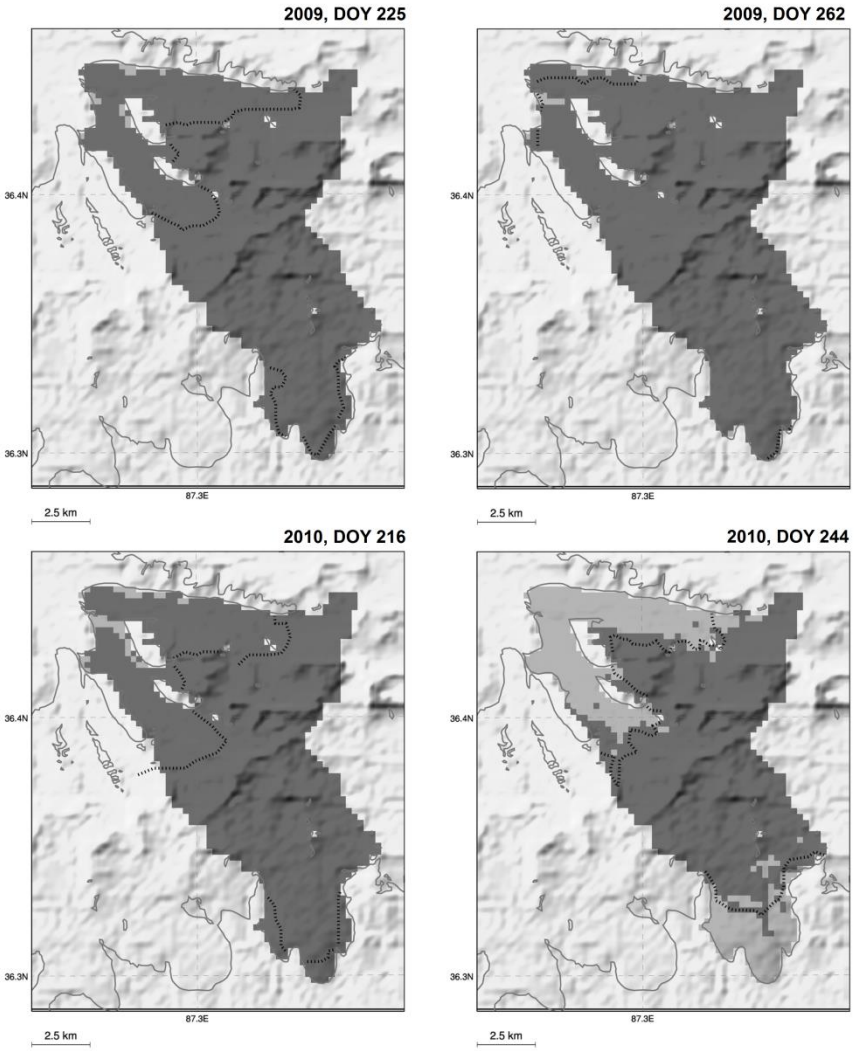

Fig. 6.13: Examples on spatial distribution of daily remote sensing derived and modelled snow line. Scenes with low congruence (left) and good agreement of both methods (right). Modelled snow cover (dark grey) and snow free glacier area (light grey) with remote sensing derived snow line (black dotted line).

6.6 Conclusions

Cluster analyses of MOD02QKM visible and near-infrared imagery were used to generate daily transient snow lines within the end of ablation period (01 July to 30 September) for the ice cap Ulugh Muztagh on the northern central TP. Method improvements in spatial representation and quality have been made compared to earlier studies (Spieß et al. 2015; Spieß et al. 2016a).

Modelled MB and SEB components as well as mean altitude of transient snow line were derived using COSIMA model for a representative detail region within the ice cap. The model was purely forced by high-resolution atmospheric model data with a spatial resolution of 250 m. The model was

calibrated using the remote sensing derived SLA. The input data was adjusted to reproduce the progression and specific statistic values of the SLA.

The resulting SLAs of both methods coincide in their interannual variability. Daily SLAs agree not consistently in time and elevation.

Application of different adjustment-parameter combinations on the model input data does result in similar progression and elevation of modelled SLAs. Even though monthly HAR data seems to be free of systematically error and is orographically well presented (Maussion et al. 2014a) unsurprisingly the application on a daily basis might be biased because of difficulties in capturing orographic convective precipitation events. COSIMA is proved to be very accurate on a monthly and annual basis even forced by non-in situ data. Nevertheless the usage of HAR forced COSIMA might be limited feasible for analysis on a daily basis. Snow drift and relocation processes of snow on the glacier surface are not integrated in COSIMA, but can be defining factors influencing the snow cover in a pronounced cold and arid climate.

The climatic interannual variability is clearly seen within the variability of SLA in both methods. 2009 is distinguished by very low air temperatures and an early peak of the precipitation in May. In 2010 extraordinarily high air temperatures occur and pronounced peaks in precipitation and temperature occur consecutively. The ELA proxy mirrors a clearly negative MB in 2010 whereas 2009 is characterized by a small amount of sparsely elevated SLAs. An early peak in snowfall seems to favour prevalent snow cover at UM and distinguished offset peaks in precipitation and air temperature seem to foster prevailing melt.

The interannual variability of ELA proxies of both methods coincide. Comparing ELA derived from the highest SLA at the end of ablation period with ELA derived from the modelled annual MB reveals a mismatch due to negative winter MB not regarded in the former ELA estimation.

The study reveals moderate negative MB for three glaciers of UM throughout the modelling period. The mean MB of the chosen detail region of UM accounts for -523±410 mm w.e. a^{-1} in the modelling period. Hence UM seems not to belong to the area of the 'Karakorum anomaly' which has its centre presumably in the Western Kunlun Shan. Sublimation is responsible for significant mass loss and negative MB during winter when precipitation amounts are small. Despite low air temperature surface melt starts in March due to high insolation.

The remote sensing approach using freely available satellite data is useful to support MB model calibration in regions without any observation data. Nevertheless resilient analysis on a daily basis is only promising with some basic meteorological data of the study site to narrow down actual climatic conditions. Since the snow cover pattern could not be consistently and precisely enough reproduced by the modelling approach it is recommended to rather combine the methods only on glaciers with glacier tongues of several kilometres width. The results of our study are difficult to compare with other studies because (1) no glaciological studies have been conducted at UM (2) other studies state multiannual MB proxies rather than provide interannual variability of glacier MB. Within the error range our results fit into the bigger picture of spatially diverse glacier development on the TP and agree with sparse existing regional MB proxies for neighbouring study regions (Scherler et al. 2011; Gardner et al. 2013; Neckel et al. 2014; Kääb et al. 2015).

7 Synthesis

The initial idea, deduced from the project-focus on dynamical response of glaciers to climate change on the TP, was to provide observational glaciological datasets to cross validate the COSIMA model, which was developed in the RWTH Aachen University working group on Physical Geography and Climatology. The reason for the relevance of this approach is the lack of observational data along the targeted east-west transect across the TP. At Zhadang glacier a set of ablation stakes and a time-lapse camera system provided a spatial and temporal validation of the model (Huintjes et al. 2015a). Remote sensing data was supposed to compensate for field observations elsewhere. The resulting dataset should be used as validation data for the model, to improve the knowledge on the initial conditions of modelling or to fit the model. To fulfil those requirements the resulting data was needed to be of preferably high spatial and temporal resolution.

7.1 Development in the remote sensing method to derive SLA

Within the working progress of this thesis improvements of the remote sensing method to derive daily SLA from freely available remote sensing data could be achieved.

With the usage of MODIS snow product data, as conducted in chapter 4, the method can be readily applied to derive SLAs from regional glacierized areas on the TP. The easy access, high temporal resolution and thorough quality assessment (Hall et al. 2002) of the data is convenient. Nevertheless, the coarse spatial resolution of 500 m is a disadvantage. Since we look for SLA which appears mostly on the most narrow part of a glacier or ice cap - the glacier tongue - the use of MODIS snow product data is feasible for ice caps and broad glaciers of preferable more than 1000 m (2 pixels) width. The albedo threshold to distinguish between snow and ice, as outlined in chapter 4, is a major factor of uncertainty, since in reality this threshold can regionally vary depending on grain size and impurities of snow or ice (Dietz et al. 2012).

In chapter 5 a different data basis was used to derive SLA. The MODIS swath data was utilized in order to portray a higher spatial resolution of 250 m. The raw data supplies a theoretical temporal resolution of two scenes per day. The acquisition and the preprocessing were less intuitive and considerably more time consuming in developing and computation than the ready to use MODIS snow product (chapter 5.4). The quality assessment needed to be comprehensive within the method procedure. As opposed to the first approach potentially erroneous scenes needed to be excluded automatically. Instead of an albedo threshold a cluster analysis was used to distinquish between snow and ice.

In both approaches the mean regional SLA was determined whenever a minimum of 45% of the MODIS scene pixels was valid: The 13th percentile of the altitude of the snow covered area on the glacier was used as an estimate for the mean regional SLA.

In deriving the ELA the approaches in chapter 4 and 5 basically rely on the assumption that the highest SLA at the end of ablation period (cf. Fig. 4.9) can be used as an ELA proxy. In contrast to chapter 4 the derived SLA in chapter 5 was weighted with the underlying data coverage to reduce outliers due to unrepresentative coverage of classified pixels within the scene. Thus the ELA proxy was taken as the (second) highest SLA in (chapter 4) chapter 5.

The advancement in chapter 6 consists of stricter quality assessment of single scenes. Subsequent to the unsupervised cluster analysis the physical credibility was verified based on spectral characteristics of the reflectance. Furthermore, a secondary cloud filter was introduced in assuming that cloud covered pixels at higher altitude that are neighbouring snow covered pixels actually represent snow cover as well. In chapter 6 the research focus shifted from the interannual ELA proxy to the progression of the SLA within the ablation period. Consequently, the minimum data coverage threshold was significantly increased from 45% to 95% in order to derive single (daily) snow cover scenes which are qualitatively more reliable. However, the underlying number of scenes is reduced notably which increases the chance of missing those scenes that are displaying the highest SLA and thus may serve as the ELA proxy. In chapter 6 the remote sensing derived SLAs were used to fit the COSIMA model. In this regard a smaller detail region consisting of three glaciers is studied separately from the larger region of UM. The progression of SLAs of both regions correlate significantly ($r = 0.65$ after Spearman). The derivation of the SLA in the detail region (UMdetail) is done by manually digitizing the snow lines on the glacier tongues for the three-year-period selected for modelling with COSIMA in contrast to using a percentile of the snow covered area as in the other approaches. This procedure of manually digitizing snowlines was more elaborate, but it supplied results which are directly comparable to the model output. In the intended case of successfully fitting the model to reproduce the regional daily remote sensing derived SLA the model output can reveal daily distributed SEB and MB information of the glacierized area.

7.2 Overall conclusion

7.2.1 MB and ELA

The thesis aim to study a diverse set of ROIs across the TP was accomplished. The described methods were applied to a series of study sites across the plateau to look for spatial differences in interannual variability of the ELA proxy. For the majority of the study sites no other glaciological studies have been conducted so far.

Two different MODIS data sets were used to derive annual ELA proxies for PIC. Results show that the interannual variabilities are highly and significantly correlated. The cross validation shows that our method is robust and feasible for larger glacierized areas (Fig. 5.8).

The spatial pattern of average ELA proxy (2002-2012) for all study regions generally agree with the estimates of Yao et al. (2012). The ELA is lowest in the Pamir (Muztagh Ata at 5130 m a.s.l.; Table 5.1) with its winter precipitation regime dominated by westerlies. Average ELA on the TP is remarkably higher between 5600 and 6000 m a.s.l. On the southern TP along the east-west transect from Western Nyainqêntanglha via the Transhimalayas to Gurla Mandhata the ELA slightly increases from

east to west (Table 5.1). Towards the northern fringe of the plateau the multiannual ELA decreases slightly to 5620 m a.s.l. at UM (Table 6.4). The limitation of the time series length does not enable a trend analysis concerning the MB. A tendency towards a higher ELA / more negative MB is apparent at the Western Nyainqêntanglha range. This is in agreement with the MB of Zhadang glacier after Mölg et al. 2014 and Huintjes et al. 2015a. The peaks of most negative MB years in 2006 and 2009 agree as well with those studies (Fig. 4.4 and Fig. 5.9). The continuing mass loss is in agreement with the study results stating a pronounced mass loss of the temperate to polythermal glaciers influenced by the monsoon in the south-east of the TP (e.g. Kääb et al. 2012; Mölg et al. 2012; Yao et al. 2012; Gardelle et al. 2013; Gardner et al. 2013). At UMdetail on the northern plateau the modelled negative MB of -523±410 mm w.e. a^{-1} in 2008 to 2010 is in agreement with the transitional location of UM between positive (in Western Kunlun Shan) and negative glacier MB (Eastern Kunlun Shan, Qilian Shan) shown in the studies of Gardner et al. (2013), Neckel et al. (2014) and Kääb et al. (2015) based on IceSat data. UM seems not to belong to the area of the 'Karakorum anomaly' which has its centre presumably in the Western Kunlun Shan.

The results on interannual regional MB proxies of 12 years are difficult to compare with other studies because either (1) no glaciological studies have been conducted yet in the specific ROIs, (2) other studies state multiannual MB proxies rather than provide interannual variability of glacier MB or (3) glaciological studies based on in situ measurements have only been conducted on single glaciers rather than covering a whole region.

7.2.2 Interannual ELA variability

In comparing the interannual ELA variability across the plateau it becomes obvious that it is less pronounced for summer-accumulation type glaciers in contrast to the winter-spring-accumulation type glaciers at Muztagh Ata. Regional interannual ELA variability differs in form and strength often even between spatially close ROIs for example in the Transhimalaya (Table 5.3). This can be related to different reactions of the glaciers to climatic forcing (depending on its topographical and geomorphological features) and also the fact that the inter-annual variability of the climatic forcing factors is not uniform across the TP. Even ROIs spatially close to each other show strong differences in the inter-annual variability of temperature and precipitation (Fig. 5.7C). The standard deviation of the inter-annual temperature is higher in the winter months (highest at Muztagh Ata, Fig. 5.6) whereas the precipitation has a higher inter-annual variability in the summer months (Table 5.1). The higher interannual precipitation variability in central and western TP compared to other TP regions can be explained by interannual variability of the outreach of summer precipitation events (Maussion 2014b). Not only the amplitude of the variability but also its algebraic sign can vary in the same year across the TP. This confirms the essentially different climatic patterns due to large scale circulation and local factors.

The simplified approach of a correlation analysis to detect connections between the ELA and climatic predictors on a monthly basis (chapter 4.3.1 and 5.4.2) can indicate climate-related forcings of the ELA proxy variability in case of high and significant correlations. However, not only the inherent uncertainty of the ELA estimation has to be kept in mind but also the statistical limitations due to the shortness of the time series.

In very general terms summer air temperature is most important for the central and eastern parts of the Tibetan Plateau while winter precipitation has much relevance for glaciers in the west of the plateau. Spatially, a high correlation of the inter-annual ELA variability is present between Western Nyainqêntanglha and PIC (Table 5.3). For the mass balance of PIC, equal to Zhadang glacier in

Western Nyainqêntanglha range revealed by Mölg et al. (2014), June precipitation has been identified as a crucial factor. An early peak in snowfall before July seems to favour prevalent snow cover also at UM in the northern TP and distinguished offset peaks in precipitation and air temperature seem to foster prevailing melt (chapter 6.5).

At several study areas higher temperatures throughout winter and spring tend to raise the ELA (chapter 5.5). Sublimation is favoured by rising temperatures even during periods with temperatures below freezing point, especially under arid conditions.

Whereas increased westerly air flow in November enhances sublimation at PIC and Nyainqêntanglha, it is the driver of increased snowfall in the Pamirs leading to a contrasting regional pattern of ELA variability. Strong southerly flow in July is connected to higher temperatures and is correlated with an increased ELA. Only at Muztagh Ata and Surla this pattern is not visible. Direct influence of the monsoon indicated through the ISM is visible at NWN in July and Gurla Mandhata in August, even though other studies suggest the solitary influence of westerly windmasses in the western Himalaya range (Curio et al. 2015). However, monsoonal influence is also tracable through the DMI at Gurla Mandhata, Surla and Shankangsham between June and September. El Niño in spring (summer) is connected to a lower (higher) ELA at Muztagh Ata (Gurla Mandhata). While in February or March a positive phase of NAO is connected to higher wind speed and a lower ELA at PIC, SEN, Targo Gangri and Shankangsham, in April it is connected to lesser wind speed and a higher ELA at Surla.

7.2.3 Comparison between remote sensing and modelling approach

Modelled MB and SEB components as well as the mean altitude of transient snow line were derived using COSIMA model in chapter 6. The model was purely forced by high-resolution atmospheric model data and was calibrated using the remote sensing derived SLA. In the absence of in situ measurements the meteorological input data was adjusted to reproduce the progression and specific statistic values of the remote sensing derived SLA.

The resulting SLAs of remote sensing and modelling approach agree in their interannual variability whereas daily SLAs do not agree consistently in time and elevation. COSIMA is proved to be very accurate on a monthly and annual basis even forced by non-in situ data. The application of different adjustment-parameter combinations on the model input data does result in similar progression and elevation of modelled daily SLA which do not accurately reflect the daily progression in remote sensing derived SLA. Using glaciological and hydrological models driven solely by HAR data Huintjes et al. (2014), Mölg et al. (2014) and Biskop et al. (2013) could reproduce observed surface MB at Zhadang glacier and volume change at lake Nam Co. The usage of HAR forced COSIMA output appears to be limited feasible for analysis on a daily basis for several reasons: The application on a daily basis might be biased because of the difficulty in capturing orographic convective precipitation events in the HAR data and the missing consideration of snow drift and relocation processes of snow on the glacier surface within COSIMA.

The necessity of preferably high spatial resolution in MB studies was confirmed by comparing the model output of different spatial resolution. A more negative annual MB is apparent when running the model on a higher resolved DEM. Studying the spatial distribution of SEB components it becomes clear that areas with highest SW_{net} and most negative MB match with areas of coinciding lowest albedo, highest surface melt, subsurface melt and sublimation (Fig. 6.9). These areas mainly consist of the south facing flanks of the two north-east facing glaciers and to a lesser extent of the glacier front of the convex formed south facing glacier (Fig. 6.9). These comparatively narrow (<500 m wide)

areas of highest SW_{net} and most negative MB are not represented well within the lower resolution runs resulting in less negative MB within the low resolution model runs.

Another outcome is the observation that the commonly used ELA approximation as the highest position of the transient snow line at the end of ablation period is only reasonable in study regions characterized by a positive winter MB. At UMdetail the modelled ELA derived from the modelled annual MB is significantly higher than the remote sensing derive ELA proxy based on the SLA at the end of the ablation period since the negative winter MB (Fig. 6.10, Fig. 7.1) is not taken into account in the remote sensing approach. At UMdetail at the northern fringe of the TP the SEB modelling reveals sublimation responsible for significant mass loss and negative MB during winter when precipitation amounts are very small. Despite low air temperature surface melt starts in March due to high insolation.

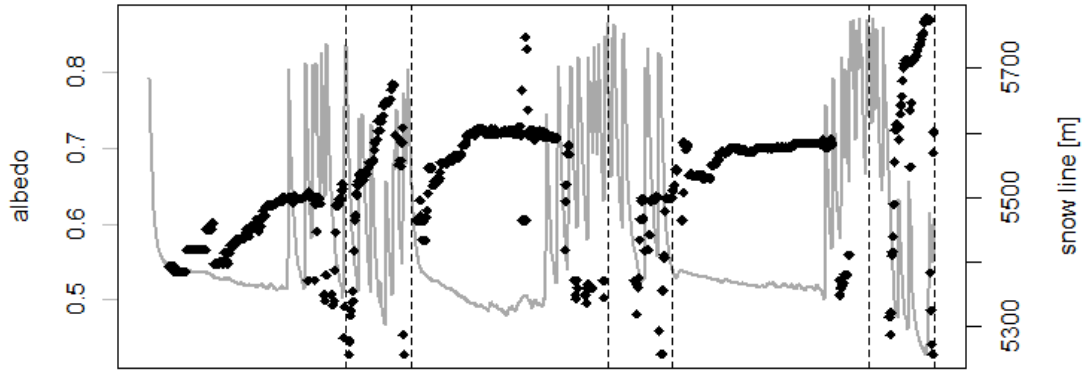

Fig. 7.1: Modelled daily mean albedo (grey) and modelled SLA (black) in the modelling period (01 October 2007 to 30 September 2010).

7.2.4 Uncertainties

Even though based on observational remote sensing data, the approaches implicate a couple of uncertainties, some of which can hardly be quantified. The most important uncertainties are once more summarized:

◆ To improve the accuracy of the resulting snow map the applied MODIS cloud mask tends to misclassify snow as clouds (Riggs and Hall 2002). Thorough applications of cloud filter address this uncertainty.

◆ Uncertainties in the validation with Landsat scenes are negligible considering the much coarser resolution of MODIS data (chapter 4.3).

◆ Superimposed ice is formed by refreezing of meltwater on the glacier surface. On the cold and polythermal glaciers on the TP superimposed ice is likely to exist (Fujita and Ageta 2000). Neglecting superimposed ice when deriving the ELA proxy using the end-of-ablation snow line in a negative MB year will lead to an overestimation of the ELA (Fig. 3.6).

◆ Important spatially differentiations in SEB are difficult to capture in a coarse resolution model run. Steps in altitudes within the DEM result in a less graduate progression of altitude reflected within the DEM and consequently within the derived SLAs.

◆ The optimal minimum data coverage in chapter 4 and 5 is estimated. The resilience of a mean SLA derived from different minimum amount of valid pixels was tested and the threshold is compared to others used in other studies (cf. Shea et al. 2013).

◆ The albedo threshold to distinguish between snow and ice is validated using two Landsat scenes which is not considered resilient but was limited due to the lack of suitable Landsat scenes.

◆ The same uncertainty is inherent for the evaluation of the fixed percentile used to derive the regional mean SLA since only three Landsat scenes could be used in chapter 4 and 5 for this purpose.

◆ The unsupervised k-means cluster analysis in chapter 5 and 6 minimises the Euclidean Distance between cluster means and its uncertainties are not quantified.

◆ The reflectance combination threshold to supervise the cluster analysis in chapter 6 is estimated averaging literature based information (Lopez et al. (2008); Dietz et al. (2011); Goetz et al. (2012)).

◆ The model uncertainty can hardly be quantified (Huintjes et al. 2015a). Uncertainties in the subsurface temperature, water content and snow density are addressed by including a model spin-up period of two years. Huintjes et al. (2015a) evaluated the results from COSIMA against multi-annual MB measurements using the glaciological method at Zhadang glacier. They determined a glacier-wide model uncertainty of ±600 kg m^{-2} yr^{-1}. We obtain a model uncertainty for SLA at UM of maximal ±340 m, accounting for precipitation- and temperature uncertainties.

◆ Model runs with the same parameter set that are only different in the allocated spin-up time result in different SLA (Fig. 7.2, Table 7.1). This indicates that improper spin-up times leas to additional modelling errors.

Table 7.1: Results of modelling approach within the observation period (01 July – 30 September): Mass balance (MB), highest transient snow line in study period (max SLA), mean SLA based on temporal congruent scenes of both methods (mean SLA), difference between highest and lowest modelled SLA in study period (max SLA – min SLA), standard deviation of modelled SLA in study period (std). Comparison with remote sensing approach on the right: Difference between remote sensing derived maximum SLA and modelled maximum SLA (\max SLA), difference between remote sensing derived mean SLA and modelled mean SLA (\mean SLA), root mean square error (RMSE), correlation coefficient after spearman (r) and p-value (p) of SLA (based on temporal coinciding scenes).

Res	model period	MB (m w.e.)	max SLA (m)	mean SLA (m)	max SLA – min SLA (m)	std	\max SLA (m)	\mean SLA (m)	RMSE (m)	r	p
1000	2006 - 2010	-0.46	5750	5563	477	100	-74	-42	140	0.47	0.0018
		-0.08	5558	5468	119	39	34	-18			
		-0.54	5825	5562	552	132	1	113			
1000	2005 - 2010	-0.45	5796	5540	453	109	-120	-19	152	0.37	0.028
		-0.05	5354	5354	0	0	239	75			
		-0.52	5725	5535	382	102	101	320			

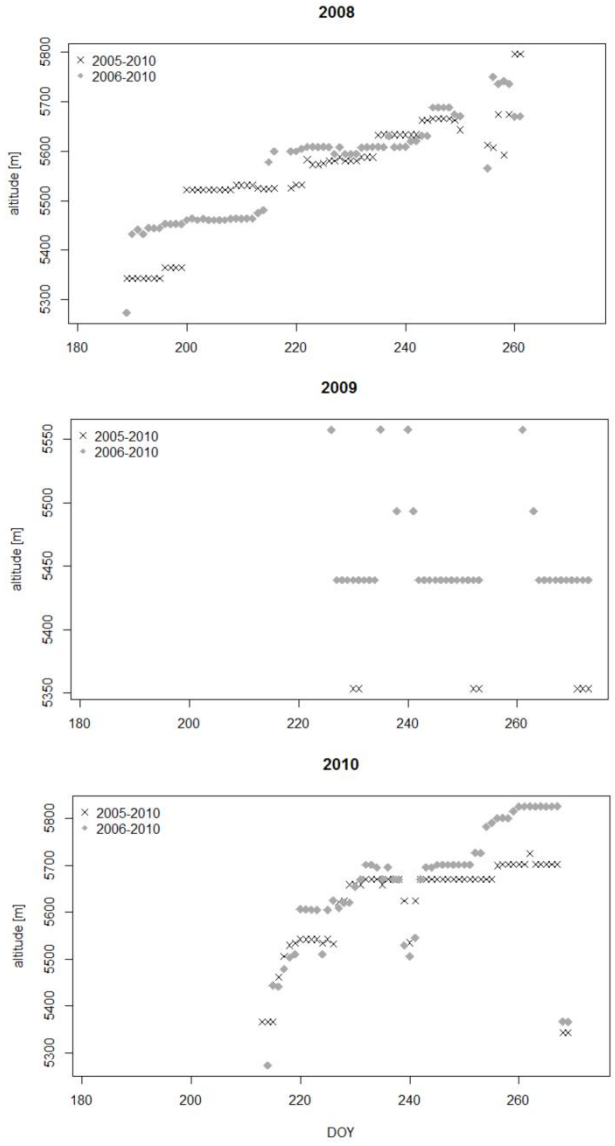

Fig. 7.2: Comparison of modelled SLA allowing different spin-up time of one year (2006-2010) and two years (2005-2010). Snow line altitudes (SLA) of the detail region (UMdetail) within 01 July to 30 September in 2008 to 2010.

7.3 Outlook

This thesis presents the development of a remote-sensing approach to derive snow lines from MODIS satellite data to estimate mass balance variability of glaciers on the Tibetan Plateau by means of the annual ELA. The method can be readily applied to construct time series of transient snow line altitudes with at best case daily resolution and regional annual ELAs on larger glacierized areas since 2002.

The focus of this thesis was the spatial variation of glacial variability thus we choose glacierized areas distributed across the plateau. These areas often did not offer any observational data to adjust the method to local climatic conditions. Field campains with further measurements of atmospheric and glaciological data would be highly beneficial for the application of the introduced method of this thesis as well as for a great number of other research activities concerning the TP.

As a desirable further research step the application of the method to areas which are already well studied concerning regional annual glacialogical parameters will anable to correct potentially excisting flaws and especially adapt the method to local climatic conditions. In consequence, since validation and comparison of our results with ground truth was the biggest deficiency, further adjustment might well improve the method in its reliability.

Meteorological ground truth data would give the opportunity to adjust the HAR input data. Usage of improved processing power would introduce the possibility to model a big glacierized area over a longer time period and to perform multiple runs with different parameter sets. The remote sensing methods produces best results for local mean ELA proxy on larger glacierized areas. The implementation of the method described in chapter 6 (Spieß et al. 2016b) to a study region with longterm meteorological measurements on the TP using superior processing power would improve the comparison between modelling and remote sensing approach.

An interesting applied research approach would be to focus on single hazardous snowfall events on the TP. The methods developed in this thesis can be used to derive a respective index of hazardous snowfall events. The spatial distribution and temporal occurance of hazardous snowfall events could be studied in connection with the influence on local glaciers and direct impact on human livelihood on the basis of MODIS data. This index could be used to validate meteorological model data, which in turn could improve COSIMA input data.

References

Arendt, A., Bolch, T., Cogley, J.G. et al. (2014) Randolph Glacier Inventory 4.0: A dataset of global glacier outlines. Global Land Ice Measurements from Space, U.S. National Snow and Ice Data Center, Boulder Colorado, USA. Digital Media.

Aschwanden, A. (2008) Mechanics and thermodynamics of polythermal glaciers, Dissertation, ETH Zürich, 93 pp.

Bao, W.J., Liu, S.Y., Wei, J.F. and Guo, W.Q. (2015) Glacier changes during the past 40 years in the West Kunlun Shan. Journal of Mountain Science, 12(2), 344-357. doi:10.1007/S11629-014-3220-0

Barnes, E.A. and Hartmann, D.L. (2010) Dynamical Feedbacks and the Persistence of the NAO. Journal of the Atmospheric Sciences, 67, 851–865. doi:10.1175/2009 JAS3193.1

Benn, D.I., Evans, D.J.A. (2010) Glaciers und Glaciation, 2nd ed. Hodder Education, London.

Bishop, M.P., Olsenholler, J.A., Shroder, J.F., Barry, R.G., Raup, B.H., Bush, A.B., Copland, L., Dwyer, J.L., Fountain, A.G., Haeberli, W., Kääb, A., Paul, F., Hall, D.K., Kargel, J.S., Molnoa, B.F., Trabant, D.C. and Wessels, R. (2004) Global Land Ice Measurements from Space (GLIMS): remote sensing and GIS investigations of the Earth's cryosphere. Geocarto International, 19(2), 57-84.

Biskop, S., Maussion, F., Krause, P. and Fink, M. (2015) What are the key drivers of regional differences in the water balance on the Tibetan Plateau? Hydrology and Earth System Sciences Discussions, 12, 4271-4314. doi:10.5194/hessd-12-4271-2015

Böhner, J. (2006) General climatic controls and topoclimatic variations in Central and High Asia. Boreas, 35(2), 279-295. doi:10.1080/03009480500456073

Bolch, T., Buchroithner, M.F., Peters, J., Baessler, M. and Bajracharya, S. (2008) Identification of glacier motion and potentially dangerous glacial lakes in the Mt. Everest region/Nepal using spaceborne imagery. Natural Hazards and Earth System Science, 8(6), 1329-1340.

Bolch, T., Yao, T., Kang, S., Buchroithner, M.F., Scherer, D., Maussion, F., Huintjes, E. and Schneider, C. (2010) A glacier inventory for the western Nyainqêntanglha Range and the Nam Co Basin, Tibet, and glacier changes 1976–2009. The Cryosphere, 4(3), 419-433. doi:10.5194/tc-4-419-2010

Bolch, T., Kulkarni, A., Kääb, A., Huggel, C., Paul, F., Cogley, J.G., Frey, H., Kargel, J.S., Fujita, K., Scheel, M., Bajracharya, S. and Stoffel, M. (2012) The state and fate of Himalayan glaciers. Science, 336(6079), 310-314. doi:10.1126/science.1215828

Boos, W.R. and Kuang, Z. (2010) Dominant control of the South Asian monsoon by orographic insulation versus plateau heating. Nature, 463, 218-U102. doi:10.1038/nature08707

Bothe, O., Fraedrich, K. and Zhu, X. (2010) The large-scale circulations and summer drought and wetness on the Tibetan plateau. International Journal of Climatology, 30(6), 844-855. doi: 10.1002/joc.1946

Bothe, O., Fraedrich, K. and Zhu, X. (2011) Large-scale circulations and Tibetan Plateau summer drought and wetness in a high-resolution climate model. International Journal of Climatology, 31(6), 832-846. doi:10.1002/joc.2124

Braithwaite, R.J. and Raper, S.C.B. (2010) Estimating equilibrium-line altitude (ELA) from glacier inventory data. Annals of Glaciology, 50(53), 127-132. doi:10.3189/172756410790595930

Brock, B. W., Willis, I. C. and Sharp, M. J. (2000) Measurement and parameterization of albedo variations at Haut Glacier d'Arolla, Switzerland. Journal of Glaciology, 46(155), 675-688.

Brun, F., Dumont, M., Wagnon, P., Berthier, E., Azam, M.F., Shea, J.M., Sirguey, P., Rabatel, A. and Ramanathan, A. (2015) Seasonal changes in surface albedo of Himalayan glaciers from MODIS data and links with the annual mass balance. The Cryosphere, 9(1), 341-355. doi:10.5194/tc-9-341-2015

Burchfield, B.C., Molnar, P., Zhao, Z., Liang, K., Wang, S. et al. (1989) Geology of the Ulugh Muztagh area, northern Tibet. Earth and Planetary Science Letters 94:57–70

Carsey, F. (1992) Remote sensing of ice and snow: review and status. International Journal of Remote Sensing, 13(1), 5-11. doi:10.1080/01431169208904021

Chang, D. (1981) The vegetation zonation of the Tibetan Plateau. Mountain Research and Development, 29-48.

Chen, A., Chen, W., Wu, H., Zhang, W. and Wu, Y. (2014) The variations of firn line altitude on the Binglinchuan Glacier, Ulugh Muztagh during 2000-2013. Journal of Glaciology and Geocryology, 36(5):1069-1078. doi:10.7522/j.issn.1000 0240.2014.0129 (In Chinese with English abstract)

Chen, B., Xu, X.D., Yang, S. and Zhang, W. (2012) On the origin and destination of atmospheric moisture and air mass over the Tibetan Plateau. Theoretical and Applied Climatology, 110, 423–435. doi:10.1007/s00704-012-0641y

Cheng, G. and Wu, T. (2007) Responses of permafrost to climate change and their environmental significance, Qinghai-Tibet Plateau. Journal of Geophysical Research: Earth Surface (2003–2012), 112(F2).doi:10.1029/2006JF000631

China 2010 census data released (2011, 29 Sep). China Data Center. Retrieved from: http://chinadatacenter.org

Choekyi, T. (2014) Rethinking Grassland Policies: The Case of Environmental Justice of Tibetan Nomads. Doctoral dissertation, Budapest. etd.ceu.hu

Cogley, J.G., Hock, R., Rasmussen, L.A., Arendt, A.A., Bauder, A., Braithwaite, R.J., Jansson, P., Kaser, G., Möller, M., Nicholson, L. and Zemp, M. (2011) Glossary of Glacier Mass Balance and Related Terms. IHP-VII Technical Documents in Hydrology No. 86, IACS Contribution No. 2, UNESCO-IHP, Paris. 114 pp.

Cui, X. and Graf, H.F. (2009) Recent land cover changes on the Tibetan Plateau: a review. Climatic Change, 94, 47-61. doi:0.1007/s10584-009-9556-8

Cui, Z.Y., and Zhou, W.M. (2013) Extracting Area Change of Glaciers in the Ulugh Muztagh Region Based on RS and GIS. Modern Surveying and Mapping, 4, 003.

Curio, J., Maussion, F. and Scherer, D. (2015) A 12-year high-resolution climatology of atmospheric water transport over the Tibetan Plateau. Earth System Dynamics, 6, 109-124. doi:10.5194/esd-6-109-2015

Dietz, A.J., Kuenzer, C., Gessner, U. and Dech, S. (2012) Remote sensing of snow–a review of available methods. International Journal of Remote Sensing, 33(13), 4094-4134. doi:10.1080/01431161.2011.640964

Ding, Y., Liu, S., Li, J. and Shangguan, D. (2006) The retreat of glaciers in response to recent climate warming in western China. Annals of Glaciology, 43(1), 97-105.

Domrös, M. and Peng. G. (1988) The Climate of China, Springer, 361 pp.

Dumont, M., Sirguey, P., Arnaud, Y. and Six, D. (2011) Monitoring spatial and temporal variations of surface albedo on Saint Sorlin Glacier (French Alps) using terrestrial photography. The Cryosphere, 5(3), 759-771. doi:10.5194/tc-5-759-2011

Dumont, M., Gardelle, J., Sirguey, P., Guillot, A., Six, D., Rabatel, A. and Arnaud, Y. (2012) Linking glacier annual mass balance and glacier albedo retrieved from MODIS data. The Cryosphere, 6(4), 2363-2398. doi:10.5194/tc-6-1527-2012

Dyurgerov, M., Meier, M.F., Bahr, D.B. (2009) A new index of glacier area change: a tool for glacier monitoring. Journal of Glaciology, 55(192), 710–716. doi:10.3189/002214309789471030

Fischer, A. M. (2005) State Growth and Social Exclusion in Tibet: Challenges of recent economic growth (No. 47). NIAS press.

Flanner, M.G. and Zender, C.S. (2005) Snowpack radiative heating: Influence on Tibetan Plateau climate. Geophysical research letters, 32(6). doi:10.1029/2004GL022076

Flohn, H. (1958) Beitrage zur Klimakunde von Hochasien. Erdkunde, 12(4), 294-308.

Fujita, K., Seko, K., Ageta, Y., Jianchen, P. and Tandong, Y. (1996) Superimposed ice in glacier mass balance on the Tibetan Plateau. Journal of Glaciology, 42(142), 454-460.

Fujita, K. and Ageta, Y. (2000) Effect of summer accumulation on glacier mass balance on the Tibetan Plateau revealed by mass-balance model. Journal of Glaciology, 46(153), 244-252.

Fujita, K., Ohta, T. and Ageta, Y. (2007) Characteristics and climate sensitivities of runoff from a cold-type glacier on the Tibetan Plateau. Hydrological Processes, 21, 21, 2882-2891.

Fujita, K. (2008a) Effect of precipitation seasonality on climatic sensitivity of glacier mass balance. Earth Planetary Science Letter, 276, 1-2, 14-19.

Fujita, K. (2008b) Influence of precipitation seasonality on glacier mass balance and its sensitivity to climate change. Annals of Glaciology, 48, 88-92.

Gao, Y., Cuo, L. and Zhang, Y. (2014) Changes in Moisture Flux over the Tibetan Plateau during 1979–2011 and Possible Mechanisms. Journal of Climate, 27, 1876–1893. doi:10.1175/JCLI-D-13-00321.1

Gardelle, J., Berthier, E. and Arnaud, Y. (2012) Impact of resolution and radar penetration on glacier elevation changes computed from DEM differencing. Journal of Glaciology, 58(208), 419-422.

Gardelle, J., Berthier, E., Arnaud, Y. and Kääb, A. (2013) Region-wide glacier mass balances over the Pamir-Karakoram-Himalaya during 1999-2011. The Cryosphere, 7(6), 1885-1886. doi:10.5194/tc-7-1263-2013

Gardner, A.S., Moholdt, G., Cogley, J.G., Wouters, B., Arendt, A.A., Wahr, J., Berthier, E., Hock, R., Pfeffer, W.T., Kaser, G., Ligtenberg, S.R.M., Bolch, T., Sharp, M.J., Hagen, J.O., van den Broeke, M.R. and Paul, F. (2013) A reconciled estimate of glacier contributions to sea level rise: 2003 to 2009, Science, 340, 852– 857, 2013. doi:10.1126/science.1226558

Gerlitz, L., Conrad, O. and Böhner, J. (2015) Large-scale atmospheric forcing and topographic modification of precipitation rates over High Asia-a neural-network-based approach. Earth System Dynamics, 6, 61-81. doi:10.5194/esd-6-61-2015

Goetz (2012) Quantifying Spectral Diversity within a MODIS Footprint – Goetz Recipient Research in the Himalayas.

Gruber, S. and Haeberli, W. (2007) Permafrost in steep bedrock slopes and its temperature-related destabilization following climate change. Journal of Geophysical Research: Earth Surface 112, F02S18. doi:10.1029/2006JF000547

Guo, W., Liu, S., Wei, J. and Bao, W. (2013) The 2008/09 surge of central Yulinchuan glacier, northern Tibetan Plateau, as monitored by remote sensing. Annals of Glaciology, 54(63), 299-310. doi:10.3189/2013AoG63A495

Hagg, W., Braun, L. N., Weber, M. and Becht, M. (2006) Runoff modelling in glacierized Central Asian catchments for present-day and future climate. Nordic Hydrology, (2), 93-105. doi:10.2166/nh.2006.001

Hall, D.K. and Martinec, J. (1985) Remote sensing of ice and snow. Chapman and Hall, New York.

Hall, D.K., Riggs, G.A. and Salomonson, V.V. (1995) Development of methods for mapping global snow cover using moderate resolution imaging spectroradiometer data. Remote sensing of Environment, 54(2), 127-140. doi:10.1016/0034-4257(95)00137-P

Hall, D.K., Riggs, G.A., Salomonson, V.V., DiGirolamo, N.E. and Bayr, K.J. (2002) MODIS snow-cover products. Remote sensing of Environment, 83(1), 181-194. doi:10.1016/S0034-4257(02)00095-0

Hall, D.K., Riggs, G.A. and Salomonson, V.V. (2006) updated daily. MODIS/Terra Snow Cover 5-min L2 Swath 500m V005, 01 July to 30 September, 2001 to 2012. Boulder, Colorado USA: National Snow and Ice Data Center. Digital media

Hall, D.K. and Riggs, G.A. (2007) Accuracy assessment of the MODIS snow products. Hydrological Processes, 21(12), 1534-1547. doi:10.1002/hyp.6715

Hall, D.K. (2012) Remote sensing of ice and snow. Springer Science & Business Media.

Hedin, S. (1909) Transhimalaya, 3 vols., Leipzig, 1909.

Hewitt, K. (2005) The Karakoram anomaly? Glacier expansion and the'elevation effect,'Karakoram Himalaya. Mountain Research and Development, 25(4), 332-340. doi:10.1659/0276-4741(2005)025[0332:TKAGEA]2.0.CO;2

Hock, R. (2005) Glacier melt: a review of processes and their modelling. Progress in physical geography, 29(3), 362-391. doi:10.1191/0309133305pp453ra

Höfer, H.V. (1879) Gletscher und Eiszeitstudien. Sitzungsberichte der Akademie der Wissenschaften Wien, math.-phys. Klasse I 79, 331–367.

Holzer, N., Vijay, S., Yao, T., Xu, B., Buchroithner, M. and Bolch, T. (2015) Four decades of glacier variations at Muztag Ata (Eastern Pamir): a multi-sensor study including Hexagon KH-9 and Pléiades data. The Cryosphere, 9(6), 2071-2088. doi:10.5194/tc-9-2071-2015

Hooke, R. L. (2005) Principles of glacier mechanics. Cambridge university press.

Hu, J., Li, Z., Li, J., Zhang, L., Ding, X., Zhu, J. and Sun, Q. (2014) 3-D movements mapping of the alpine glacier in Qinghai-Tibetan Plateau by integrating D-InSAR, MAI and Offset-Tracking: Case study of the Dongkemadi Glacier. Global and Planetary Change, 118, 62-68. doi:10.1016/j.gloplacha.2014.04.002.

Hubbard, B. and Glasser, N. (2005) Field techniques in glaciology and glacial geomorphology, Wiley, 400 pp.

Huintjes, E. (2014) Energy and mass balance modelling for glaciers on the Tibetan Plateau - Extension, validation and application of a coupled snow and energy balance model. -Doctoral dissertation, RWTH Aachen University. http://darwin.bth.rwth-aachen.de/opus3/volltexte/2014/5239/

Huintjes, E., Sauter, T., Schröter, B., Maussion, F., Yang, W., Kropacek, J., Buchroithner, M., Scherer, D., Kang, S. and Schneider, C. (2015a) Evaluation of a coupled snow and energy balance model for Zhadang glacier, Tibetan Plateau, using glaciological measurements and time-lapse photography. Arctic, Antarctic, and Alpine Research, 47 (3), 573–590. doi:10.1657/AAAR0014-073

Huintjes, E., Neckel, N., Hochschild, V. and Schneider, C. (2015b) Surface energy and mass balance at the Purogangri Ice Cap, central Tibetan Plateau, 2001-2011. Journal of Glaciology, doi:10.3189/2015JoG15J056

Huintjes, E., Loibl, D., Lehmkuhl, F. and Schneider, C. (2016) A modelling approach to reconstruct Little Ice Age climate from remote sensing glacier observations in southeastern Tibet. Annals of Glaciology, 57(71). doi:10.3189/2016AoG71A025

Hurrell, J. and National Center for Atmospheric Research Staff (Eds). (Last modified 08 Oct 2013) The Climate Data Guide: Hurrell North Atlantic Oscillation (NAO) Index (PC-based). Retrieved from https://climatedataguide.ucar.edu/climate-data/hurrell-north-atlantic-oscillation-nao-index-pc-based.

Immerzeel, W.W., van Beek, L.P.H. and Bierkens, M.F.P. (2010) Climate change will affect the Asian water towers. Science, 328, 1382–1385. doi:10.1126/science. 1183188

Jacob, T., Wahr, J., Pfeffer, W.T. and Swenson, S. (2012) Recent contributions of glaciers and ice caps to sea level rise. Nature, 482(7386), 514-518. doi:10.1038/nature10847

Kääb, A., Wessels, R., Haeberli, W., Huggel, C., Kargel, J.S. and Khalsa, S.J.S. (2003) Rapid ASTER imaging facilitates timely assessment of glacier hazards and disasters. EOS, Transactions American Geophysical Union, 84(13), 117-121.

Kääb, A., Huggel, C., Fischer, L., Guex, S., Paul, F. et al. (2005) Remote sensing of glacier-and permafrost-related hazards in high mountains: an overview. Natural Hazards and Earth System Science, 5(4), 527-554.

Kääb, A., Berthier, E., Nuth, C., Gardelle, J. and Arnaud, Y. (2012) Contrasting patterns of early twenty-first-century glacier mass change in the Himalayas. Nature, 488(7412), 495-498. doi:10.1038/nature 11324

Kääb, A., Treichler, D., Nuth, C. and Berthier, E. (2015) Brief Communication: Contending estimates of 2003–2008 glacier mass balance over the Pamir–Karakoram–Himalaya. The Cryosphere, 9(2), 557-564. doi:10.5194/tc-9-557-2015

Kalnay, E., Kanamitsu, M., Kistler, R., Collins, W., Deaven, D., Gandin, L., Iredell, M., Saha, S., White, G., Woollen, J., Zhu, Y., Chellah, M., Ebisuzaki, W., Higgins, W., Janowiak, J., Mo, K.C., Ropelewski, C. Wang, J., Leetmaa, A., Reynolds, R., Jenne, R. and Joseph, D. (1996) The NCEP/NCAR 40-year reanalysis project. Bulletin of the American meteorological Society, 77(3), 437-471.

Kang, S., Chen, F., Gao, T., Zhang, Y., Yang, W., Yu, W. and Yao, T. (2009) Early onset of rainy season suppresses glacier melt: a case study on Zhadang glacier, Tibetan Plateau. Journal of Glaciology, 55(192), 755-758.

Kang, S., Xu, Y., You, Q., Flügel, W.A., Pepin, N. and Yao, T. (2010) Review of climate and cryospheric change in the Tibetan Plateau. Environmental Research Letters, 5(1), 015101. doi:10.1088/1748-9326/5/1/015101

Kaser, G., Fountain, A. and Jansson, P. (2003) A manual for monitoring the mass balance of mountain glaciers, Technical Documents in Hydrology, 59, 137 pp.

Kaser, G., Großhauser, M. and Marzeion, B. (2010) Contribution potential of glaciers to water availability in different climate regimes. Proceedings of the National Academy of Sciences, 107(47), 20223-20227. doi:10.1073/pnas.1008162107

Klein, J. A., Harte, J. and Zhao, X. Q. (2004) Experimental warming causes large and rapid species loss, dampened by simulated grazing, on the Tibetan Plateau. Ecology Letters, 7(12), 1170-1179. doi:10.1111/j.1461-0248.2004.00677.x

Kornfeld, D., Eckert, S., Appel, E., Ratschbacher, L., Pfänder, J., Liu, D. and Ding, L. (2014) Clockwise rotation of the Baoshan Block due to southeastward tectonic escape of Tibetan crust since the Oligocene. Geophysical Journal International, ggu009. doi:10.1093/gji/ggu009

Kropáček, J., Braun, A., Kang, S., Feng, C., Ye, Q. and Hochschild, V. (2012) Analysis of lake level changes in Nam Co in central Tibet utilizing synergistic satellite altimetry and optical imagery. International Journal of Applied Earth Observation and Geoinformation, 17, 3-11. doi:10.1016/j.jag.2011.10.001

Kropáček, J., Neckel, N., Tyrna, B., Holzer, N., Hovden, A., Gourmelen, N., Schneider, C., Buchroithner, M. and Hochschild, V. (2015) Repeated glacial lake outburst flood threatening the oldest Buddhist monastery in north-western Nepal. Natural Hazards and Earth System Science, 15(10), 2425-2437. doi:10.5194/nhess-15-2425-2015

Kumar, L., Skidmore, A.K. and Knowles, E. (1997) Modelling topographic variation in solar radiation in a GIS envir-onment. International Journal of Geographical Information Science, 11, 5, 475-497. doi:10.1080/136588197242266

Lauer, W. and Bendix, J. (2004) Klimatologie, Westermann, 352 pp.

Leech, M.L., Singh, S., Jain, A.K., Klemperer, S.L. and Manickavasagam, R.M. (2005) The onset of India–Asia continental collision: early, steep subduction required by the timing of UHP metamorphism in the western Himalaya. Earth and Planetary Science Letters, 234(1), 83-97. doi:10.1016/j.epsl.2005.02.038

Lehmkuhl, F. and Haselein, F. (2000) Quaternary paleoenvironmental change on the Tibetan Plateau and ad-jacent areas (Western China and Western Mongolia), Quaternary International, 65/66, 121-145. doi:10.1016/S1040-6182(99)00040-3

Lei, Y., Yao, T., Yi, C., Wang, W., Sheng, Y., Li, J. and Joswiak, D. (2012) Glacier mass loss induced the rapid growth of Linggo Co on the central Tibetan Plateau. Journal of Glaciology, 58(207), 177-184. doi:10.3189/ 2012JoG11J025

Lemke, P., Ren, J., Alley, R.B., Allison, I., Carrasco, J., Flato, G., Fujii, Y., Kaser, G., Mote, P., Thomas, R.H. and Zhang, T. (2007) Observations: changes in snow, ice and frozen ground. In: Solomon, S., Qin, D., Manning, M., Chen, Z., Marquis, M., Averyt, K.B., Tignor, M., Miller, H.L. (Eds.), Climate Change 2007: The Physical Science Basis. Contribution of Working Group I to the Fourth Assessment Report of the Intergovernmental Panel on Climate Change. Cambridge University Press, Cambridge, UK.

Li, J., Yu, R. and Zhou, T. (2008) Teleconnection between NAO and climate downstream of the Tibetan Plateau. Journal of Climate, 21(18), 4680-4690. doi:10.1175/2008JCLI2053.1

Li, J., Wu, Z., Jiang, Z. and He, J. (2010) Can global warming strengthen the East Asian Summer Monsoon? Journal of Climate, 23, 6696–6705. doi:10.1175/2010JCLI3434.1

Li, J., Fang, X., Song, C., Pan, B., Ma, Y. and Yan, M. (2014) Late Miocene–Quaternary rapid stepwise uplift of the NE Tibetan Plateau and its effects on climatic and environmental changes. Quaternary Research, 81(3), 400-423. doi:10.1016/j.yqres.2014.01.002

Liu, S.Y., Shangguan, D.H., Ding, Y.J., Han, H.D., Zhang, Y., Wang, J., Xie, C.W., Ding, L.F. and Li, G. (2004) Variation of glaciers studied on the basis of remote sensing and GIS — a reassessment of the changes of the Xinqingfeng and Malan ice caps in the Northern Tibetan Plateau. Journal of Glaciology and Geocryology 26 (3), 244 – 252 (In Chinese).

Liu, J., Wang, S., Yu, S., Yang, D. and Zhang, L. (2009) Climate warming and growth of high-elevation inland lakes on the Tibetan Plateau. Global and Planetary Change, 67, 209–217, doi:10.1016/j.gloplacha.2009.03.010

Liu, L., Jiang, L. and Wang, H. (2012) Extraction of glacier surface elevation and velocity in high Asia with ERS-1/2 Tandem SAR data: Application to Puruogangri ice field, Tibetan Plateau. Geoscience and Remote Sensing Symposium (IGARSS), 2012 IEEE International (pp. 4442-4445).

Liu, X. and Chen, B. (2000) Climatic warming in the Tibetan Plateau during recent decades. International Journal of Climatology, 20, 1729-1742.

Liu, X. and Yin, Z.Y. (2001) Spatial and temporal variation of summer precipitation over the eastern Tibetan Plateau and the North Atlantic Oscillation. Journal of Climate, 14(13), 2896-2909.

Loibl, D., Lehmkuhl, F. and Grießinger, J. (2014) Reconstructing glacier retreat since the Little Ice Age in SE Tibet by glacier mapping and equilibrium line altitude calculation. Geomorphology, 214, 22-39. doi:10.1016/j.geomorph.2014.03.018

Lopez, P., Sirguey, P., Arnaud, Y., Pouyaud, B., & Chevallier, P. (2008) Snow cover monitoring in the Northern Patagonia Icefield using MODIS satellite images (2000–2006). Global and Planetary Change, 61(3), 103-116. doi:10.1016/j.gloplacha.2007.07.005

Louis, H. (1955) Schneegrenze und Schneegrenzbestimmung. Geographisches Taschenbuch 55, 414–418.

Ma, D., Boos, W. and Kuang, Z. (2014) Effects of orography and surface heat fluxes on the south Asian summer monsoon. Journal of Climate, 27(17), 6647-6659. doi:10.1175/JCLI-D-14-00138.1

Maussion, F., Scherer, D., Mölg, T., Collier, E., Curio, J. and Finkelnburg, R. (2014a): Precipitation seasonality and variability over the Tibetan Plateau as resolved by the High Asia Reanalysis. Journal of Climate, 27(5), 1910-1927. doi:10.1175/JCLI-D-13-00282.1

Maussion, F. (2014b): A new atmospheric dataset for High Asia - Development, validation and applications in climatology and in glaciology. Doctoral thesis, Technische Universität Berlin. doi:10.14279/depositonce-3979

McKenna, L.W. and Walker, J.D. (1990) Geochemistry of crustally derived leucocratic igneous rocks from the Ulugh Muztagh area, northern Tibet and their implications for the formation of the Tibetan Plateau. Journal of Geophysical Research: Solid Earth (1978–2012), 95(B13), 21483-21502.

Mernild, S., Pelto, M., Malmros, J.K., Yde, J.C., Knudsen, N.T. and Hanna, E. (2013) Identification of snow ablation rate, ELA, AAR and net mass balance using transient snowline variations on two Arctic glaciers. Journal of Glaciology, 59 (216): 649-659. doi:10.3189/2013JoG12J221

Metsämäki, S., Pulliainen, J., Salminen, M., Luojus, K., Wiesmann, A., Solberg, R., Böttcher, K., Hiltunen, M. and Ripper, E. (2015) Introduction to GlobSnow Snow Extent products with considerations for accuracy assessment. Remote Sensing of Environment, 156, 96-108. doi:10.1016/j.rse.2014.09.018

Meyerhoff, A. A., Kamen-Kaye, M., Chen, C. and Taner, I. (1991) Stratigraphy and Paleontology. In China—Stratigraphy, Paleogeography and Tectonics, pp. 7-113. Springer Netherlands.

Miehe, G., Miehe, S., Will, M., Opgenoorth, L., Duo, L., Dorgeh, T. and Liu, J. (2008) An inventory of forest relicts in the pastures of Southern Tibet (Xizang AR, China). Plant Ecology, 194(2), 157-177. doi:10.1007/s11258-007-9282-0

Miehe, G., Miehe, S., Kaiser, K., Reudenbach, C., Behrendes, L., Duo, L. and Schlütz, F. (2009) How old is pastoralism in Tibet? An ecological approach to the making of a Tibetan landscape. Palaeogeography, Palaeoclimatology, Palaeoecology, 276(1), 130-147. doi:10.1016/j.palaeo.2009.03.005

Mölg, T., Cullen, N.J., Hardy, D.R., Winkler, M. and Kaser, G. (2009) Quantifying Climate Change in the Tropical Midtroposphere over East Africa from Glacier Shrinkage on Kilimanjaro. Journal of Climate, 22(15).

Mölg, T., Maussion, F., Yang, W. and Scherer, D. (2012) The footprint of Asian monsoon dynamics in the mass and energy balance of a Tibetan glacier. The Cryosphere, *6*(6), 1445-1461. doi:10.5194/tcd-6-3243-2012

Mölg, T., Maussion, F.and Scherer, D. (2014) Mid-latitude westerlies as a driver of glacier variability in monsoonal High Asia. Nature Climate Change. doi:10.1038/ nclimate2055

Möller, M. and Schneider, C. (2010) Volume change at Gran Campo Nevado, Patagonia in 1984-2000 - a reassessment based on new findings. Journal of Glaciology, 56(196), 363-365. doi:10.3189/002214310791968458

Möller, M., Finkelnburg, R., Braun, M., Hock, R., Jonsell, U., Pohjola, V. A., Schneider, D. and Schneider, C. (2011) Climatic mass balance of the ice cap Vestfonna, Svalbard: A spatially distributed assessment using ERA-Interim and MODIS data. Journal of Geophysical Research: Earth Surface (2003–2012), 116(F3). doi:10.1029/2010JF001905

Molnar, P. (1987a) The Highest Peak on the Northern Tibetan Plateau. Alpine Journal, 104-116, 1987.

Molnar, P., Burchfiel, B.C., Zhao, Z., Lian, K.,Wang, S. and Huang, M. (1987b) Geologic evolution of northern Tibet: results of an expedition to Ulugh Muztagh. Science 23:299–305

Molnar, P., Boos, W.R. and Battisti, D.S. (2010) Orographic controls on climate and paleoclimate of Asia: thermal and mechanical roles for the Tibetan Plateau. Annual Reviews Earth and Planetary Sciences 38 (1), 77–102. doi:10.1146/annurev-earth-040809-152456

Mulch, A. and Chamberlain, C.P. (2006) Earth science: The rise and growth of Tibet. Nature, 439(7077), 670-671. doi:10.1038/439670a

Murphy, M.A., Yin, A., Harrison, T.M., Dürr, S.B., Chen, Z., Ryerson, F.J. and Zhou, X. (1997) Did the Indo-Asian collision alone create the Tibetan plateau? Geology, 25(8), 719-722.

Neckel, N., Braun, A., Kropáček, J. and Hochschild, V. (2013) Recent mass balance of the Purogangri Ice Cap, central 594 Tibetan Plateau, by means of differential X-band SAR interferometry. The Cryosphere, 7(5). doi:10.5194/tc-7-1623-2013

Neckel, N., Kropáček, J., Bolch, T. and Hochschild, V. (2014) Glacier mass changes on the Tibetan Plateau 2003–2009 derived from ICESat laser altimetry measurements. Environmental Research Letters, 9(1), 014009. doi:10.1088/1748-9326/9/1/014009

Neckel, N., Kropáček, J., Schröter, B. and Scherer, D. (2015) Effects of Cyclone Hudhud captured by a high altitude Automatic Weather Station in northwestern Nepal. Weather, 70(7), 208-210. doi:10.1002/wea.2494

Oerlemans, J. (2010) The microclimate of valley glaciers, Igitur, 138 pp.

Palazzi, E., von Hardenberg, J. and Provenzale, A. (2013) Precipitation in the Hindu-Kush Karakoram Himalaya: Observations and future scenarios, Journal of Geophysical Research: Atmospheres, 118, 85-100. doi:10.1029/2012JD018697

Park, H.S., Chiang, J.C.H., Lintner, B. and Zhang, G.J. (2010) The delayed effect of major El Niño events on Indian Monsoon Rainfall. Journal of Climate, 23, 932–946.

Paterson, W.S.B., and Cuffey, K.M. (1994) The physics of glaciers (Vol. 3). Oxford: Pergamon.

Paul, F., Kääb, A., Maisch, M., Kellenberger, T. and Haeberli, W. (2002) The new remote-sensing-derived Swiss glacier inventory: I. Methods. Annals of Glaciology, 34(1), 355-361.

Paul, F., Huggel, C. and Kääb, A. (2004) Combining satellite multispectral image data and a digital elevation model for mapping debris-covered glaciers. Remote Sensing of Environment, 89(4), 510-518. doi:10.1016/j.rse.2003.11.007

Paul, F., Barrand, N.E., Baumann, S., Berthier, E., Bolch, T., Casey, K., Frey, H., Josji, S.P., Konovalov, V., Le Bris, R., Mölg, M., Nosenko, G., Nuth, C., Pope, A., Racoviteanu, A., Rastner, P., Raup, B., Scharrer, K., Steffen, S. and Winsvold, S. (2013) On the accuracy of glacier outlines derived from remote-sensing data. Annals of Glaciology, 54(63), 171-182. doi:10.3189/2013AoG63A296

Pelto, M. (2011) Utility of late summer transient snowline migration rate on Taku Glacier, Alaska. The Cryosphere, 5, 1127–1133. doi:10.5194/tc-5-1127-2011

Pelto, M. and Brown, C. (2012) Mass balance loss of Mount Baker, Washington glaciers 1990–2010. Hydrological Processes, 26(17), 2601-2607. doi:10.1002/hyp.9453

Pepe, M., Brivio, P.A., Rampini, A., Nodari, F.R. and Boschetti, M. (2005) Snow cover monitoring in Alpine regions using ENVISAT optical data. International Journal of Remote Sensing, 26(21), 4661-4667. doi:10.1080/01431160500206635

Pfeffer, W.T., Arendt, A., Bliss, A., Bolch, T., Cogley, J.G., Gardner, A.S., Hagen, J., Hock, R., Kaser, G., Kienholz, C., Miles, E.S., Moholdt, G., Mölg, N., Paul, F., Radíc, V., Rastner, P., Raup, B.H., Rich, J., Sharp, M.J. and The Randolph Consortium (2014) The Randolph Glacier Inventory: a globally complete inventory of glaciers. Journal of Glaciology, 60(221), 537. doi:10.3189/2014JoG13J176

Pope, A., Rees, W.G., Fox, A.J. and Fleming, A. (2014) Open access data in polar and cryospheric remote sensing. Remote Sensing, 6(7), 6183-6220. doi:10.3390/rs6076183

Porter, S.C. (1975) Equilibrium-line altitudes of late Quaternary glaciers in the Southern Alps, New Zealand. Quaternary Research 5, 27–47. doi:10.1016/0033-5894(75)90047-2

Pritchard, H.D., Luthcke, S.B. and Fleming, A.H. (2010) Understanding ice-sheet mass balance: progress in satellite altimetry and gravimetry. Journal of Glaciology, 56(200), 1151-1161.

Qi, W., Xuejun, Q., Qigui, L., Freymueller, J., Shaomin, Y., Caijun, X. and Gang, C. (2011) Rupture of deep faults in the 2008 Wenchuan earthquake and uplift of the Longmen Shan. Nature Geoscience, 4(9), 634-640. doi:10.1038/ngeo1210

Qiu, J. (2008) China: the third pole. Nature News, 454(7203), 393-396.

Qu, B., Ming, J., Kang, S.C., Zhang, G.S., Li, Y. W., Li, C.D., Zhao, S.Y., Ji, Z.M. and Cao, J.J. (2014) The decreasing albedo of the Zhadang glacier on western Nyainqêntanglha and the role of light-absorbing impurities. Atmospheric Chemistry and Physics, 14(20), 11117-11128. doi:10.5194/acp-14-11117-2014

Rabatel, A., Bermejo, A., Loarte, E., Socuro, A., Gomez, J., Leonardini, G., Vincent, C., Sicart and J.E. (2012) Can the snowline be used as an indicator of the equilibrium line and mass balance for glaciers in the outer tropics? Journal of Glaciology, 58, 212, 1027- 1036. doi:10.3189/2012JoG12J027

Rasmussen, R., Dixon, M., Vasiloff, S., Hage, F., Knight, S., Vivekanandan, J. and Xu, M. (2003) Snow nowcasting using a real-time correlation of radar reflectivity with snow gauge accumulation. Journal of Applied Meteorology, 42(1), 20-36.

Ratschbacher, L., Krumrei, I., Blumenwitz, M., Staiger, M., Gloaguen, R., Miller, B.V. and Appel, E. (2011) Rifting and strike-slip shear in central Tibet and the geometry, age and kinematics of upper crustal extension in Tibet. Geological Society, London, Special Publications, 353(1), 127-163. doi:10.1144/SP353.8

Rees, W.G. (2005) Remote sensing of snow and ice. CRC Press.

Riggs, G. A. and Hall, D. K. (2002, June) Reduction of cloud obscuration in the MODIS snow data product. In 59th Eastern Snow Conference (Vol. 5, No. 7).

Royden, L.H., Burchfiel, B.C. and van der Hilst, R.D. (2008) The geological evolution of the Tibetan Plateau. Science, 321(5892), 1054-1058. doi:10.1126/science.1155371

Rupper, S. and Roe, G. (2008) Glacier changes and regional climate: a mass and Energy balance approach. Journal of Climate, 21(20), 5384-5401. doi:10.1175/2008JCLI2219.1

Ryavec, K. E. (2015) A Historical Atlas of Tibet. University of Chicago Press.

Sakai, A., Nuimura, T., Fujita, K., Takenaka, S., Nagai, H. and Lamsal, D. (2015) Climate regime of Asian glaciers revealed by GAMDAM glacier inventory. The Cryosphere, 9(3), 865-880. doi:10.5194/tc-9-865-2015

Sauter, T., Möller, M., Finkelnburg, R., Grabiec, M., Scherer, D. and Schneider, C. (2013) Snowdrift modelling for the Vestfonna ice cap, north-eastern Svalbard. The Cryosphere, 7(4). doi:10.5194/tc-7-1287-2013

Scherler, D., Bookhagen, B. and Strecker, M.R. (2011) Spatially variable response of Himalayan glaciers to climate change affected by debris cover. Nature Geoscience, 4(3), 156-159. doi:10.1038/ngeo1068

Schiemann, R., Lüthi, D. and Schär, C. (2009) Seasonality and interannual variability of the westerly jet in the Tibetan Plateau region. Journal of Climate, 22(11), 2940-2957. doi:10.1175/2008JCLI2625.1

Shaman, J. and Tziperman, E. (2005) The effect of ENSO on Tibetan Plateau snow depth: A stationary wave teleconnection mechanism and implications for the South Asian monsoons. Journal of Climate, 18(12), 2067-2079.

Shan, B., Xiong, X., Wang, R., Zheng, Y. and Yadav, R.B.S. (2015) Stress evolution and seismic hazard on the Maqin-Maqu segment of East Kunlun Fault zone from co-, post-and interseismic stress changes. Geophysical Journal International, 200(1), 244-253. doi:10.1093/gji/ggu395

Shangguan, D.H., Liu, S.Y., Ding, Y.J., Ding, L.F. and Li, G. (2004) Glacier changes at the head of Yurungkax River in the west Kunlun Mountains in the past 32 years. ACTA Geographica Sinica 59 (6), 855 – 862 (In Chinese).

Shangguan, D.H., Liu, S.Y., Ding, Y.J., Ding, L.F., Shen, Y.P., Zhang, S.Q., Lu, A.X., Li, G., Cai, D.H. and Zhang, Y. (2005) Monitoring glacier changes and inventory of glaciers in Muztag Ata-Kongur Tagh, East Pamir, China using ASTER data. Journal of Glaciology and Geocryology 27 (3), 344 – 351 (In Chinese).

Shangguan, D.H., Liu, S., Ding, Y., Ding, L., Xiong, L., Cai, D. and Zhang, Y. (2006) Monitoring the glacier changes in the Muztag Ata and Konggur mountains, east Pamirs, based on Chinese Glacier Inventory and recent satellite imagery. Annals of Glaciology, 43(1), 79-85. doi: 10.3189/172756406781812393

Shangguan, D., Liu, S., Ding, Y., Ding, L., Xu, J. and Jing, L. (2009) Glacier changes during the last forty years in the Tarim Interior River basin, northwest China. Progress in natural science, 19(6), 727-732. doi:10.1016/j.pnsc.2008.11.002

Shea, J.M., Menounos, B., Moore, R.D. and Tennant, C. (2013) An approach to derive regional snow lines and glacier mass change from MODIS imagery, western North America. The Cryosphere, 7(2). doi:10. 5194/tc-7-667-2013

Shi, Y. and Liu, S. (2000) Estimation on the response of glaciers in China to the global warming in the 21st century. Chinese Science Bulletin, 45(7), 668-672.

Shi, Y., Liu, C. and Kang, E. (2009) The glacier inventory of China. Annals of Glaciology, 50(53), 1-4. doi:10.3189/1727564107905 95831

Shrestha, A.B. and Aryal, R. (2011) Climate change in Nepal and its impact on Himalayan glaciers. Regional Environmental Change, 11(1), 65-77. doi:10.1007/s10113-010-0174-9

Spieß, M., Maussion, F., Möller, M., Scherer, D. and Schneider, C. (2015) MODIS derived equilibrium-line altitude estimates for Purogangri ice cap, Tibetan Plateau, and their relation to climatic predictors (2001–2012). Geografiska Annaler: Series A, Physical Geography, 20, 1–17. doi:10.1111/ geoa.12102

Spieß, M., Maussion, F. and Schneider, C. (2016a) MODIS-derived interannual variability of the equilibrium-line altitude across the Tibetan Plateau. Annals of Glaciology 57(71). doi:10.3189/2016AoG71A014

Spieß M., Huintjes, E. and Schneider, C. (2016b): Comparison of modelled- and remote sensing-derived snow line altitudes at Ulugh Muztagh, northern Tibetan Plateau. Journal of mountain science, 13(4), 593-613. doi:10.1007/s11629-015-3818-x

Stocker, T.F., Qin, D., Plattner, G.K., Tignor, M., Allen, S.K., Boschung, J. et al. (2013) IPCC, 2013: climate change 2013: the physical science basis. Contribution of working group I to the fifth assessment report of the intergovernmental panel on climate change.

Styron, R.H., Taylor, M.H., Sundell, K.E., Stockli, D.F., Oalmann, J.A., Möller, A. and Ding, L. (2013) Miocene initiation and acceleration of extension in the South Lunggar rift, western Tibet: Evolution of an active detachment system from structural mapping and (U-Th)/He thermochronology. Tectonics, 32(4), 880-907. doi:10.1002/tect.20053, 2013

Su, F., Zhang, L., Ou, T., Chen, D., Yao, T., Tong, K. and Qi, Y. (2016) Hydrological response to future climate changes for the major upstream river basins in the Tibetan Plateau. Global and Planetary Change, 136, 82-95. doi:10.1016/j.gloplacha.2015.10.012

Swenson, S. and Wahr, J. (2002) Methods for inferring regional surface-mass anomalies from Gravity Recovery and Climate Experiment (GRACE) measurements of time-variable gravity. Journal of Geophysical Research: Solid Earth (1978–2012), 107(B9), ETG-3. doi:10.1029/2001JB000576, 2002

Takaya, K. and Nakamura, H. (2013) Interannual variability of the East Asian winter monsoon and related modulations of the planetary waves. Journal of Climate, 26(23), 9445-9461. doi:10.1175/JCLI-D-12-00842.1

Tang, Z., Wang, J., Li, H., Yan, L. (2013) Spatiotemporal changes of snow cover over the Tibetan plateau based on cloud-removed moderate resolution imaging spectroradiometer fractional snow cover product from 2001 to 2011. Journal of Applied Remote Sensing, 7(1), 073582-073582. doi:10.1117/1.JRS.7.073582

Thompson, L.G., Yao, T., Davis, M.E., Mosley-Thompson, E., Mashiotta, T.A., Lin, P.N., Mikhalenko, V.N. and Zagorodnov, V.S. (2006) Holocene climate variability archived in the Puruogangri ice cap on the central Tibetan Plateau. Annals of Glaciology, 43(1), 61-69. doi:10.3189/ 172756406781812357

Tian, L., Zong, J., Yao, T., Ma, L., Pu, J. and Zhu, D. (2014) Direct measurement of glacier thinning on the southern Tibetan Plateau (Gurenhekou, Kangwure and Naimona'Nyi glaciers). Journal of Glaciology, 60(223), 879-888. doi:10.3189/2014JoG14J022

Town, J. (2008) The sliding snow of Tachab Kangri. The Alpine Journal 2008, 113(357), 84-92

Van der Woerd, J., Owen, L.A., Tapponnier, P., Xiwei, X., Kervyn, F., Finkel, R.C. and Barnard, P.L. (2004) Giant, ~M8 earthquake-triggered ice avalanches in the eastern Kunlun Shan, northern Tibet: Characteristics, nature and dynamics. Geological Society of America Bulletin, 116(3-4), 394-406. doi:10.1130/B25317.1

Wagnon, P., Vincent, C., Arnaud, Y., Berthier, E., Vuillermoz, E., Gruber, S. and Pokhrel, B.K. (2013) Seasonal and annual mass balances of Mera and Pokalde glaciers (Nepal Himalaya) since 2007. The Cryosphere, 7(6), 1769-1786. doi:10.5194/tc-7-1769-2013

Wang, A., Smith, J.A., Wang, G., Zhang, K., Xiang, S. and Liu, D. (2009) Late Quaternary river terrace sequences in the eastern Kunlun Range, northern Tibet: a combined record of climatic change and surface uplift. Journal of Asian Earth Sciences, 34(4), 532-543. doi:10.1016/j.jseaes.2008.09.003

Wang, B., Wu, R. and Lau, K.M. (2001) Interannual variability of the Asian summer monsoon: contrasts between the Indian and the Western North Pacific-East Asian Monsoons. Journal of Climate, 14(20), 4073-4090. doi:10.1175/1520-0442(2001)014<4073: IVOTAS> 2.0.CO;2

Wang, C., Dai, J., Zhao, X., Li, Y., Graham, S. A., He, D., Bo, R. and Meng, J. (2014) Outward-growth of the Tibetan Plateau during the Cenozoic: A review. Tectonophysics, 621, 1-43. doi:10.1016/j.tecto.2014.01.036

Wang, G., Li, Y., Wu, Q. and Wang, Y. (2006) Impacts of permafrost changes on alpine ecosystem in Qinghai-Tibet Plateau. Science in China Series D: Earth Sciences, 49(11), 1156-1169. doi:0.1007/s11430-006-1156-0

Wang, X., Yang, M., Liang, X., Pang, G., Wan, G., Chen, X. and Luo, X. (2014) The dramatic climate warming in the Qaidam Basin, northeastern Tibetan Plateau, during 1961–2010. International Journal of Climatology, 34(5), 1524-1537. doi:10.1002/joc.3781

Ward, M. (1989) The Kun Lun Shan: Desert Peaks of Central Asia. Alpine Journal

Wei, J., Liu, S., Guo, W., Yao, X., Xu, J., Bao, W. and Jiang, Z. (2014) Surface-area changes of glaciers in the Tibetan Plateau interior area since the 1970s using recent Landsat images and historical maps. Annals of Glaciology, 55, 66, 213-222. doi:10.3189/2014AoG66A038

Wei, Y. and Fang, Y. (2013) Spatio-temporal characteristics of global warming in the Tibetan Plateau during the last 50 years based on a generalised temperature zone – elevation model. PLOS ONE, 8, 4, e60044

Wu, B. (2005) Weakening of Indian summer monsoon in recent decades. Advances in Atmospheric Sciences, 22, 21-29.

Wu, G. and Zhang, Y. (1998) Tibetan Plateau forcing and the timing of the monsoon onset over South Asia and the South China Sea. Monthly Weather Review, 126, 913–927, doi:10.1175/1520-0493(1998)126<0913:TPFATT.2.0.CO;2

Wu, H.，He, J.， Guo，Z., Mao, R. and Wu, Y. (2013) The temporal and spatial changes of snow depth in Ulugh Muztagh area derived from HJ-1 satellite data. Geographical Research, 32.10(2013):1782-1791. doi:10.11821/dlyj201310002 (In Chinese with English abstract)

Wu, H., Wang, N., Jiang, X. and Guo, Z. (2014) Variations in water level and glacier mass balance in Nam Co lake, Nyainqêntanglha range, Tibetan Plateau, based on ICESat data for 2003-09. Annals of Glaciology, 55, 66, 239-247. doi:10.3189/2014AoG66A100

Wu, Z., Wang, B., Li, J. and Jin, F. (2009) An empirical seasonal prediction model of the east Asian summer monsoon using ENSO and NAO. Journal of Geophysical Reserach, 114, D18120. doi:10.1029/2009JD011733

Wu, Z., Li, J., Jiang, Z. and Ma, T. (2012) Modulation of the Tibetan Plateau snow cover on the ENSO teleconnections: From the East Asian summer monsoon perspective. Journal of Climate, 25(7), 2481-2489. doi:10.1175/JCLI-D-11-00135.1

Xu, W. and Liu, X. (2007) Response of vegetation in the Qinghai-Tibet Plateau to global warming. Chinese Geographical Science, 17(2), 151-159. doi:10.1007/s11769-007-0151-5

Xu, X. (2014) Interactive comment on “An important mechanism sustaining the atmospheric “water tower” over the Tibetan Plateau”. Atmospheric Chemistry and Physics, 14, 11287–11295. doi:10.5194/acp-14-11287-2014

Xue, X., Guo, J., Han, B., Sun, Q. and Liu, L. (2009) The effect of climate warming and permafrost thaw on de-sertification in the Qinghai-Tibetan Plateau. Geomorphology, 108, 182-190.

Yafeng, S., Desheng, M., Tandong, Y., Qunzhu, Z. and Chaohai, L. (2005) Glaciers of Asia – Glaciers of China. U.S. Geological Survey Professional Paper 1386 –F-2

Yan, S., Liu, G., Wang, Y., Perski, Z. and Ruan, Z. (2015) Glacier surface motion pattern in the Eastern part of West Kunlun Shan estimation using pixel-tracking with PALSAR imagery. Environmental Earth Sciences, 74(3), 1871-1881. doi:10.1007/s12665-015-4645-7

Yang, B., Bräuning, A., Liu, J., Davis, M. E. and Yajun, S. (2009) Temperature changes on the Tibetan Plateau during the past 600 years inferred from ice cores and tree rings. Global and Planetary Change, 69(1), 71-78. doi: 10.1016/j.gloplacha.2009.07.008

Yang, K., Wu, H., Qin, J., Lin, C., Tang, W. and Chen, Y. (2014) Recent climate changes over the Tibetan Plateau and their impacts on energy and water cycle: A review. Global Planetary Change, 112, 79-91. doi:10.1016/j.gloplacha.2013.12.001

Yang, M., Nelson, F.E., Shiklomanov, N.I., Guo, D. and Wan, G. (2010) Permafrost degradation and its environmental effects on the Tibetan Plateau: a review of recent research. Earth-Science Reviews, 103(1), 31-44. doi:10.1016/j.earscirev.2010.07.002

Yang, W., Guo, X., Yao, T., Zhu, M. and Wang, Y. (2015) Recent accelerating mass loss of southeast Tibetan glaciers and the relationship with changes in macroscale atmospheric circulations. Climate Dynamics, 1-11. doi:10.1007/s00382-015-2872-y

Yao, T., Li, Z., Thompson, L.G., Mosley-Thompson, E., Wang, Y., Tian, L., Wang, N. and Duan, K. (2006) 18O records from Tibetan ice cores reveal differences in climatic changes. Annals of Glaciology, 43(1), 1-7. doi:10.3189/1727564067818 12131

Yao, T., Pu, J., Lu, A., Wang, Y. and Yu, W. (2007) Recent glacial retreat and its impact on hydrological processes on the Tibetan Plateau, China, and surrounding regions. Arctic, Antarctic, and Alpine Research, 39(4), 642-650. doi:10.1657/1523-0430(07-510)[YAO]2.0.CO;2

Yao, T. (2010) Glacial fluctuations and its impacts on lakes in the southern Tibetan Plateau. Chinese Science Bulletin, 55(20), 2071-2071. doi: 10.1007/s11434-010-4327-5

Yao, T., Thompson, L., Yang, W., Yu, W., Gao, Y., Guo, X., Yang, X., Duan, K., Zhai, H., Xu, B., Pu, J., Lu, A., Xiang, Y., Kattel, D.B. and Joswiak, D. (2012) Different glacier status with atmospheric circulations in Tibetan Plateau and surroundings. Nature Climate Change, 2(9), 663-667. doi:10.1038/nclimate1580

Yasuda, T. and Furuya, M. (2012) Short-term glacier velocity changes at west kunlun shan, northwest tibet, detected by synthetic aperture radar data. Remote Sensing of Environment, 128, 87-106. doi:10.1016/j.rse.2012.09.021

Yatagai, A., Kamiguchi, K., Arakawa, O., Hamada, A., Yasutomi, N. and Kitoh, A. (2012) APHRODITE: Constructing a Long-term daily Gridded Precipitation Dataset for Asia based on a Dense Network of Rain Gauges. Bulletin of American Meteorological Society, 93, 1401–1415. doi:10.1175/BAMS-D-11-00122.1

Ye, Q., Kang, S., Chen, F. and Wang, J. (2006) Monitoring glacier variations on Geladandong mountain, central Tibetan Plateau, from 1969 to 2002 using remote-sensing and GIS technologies. Journal of Glaciology, 52(179), 537-545. doi:10.3189/ 172756506781828359

Yeh, T.C., Lo, S.W. and Chu, P.C. (1957) The wind structure and heat balance in the lower troposphere over Tibetan Plateau and its surrounding. Acta Meteorologica Sinica, 28(2), 108-121.

Yi, C., Li, X. and Qu, J. (2002) Quaternary glaciation of Puruogangri—the largest modern ice field in Tibet. Quaternary International, 97, 111-121. doi:10.1016/S1040-6182(02)00056-3

Yin, A. and Harrison, T.M. (2000) Geologic evolution of the Himalayan-Tibetan orogen. Annual Review of Earth and Planetary Sciences, 28(1), 211-280. doi:10.1146/annurev.earth.28.1.211

You, Q., Kang, S., Pepin, N., Flügel, W.A., Sanchez-Lorenzo, A., Yan, Y. and Zhang, Y. (2010) Climate warming and associated changes in atmospheric circulation in the eastern and central Tibetan Plateau from a homogenized dataset. Global and Planetary Change, 72(1), 11-24. doi:10.1016/j.gloplacha.2010.04.003

You, Q., Fraedrich, K., Ren, G., Ye, B., Meng, X. and Kang, S. (2012) Inconsistencies of precipitation in the eastern and central Tibetan Plateau between surface adjusted data and reanalysis. Theoretical and Applied Climatology, 109, 485–496, doi:10.1007/s00704-012-0594-1

You, Q., Fraedrich, K., Min, J., Kang, S., Zhu, X., Pepin, N. and Zhang, L. (2014) Observed surface wind speed in the Tibetan Plateau since 1980 and its physical causes. International Journal of Climatology, 34(6), 1873-1882. doi:10.1002/joc.3807

Yuan, C., Tozuka, T. and Yamagata, T. (2012) IOD influence on the early winter Tibetan Plateau snow cover: diagnostic analyses and an AGCM simulation. Climate dynamics, 39(7-8), 1643-1660.

Yuan, D.Y., Ge, W.P., Chen, Z.W., Li, C.Y., Wang, Z.C., Zhang, H.P. et al. (2013) The growth of northeastern Tibet and its relevance to large-scale continental geodynamics: A review of recent studies. Tectonics, 32(5), 1358-1370. doi:10.1002/tect.20081

Zhang, G., Xie, H., Kang, S., Yi, D. and Ackley, S.F. (2011) Monitoring lake level changes on the Tibetan Plateau using ICESat altimetry data (2003–2009). Remote Sensing of Environment, 115(7), 1733-1742. doi:10.1016/j.rse.2011.03.005

Zhang, G., Xie, H., Yao, T., Liang, T. and Kang, S. (2012) Snow cover dynamics of four lake basins over Tibetan Plateau using time series MODIS data (2001–2010). Water Resources Research, 48(10). doi:10.1029/2012WR011971. doi:0.1002/grl.50462

Zhang, G., Yao, T., Xie, H., Kang, S. and Lei, Y. (2013) Increased mass over the Tibetan Plateau: from lakes or glaciers? Geophysical Research Letters, 40(10), 2125-2130.

Zhang, Y., Fujita, K., Ageta, Y., Nakawo, M., Yao, T. and Pu, J. (1998) The response of glacier ELA to climate fluctuations on High-Asia. Bulletin of glacier Research, (16), 1-11.

Zhao, S. (1986) Physical Geography of China, Science Press, 209 pp.

Zhao, H., Xu, B., Yao, T., Wu, G., Lin, S., Gao, J. and Wang, M. (2012) Deuterium excess record in a southern Tibetan ice core and its potential climatic implications. Climate Dynamics, 38, 1791-1803.

Zhao, L., Ding, R. and Moore, J.C. (2014a) Glacier volume and area change by 2050 in high mountain Asia. Global and Planetary Change, 122, 197-207. doi:10.1016/j.gloplacha.2014.08.006

Zhao, L., Tian, L., Zwinger, T., Ding, R., Zong, J., Ye, Q. and Moore, J.C. (2014b) Numerical simulations of Gurenhekou glacier on the Tibetan Plateau. Journal of Glaciology, 60(219), 71-82. doi:10.3189/2014JoG13J126

Zhu, L., Xie, M. and Wu, Y. (2010) Quantitative analysis of lake area variations and the influence factors from 1971 to 2004 in the Nam Co basin of the Tibetan Plateau. Chinese Science Bulletin, 55(13), 1294-1303. doi:10.1007/s11434-010-0015-8

Acknowledgements of publications

Acknowledgements for "MODIS derived equilibrium-line altitude estimates fpr Purogangri Ice Cap, Tibetan Plateau, and their relation to climatic predictors (2001-2012)" (Chapter 4)

This work is supported by the German Research Foundation (DFG) Priority Programme 1372, "Tibetan Plateau: FormationClimateEcosystems" through the DynRG-TiP ("Dynamic Response of Glaciers on the Tibetan Plateau to Climate Change") project under the codes SCHN 680/3-3 and SCHE 750/4-3 and by the German Federal Ministry of Education and Research (BMBF) Central Asia-Monsoon Dynamics and Geo-Ecosystems (CAME) program, through the WET project ("Variability and Trends in Water Balance Components of Benchmark Drainage Basins on the Tibetan Plateau") under the code 03G0804A. FM acknowledges support by the Austrian Science Fund (FWF project P22443-N21). The MOD10A1 and MYD10A1 data product was obtained through the online Data Pool at the NASA Distributed Active Archive Center (DAAC) at National snow and ice data center (NSIDC) (http://nsidc.org/data/data_ pool/) The ASTER data product was obtained through the online Data Pool at the NASA Land Processes Distributed Active Archive Center (LP DAAC), USGS/Earth Resources Observation and Science (EROS) Center, Sioux Falls, South Dakota (https://lpdaac. usgs.gov/data_access). The glacier mask of Purogangri ice cap was provided by Niklas Neckel, University of Tübingen. All data analysis and graphics were realized and programmed in the IDL language, with the help of the WAVE and the Coyote IDL libraries. We thank one anonymous reviewer and Dr. Joseph Shea for valuable suggestions that improved the manuscript.

Acknowledgements for "MODIS derived inter-annual variability of the equilibrium-line altitude across the Tibetan Plateau" (Chapter 5)

This work is supported by the German Research Foundation (DFG) Priority Programme 1372, "Tibetan Plateau: FormationClimateEcosystems" through the DynRG-TiP ("Dynamic Response of Glaciers on the Tibetan Plateau to Climate Change") project under the codes SCHN 680/3-3 and SCHE 750/4-3 and by the German Federal Ministry of Education and Research (BMBF) Central Asia Monsoon Dynamics and Geo-Ecosystems (CAME) program, through the WET project ("Variability and Trends in Water Balance Components of Benchmark Drainage Basins on the Tibetan Plateau") under the code 03G0804A. Fabien Maussion acknowledges support by the Austrian Science Fund (FWF project P22443-N21). The MOD10A1 and MYD10A1 data product was obtained through the online Data Pool at the NASA Distributed Active Archive Center (DAAC) at National snow and ice data center (NSIDC) (http://nsidc.org/data/data_ pool/). The MOD02QKM and MYD02QKM data used in this study were acquired through the Atmosphere Archive and Distribution System (LAADS) at http://ladsweb.nascom.nasa.gov/ in Hierarchical Data Format (HDF). The acquisition of the MODIS data was supported by Frank Rüthrich, Philipps University of Marburg. The ASTER data product was obtained through the online Data Pool at the NASA Land Processes Distributed Active Archive Center (LP DAAC), USGS/Earth Resources Observation and Science (EROS) Center, Sioux Falls, South Dakota (https://lpdaac. usgs.gov/data_access). We thank Niklas Neckel, University of Tübingen, Nicolai Holzer, TU Dresden, Tobias Bolch, University of Zurich and Ulrike Schinke, TU Dresden for the acquisition of the glacier masks. All data analysis and graphics were realized and programmed in the IDL language, with the help of the WAVE and the Coyote IDL libraries. Sincere thanks are due to

Mauri Pelto, two anonymous reviewer, the scientific editor Joseph Shea and the chief editor of AoG Graham Cogley for their valuable comments which greatly improved an earlier version of this work.

Acknowledgements for „Comparison of modelled- and remote sensing- derived snow line altitudes at Ulugh Muztagh, northern Tibetan Plateau" (Chapter 6)

This work was supported by the German Research Foundation (DFG) Priority Programme 1372, 'Tibetan Plateau: Formation Climate Ecosystems' through the DynRG-TiP ('Dynamic Response of Glaciers on the Tibetan Plateau to Climate Change') project under codes SCHN 680/3-3 and SCHE 750/4-3 and by the German Federal Ministry of Education and Research (BMBF) Central Asia Monsoon Dynamics and Geo-Ecosystems (CAME) program, through the WET project ('Variability and Trends in Water Balance Components of Benchmark Drainage Basins on the Tibetan Plateau') under code 03G0804A. The MOD02QKM and MYD02QKM data used in this study were acquired through the Level 1 and Atmosphere Archive and Distribution System (LAADS) at http://ladsweb.nascom.nasa.gov/ in Hierarchical Data Format (HDF). The acquisition of the MODIS data was supported by Frank Rüthrich, Philipps University of Marburg. The ASTER data product was obtained through the online Data Pool at the NASA Land Processes Distributed Active Archive Center (LP DAAC), US Geological Survey (USGS)/Earth Resources Observation and Science (EROS) Center, Sioux Falls, SD (https://lpdaac.usgs.gov/data_access). We thank Lena Funken for the preparation of the glacier mask. COSIMA is run in MATLAB. Data analysis and graphics were realized and programmed either in the Interactive Data Language (IDL), with the help of the WAVE and the Coyote IDL libraries or in R - free software environment for statistical computing and graphics. We thank two reviewers and the scientific editor for their thoughtful comments on an earlier version of this manuscript which helped to improve the publication.